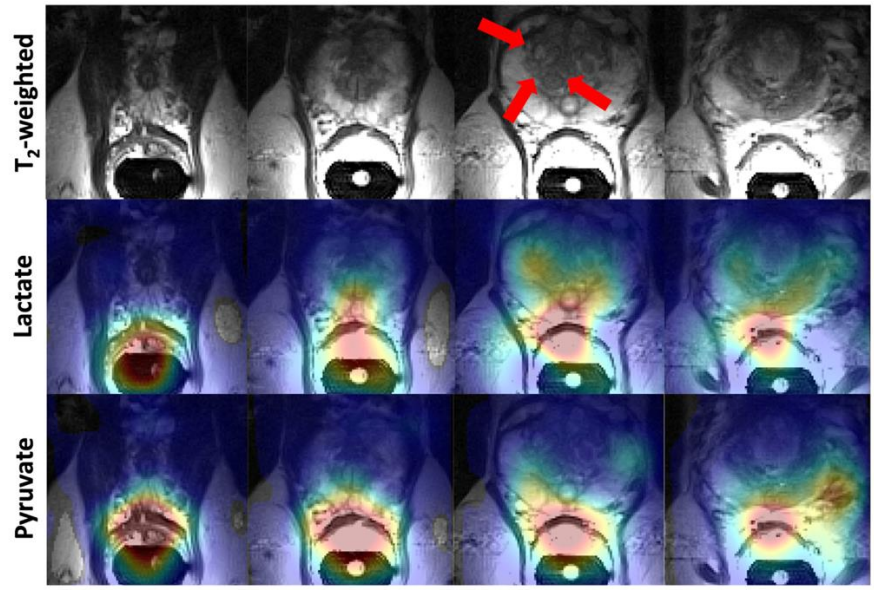

Enabling clinical Hyperpolarised ^{13}C-MR cancer imaging through phantom development, pulse sequence optimisation and quantitative image processing

Rafat Chowdhury

Centre for Medical Imaging

University College London (UCL)

A thesis submitted to University College London for the degree of Doctor of Philosophy

2023

I, Rafat Chowdhury, confirm that the work presented in this thesis is my own. Where information has been derived from other sources, I confirm, has been indicated in the thesis.

Abstract

Hyperpolarised ^{13}C-Magnetic Resonance Imaging (^{13}C-MR), via dissolution Dynamic Nuclear Polarisation (d-DNP), is an emerging technique which uses a non-ionising contrast agent to quantify metabolic processes *in vivo*. Reactions such as the conversion of carbon-13 labelled pyruvate into lactate, in a process analogous to the Warburg effect, can now be observed in real time.

Hyperpolarised ^{13}C-MR has previously been used to demonstrate significant differences in metabolism between healthy tissue and prostate cancer. Clinical hyperpolarised ^{13}C-MR studies are on-going with several imaging techniques presented in recent years.

This thesis aims to develop physical and *in silico* platforms on which to optimise and test pulse sequences, whilst also optimising an existing pulse sequence and applying this in clinical hyperpolarised ^{13}C-MR studies.

Firstly, a test object was developed which successfully reduced the variance of analysis outcomes in hyperpolarised ^{13}C-MR studies by incorporating an automated injection system for the hyperpolarised agent (coefficient of variation: 11-23% (n = 8)). Secondly, an existing numerical simulator was empirically validated (r: >0.95) and then used to identify the optimal spectral parameters for an ME-bSSFP sequence, for use in prostate cancer imaging during hyperpolarised ^{13}C-MR studies.

Building on this work the optimised ME-bSSFP sequence was used to image a small cohort (n = 5) of subjects with biopsy confirmed prostate cancer tumours in a hyperpolarised ^{13}C-MR study. Significant differences between tumourous and healthy tissues were found ($p < 0.01$).

Finally, a single case of pheochromocytoma is presented, where the subject underwent a hyperpolarised ^{13}C-MR study, with differences in metabolism presented in cystic, solid and necrotic parts of the tumours.

Impact Statement

Prostate cancer (PCa) incidence is on the rise in the UK, with a particular clinical challenge in identifying those with histologically proven PCa, whose cancer would likely result in death if left untreated. Gleason grade assessment has traditionally been the method to discriminate the aggressiveness of disease. However, a large majority of patients are diagnosed with the same Gleason grade of 3+4; a heterogeneous group in which some progress, whilst others could safely avoid radical treatments and their significant side effects. An aggressive cancer is suggested to be more metabolically active than indolent forms, so metabolic imaging offers a potential approach to assessing disease aggressiveness. The assessment of PCa metabolism could avoid the unnecessary treatment of patients with non-lethal disease.

Hyperpolarised ^{13}C-Magnetic Resonance (MR) Imaging provides *in vivo* measurement of the conversion of organic molecules such as [1-^{13}C] pyruvate into their downstream metabolic products. This thesis has resulted in the publication of a number of papers from looking to develop platforms for reproducible hyperpolarised ^{13}C-MR experiments to optimising and testing a pulse sequence in a clinical environment. The sequence optimised in this thesis is now being used as part of one of the largest hyperpolarised ^{13}C-MR clinical studies in the world, looking to assess tumour metabolism as a means of staging cancer in a range of subjects with suspected PCa.

The phantom developed in this thesis is now being redesigned in collaboration with a commercial partner, Gold Standard Phantoms, with the core concept of automated, remote injection retained, for eventual use in a multisite study which aims to determine whether data obtained in hyperpolarised ^{13}C-MR studies between different scanners is comparable between sites. This study will be integral to

understanding the feasibility of clinically translating hyperpolarised ^{13}C-MR.

Acknowledgements

Firstly, I'd like to thank Professor Shonit Punwani for all of his support and encouragement throughout this entire project. He has consistently guided me to produce work that I can be proud of, and his advice has been invaluable in my development as a researcher. I would also like to thank Professor Peter Rich for his help throughout the course of my PhD, which reiterated to me the importance of having different perspectives to approaching multidisciplinary problems. Additionally, I would like to thank David Gadian, David Atkinson and Alan Bainbridge for their guidance and support through the reviewing of data, feedback on analysis and editing of papers.

I would also like to thank Xavier Golay and the group at Gold Standard Phantoms, their input and guidance was invaluable for someone with no experience in machining and product design. My time at Gold Standard Phantoms was truly enjoyable, being able to prototype phantoms. Gaining exposure to manufacturing techniques is something I'd never imagined having the opportunity to do, not least in such a hands-on manner.

I would additionally like to give a special mention to my colleagues, Lorna Smith, Fiona Gong, Vasia Papoutsaki, Max Bullock and Tom Syer for their patience, advice, and perseverance during our clinical studies, as well as their feedback on all of the publications related to this work. It took a lot out of all of us, but I couldn't have asked for a better group of colleagues to have gone on this journey with.

I'd also like to extend my thanks to the Biotechnology and Biological Sciences Research Council (BBSRC) for funding the LIDo PhD programme whom, funded this project (Ref: BB/R505973/1) as well as CRUK for funding the clinical studies outlined in this thesis.

Finally, I’d like to thank my wonderful family, my dad, Iqbal, my mum, Rahima, my brother Shafayat and my sister Fathima. They were there with me every step of the way and without them this work would not have been possible. In particular, I’d like to dedicate this to my dad, for inspiring me to do what I love, this one’s for you.

Table of Contents

List of figures

List of tables

Thesis Overview

Section A comprises of three chapters of literature reviews of: hyperpolarised ^{13}C-MR, pulse sequences and quantification methods currently used in clinical hyperpolarised ^{13}C-MR as well as the types of test objects (phantoms) currently used for both quality assurance purposes and pulse sequence testing in the hyperpolarised ^{13}C-MR field. There is also an additional chapter in this section outlining the principle aims of this body of work. **Chapter 1** gives some background on the general principles of hyperpolarisation, with a focus on hyperpolarised ^{13}C-MR, particularly, dissolution Dynamic Nuclear Polarisation (d-DNP) and its scientific underpinning. **Chapter 2** outlines the pulse sequences currently used in clinical hyperpolarised ^{13}C-MR studies, as well as their optimisation, with a specific focus on those used for prostate studies. This chapter also lists the different quantification methods used in hyperpolarised ^{13}C-MR studies, their advantages, as well as their limitations and major challenges currently facing the field. **Chapter 3** describes the development and use of a number of previously demonstrated 'dynamic phantoms', concentrating on features which contribute towards experimental reproducibility. **Chapter 4** describes the aims of the original research projects discussed in later sections.

Section B focuses on the development of tools to test pulse sequences, whilst also describing the optimisation of an existing Multi-echo balanced Steady-State Free Precession (ME-bSSFP) sequence. **Chapter 5** describes the design, construction, and testing of a metabolic phantom. The phantom was developed with the aim of delivering a highly reproducible platform on which to perform hyperpolarised ^{13}C-MR studies by eliminating factors such as manual contrast injection and mixing. The reproducibility of the phantom during hyperpolarised ^{13}C-MR studies was assessed. **Chapter 6** discusses the process by which an ME-bSSFP sequence, which had been previously demonstrated preclinically, was optimised for use in

clinical studies. Factors such as spatial, spectral and temporal resolution were considered with numerical simulators and empirical validation also described within this chapter. The optimal parameters were chosen by considering those most suitable for prostate cancer imaging in hyperpolarised ^{13}C-MR studies.

Section C builds on the work described in Chapter 6 by demonstrating the application of ME-bSSFP in clinical cases. **Chapter 7** presents a study wherein the optimised parameters identified in Chapter 6 were applied to a small cohort of individuals with biopsy-confirmed prostate cancer. Comparisons of hyperpolarised ^{13}C-MR metrics were made between histologically confirmed tumour and healthy regions. **Chapter 8** describes a case report where a subject with a large pheochromocytoma underwent a hyperpolarised ^{13}C-MR scan with imaging performed using ME-bSSFP. Differences between the cystic, solid and necrotic portions of the tumour were assessed.

Section D concludes this thesis with **Chapter 9** suggesting areas of potential further study related to the work outlined in the original research chapters.

Section E contains a series of appendices relevant to the work presented in **Chapters 5-8**, as well as a list of the references referred to throughout this entire body of work.

Peer Reviewed Journal Articles

Abeyakoon, O., Latifoltojar, A., Gong, F., Papoutsaki, M. V., Chowdhury, R., Glaser, M., ... & Punwani, S. (2019). Hyperpolarised 13 C MRI: a new horizon for non-invasive diagnosis of aggressive breast cancer. *BJR| case reports*, *5*(3), 20190026.

Chowdhury, R., Papoutsaki, M. V., Müller, C. A., Smith, L., Gong, F., Bullock, M., ... & Punwani, S. (2022). A reproducible dynamic phantom for sequence testing in hyperpolarised 13C-magnetic resonance. *The British Journal of Radiology*, *95*(1134), 20210770.

Chowdhury, R., Mueller, C. A., Smith, L., Gong, F., Papoutsaki, M.V., … & Punwani, S. (2022). Quantification of Prostate Cancer Metabolism Using 3D Multiecho bSSFP and Hyperpolarised [1-13C] Pyruvate: Metabolism Differs Between Tumors of the Same Gleason Grade. *Journal of Magnetic Resonance Imaging*

Chowdhury, R., Moorthy, M., Smith, L., Mueller, C. A., Gong, F., Rogers, H. J., ... & Punwani, S. (2023). First-in-human in-vivo depiction of paraganglioma metabolism by hyperpolarised 13C-magnetic resonance. *BJR| Case Reports*, *9*(6).

Section A

The following chapters provide a theoretical background on some basic magnetic resonance (MR) principles and then proceed to discuss the concept of hyperpolarisation, current challenges facing the field of hyperpolarised ^{13}C-MR, as well as the use of test objects in such studies. The final chapter in this section outlines the aims of each of the novel research chapters discussed in sections B and C.

Chapter 1: MR Theory and Hyperpolarised ^{13}C-MR

MR Background

Nuclei possess a quantum mechanical property known as spin, a non-zero value of which gives rise to a magnetic moment (Figure 1), with such nuclei including ^{1}H, ^{13}C, ^{23}Na and ^{31}P:

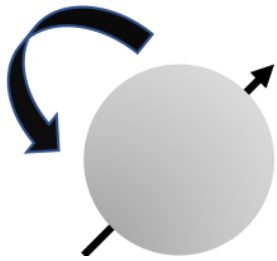

Figure 1 - Here a nucleus is shown with the property of spin illustrated by the curved black arrow

For the following explanations, we will consider a proton-based spin system. Upon being placed within an external magnetic field (B_0) these nuclei precess around the magnetic field and depending on the type of the nuclei (γ) and strength of the magnetic field a specific rate of precession can be observed, also referred to as the Larmor frequency (ω_0).

$$\omega_0 = -\gamma B_0 \qquad \text{Eq. 1}$$

Upon being placed in B_0 a group of nuclei with non-zero spin can orientate either with or against the field (Figure 2), with the nuclei readily able to transition between these two states upon excitation by an oscillating magnetic field (B_1).

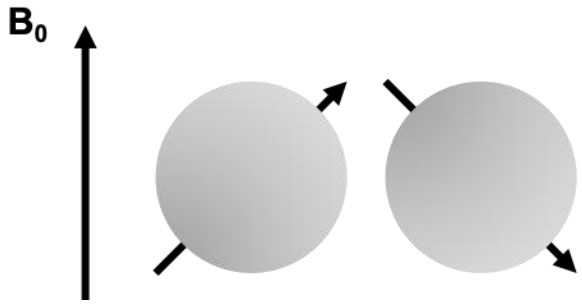

Figure 2 - In a magnetic field with direction B_0 nuclei will align either with (nuclei on the left) or against (nuclei on the right) the field

The lower energy state is, however, preferred, with the angular momenta (μ) of each state defined as:

$$\mu = \gamma \hbar I \qquad \text{Eq. 2}$$

Wherein represents γ is the nuclei's gyromagnetic ratio, $\hbar$ is the reduced Plank's constant (h/2π) and I is the combined spin quantum number of all elementary particles of a nuclei, these can be zero, integer, or half-integer values: -3/2,-1,-1/2,0,1/2,1,3/2… . From this we can derive the energy of each state ($\in$):

$$\in = -\mu B = -\gamma \hbar I B \qquad \text{Eq. 3}$$

Considering the spin angular quantum numbers of both spin states it is possible to derive their energy difference:

$$\Delta \in = -\left(\frac{1}{2} - -\frac{1}{2}\right)\gamma \hbar B = -\gamma \hbar B \qquad \text{Eq. 4}$$

By applying the De Broglie equation, allowing us to relate energy to frequency ($\Delta \in = \hbar\omega$) we find:

$$\hbar\omega_0 = -\gamma \hbar B_0 \qquad \text{Eq. 5}$$

$$\omega_0 = -\gamma B_0 \qquad \text{Eq. 1}$$

Equations 2 to 5 demonstrate how the frequency of energy required to transition between the two spin states is equal to the earlier identified Larmor frequency (Equation 1), at which the spins precess.

Due to the large number of nuclei *in vivo*, looking at individual spins becomes incredibly difficult to visualise, as such we consider the vector sum of our nuclei (Figure 3).

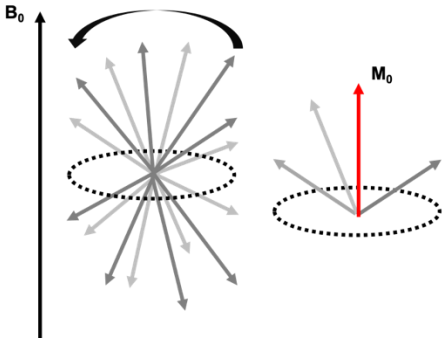

Figure 3 - Nuclei with non-zero spin, when placed in a magnetic field (B_0), align either with or against the direction of B_0 (left). There are however more nuclei in the lower energy state, giving rise to a net magnetisation vector (M_0), shown in red, aligned with B_0.

The greater number of nuclei being aligned with B_0 can be explained by quantifying the population distribution of the nuclei across the two spin states ($N_\uparrow$ and $N_\downarrow$). This can be described by the Boltzmann distribution, influenced by both $\Delta\epsilon$ and the temperature of the overall spin system (T_s).

$$\frac{N_\uparrow}{N_\downarrow} = \exp\left(\frac{\Delta\epsilon}{K_B T_s}\right) \qquad \text{Eq. 6}$$

Where K_B is the Boltzmann constant. In real terms we often observe $\Delta\epsilon$ to be considerably smaller than $K_B T_s$ and as such we can simplify equation 6 to the following:

$$\frac{N_\uparrow}{N_\downarrow} \approx 1 + \frac{\gamma\hbar B_0}{K_B T_s} \qquad \text{Eq. 7}$$

Where $N_\uparrow$ and $N_\downarrow$refers to the number of upward and downward facing spins respectively. Which when considering equation 4, in turn, affords:

Eq. 8

$$N_{\uparrow} - N_{\downarrow} \approx N_s \frac{\gamma \hbar B_0}{2K_B T_s}$$

Where N_s refers to the total number of nuclei in the system. Whilst this non-zero spin distribution is small, it does produce the quantifiable macroscopic magnetisation that is M_0, otherwise referred to as the observable NMR signal. This is also why M_0 is always aligned with B_0. M_0, however, is often found to be very small in comparison to B_0, to such an extent that it cannot be measured (Figure 4).

In MR imaging and spectroscopy radiofrequency (RF) pulses are used to generate oscillating magnetic fields (B_1) creating a measurable magnetic moment perpendicular (in the transverse plane) to M_0.

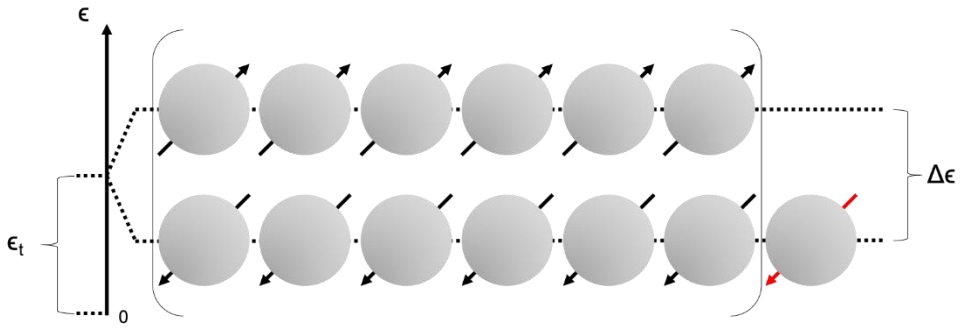

Figure 4 - Arrangement and distribution of nuclei in a magnetic field. Fractionally, more nuclei occupy the lower energy state (nuclei with red arrow), with the difference in energy between the two states (Δϵ) also shown. This distribution can be described as an example of thermal polarisation.

Before continuing, by convention, we will use a cartesian coordinate system, with M_0 considered to be aligned with the z-axis (Figure 5). As defined in Equation 1 the frequency of the RF pulse must equal f_0 and in doing so allows us to generate a measurable transverse magnetisation vector for our spin system (M_T).

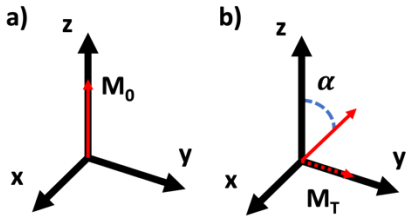

Figure 5 - An example of how an RF pulse allows for the tipping of the net magnetisation vector (M_0 - shown in red), by a predetermined angle (α) into the 'x' and 'y' axis relative to the 'z' (direction of the magnetic field), allowing for a now measurable vector (M_T).

The angle (α) by which M_0 is tipped is application dependent; in conventional MR imaging 90° pulses are not uncommon. The RF pulse is used to generate a magnetic field (B_1), along the transverse plane, its duration (t_P) and the gyromagnetic ratio (γ) of the nuclei being imaged all contribute to the size of α:

$$\alpha = \gamma B_1 t_P \qquad \text{Eq. 9}$$

The nuclei, now precessing in the transverse plane, induces voltage in receiver coils, this system then dephases over time through a number of relaxation methods, this generates a signal referred to as a free induction decay (FID).

The longitudinal relaxation (along the z-axis) of M_0 involves the recovery and realignment of the net magnetisation vector (M_0) with B_0 this is also referred to as T_1 or spin-lattice relaxation. The interaction of nuclei (spins) with the 'lattice', otherwise defined as the surrounding tissue, *in vivo*, affording a loss in energy, also known as T_1 relaxation. This process can be quantified by the time constant T_1 which is the time taken for 63% of M_0 to recover (Figure 6).

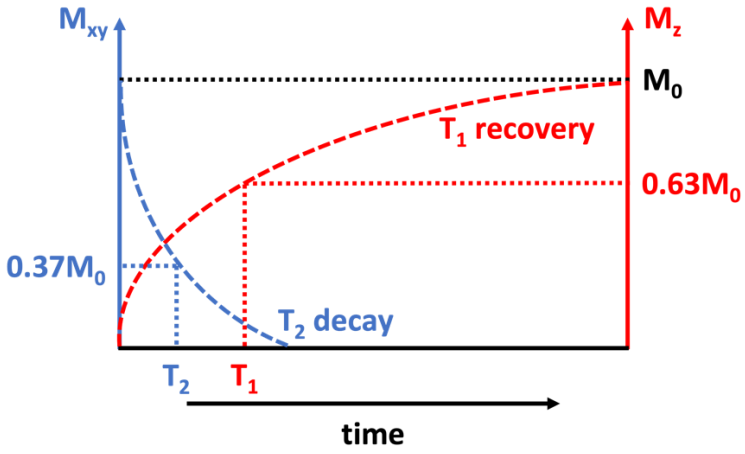

Figure 6 - The decay in the M_{xy} vector (blue) and recovery of M_0 along the M_z vector (red) allow are representative of T_2 decay and T_1 recovery respectively. Measuring these processes and identifying specific thresholds allow for the derivation of the constants T_2 ($0.37M_0$) and T_1 ($0.63M_0$).

Transverse relaxation (along the xy-axis), or the decay of the M_{xy}/M_T vector, due to the interactions between neighbouring spins, known as spin-spin relaxation, is quantifiable through the time constant T_2 which is the time taken for Mxy to decay to 37% of M_0.

T_2 and T_1 relaxation are independent processes with their time constants contributing to mono exponential decay functions (Equations 10 and 11).

$$\frac{dM_{xy}}{dt} = -\frac{M_{xy}}{T_2} \qquad \text{Eq. 10}$$

$$\frac{dM'_z}{dt} = -\frac{M'_z - M_z^{eq}}{T_1} \qquad \text{Eq. 11}$$

In addition to the above effects, field inhomogeneities in B_0 also contribute to a loss of phase coherence in M_T with the decay constant for this effect referred to as T_2*.

In nuclear magnetic resonance (NMR) spectroscopy experiments, the signal induced in the receiver coil can be converted, by an inverse Fourier transformation into a frequency spectrum.

When imaging a subject the nuclei in their body are subjected to an approximately homogeneous magnetic field (B_0). By employing linear spatial magnetic gradient fields in the orthogonal directions (such as those illustrated in Figure 5), as well as the simultaneous application of an RF-pulse, spatial localisation of the MR signal can be achieved.

The aforementioned spatial gradients introduce magnetic fields with known linear changes that modify the intensity of B_0; when applied, nuclei experience varying magnetic field strengths, resulting in different precessional frequencies as per equation 1. The slice-selecting gradient (G_{SS}), applied in the z-direction, is combined with an RF pulse. The simultaneous application of the slice-select gradient ensures that only spins within a specified region precess at frequencies resonant with the applied RF pulse. The slice thickness is determined by the RF pulse bandwidth and gradient strength.

Now that the slice position has been determined, to localise the signal in-plane a further two additional gradients are required. These are applied in the remaining two perpendicular directions: the frequency encoding gradient (G_{FE}) and the phase encoding gradient (G_{PE}).

G_{FE} follows the G_{SS} in another orthogonal direction, for example, the y-axis (with reference to Figure 5). This induces a spatially-dependent variation in precessional frequencies along this axis, encoding the location along this axis through frequency.

On the other hand, the G_{PE} is applied along the remaining orthogonal direction, i.e. the x-axis. G_{PE} is activated only briefly after the RF pulse, causing protons to precess with different frequencies along the x-axis during this period. Once this gradient is turned off, all protons return to their original precessional frequency. However, due to the phase shift introduced, protons are now out of sync with each other, and this phase change can be detected and encoded along this axis.

By combining the three aforementioned gradients the spatial localisation of MR signals can be achieved and the formation of images is facilitated.

Hyperpolarisation

Polarisation is the measure of nuclei which exist in a lower energy state when a sample containing nuclei with a non-zero spin (^{13}C ^{15}N) is placed in a magnetic field. For ^{13}C species at thermal equilibrium the polarisation (at 3T) is 2.5 nuclei per million (Figure 4). Hyperpolarisation is the process by which the nuclear spin polarisation of a species is amplified to levels far greater than its thermal equilibrium, by a factor of 10^4-10^5 (Figure 7). In recent times hyperpolarised tracers have been used for contrast-based imaging, however, due to the non-equilibrium nature of the hyperpolarised state the polarisation is subject to decay. Despite this, should the relaxation constants (T_1 and T_2) prove to be long enough, upon injection of the contrast into a phantom or human subject, data acquisition via MR spectroscopy/imaging is possible.

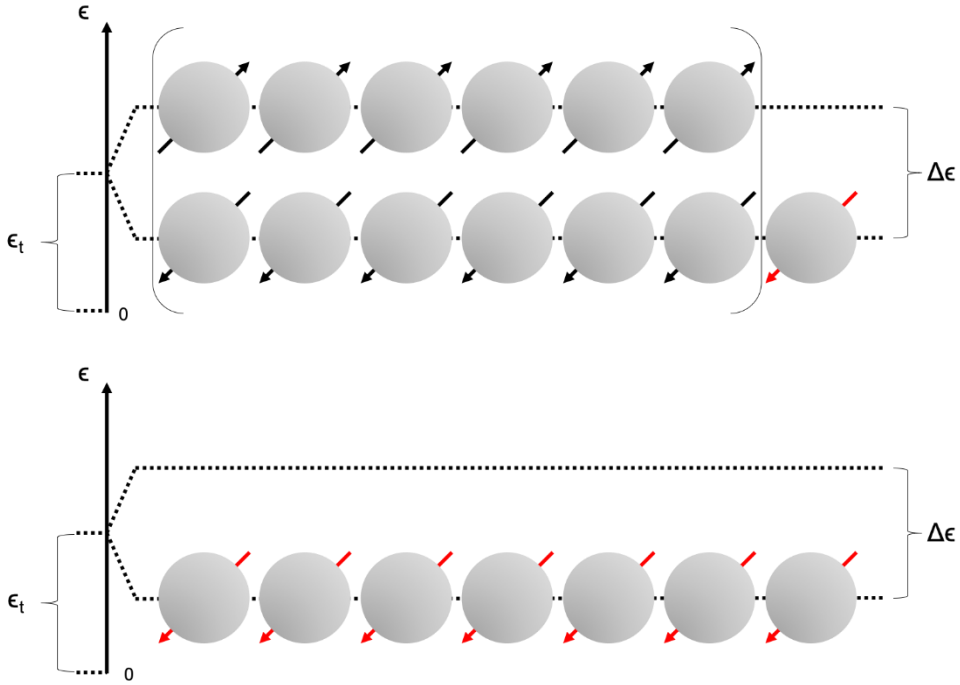

Figure 7 – Demonstrates thermal polarisation (top image), representative of a natural Boltzmann distribution, whilst the hyperpolarised state, arising by forcing nuclei into the lower energy state, is also shown (bottom image).

Hyperpolarised ^{13}C-MR studies are currently of great interest with a number of trials having already been conducted [1], [2]. The hyperpolarised state can be achieved through several methods, including dissolution-Dynamic Nuclear Polarisation (d-DNP), Parahydrogen Induced Polarisation (PHIP), Signal Amplification by Reversible Exchange (SABRE) and Spin exchange Optical Pumping (SEOP).

Dissolution - Dynamic Nuclear Polarisation

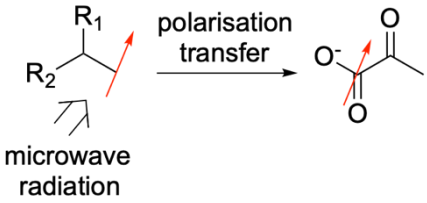

Figure 8 - An electroparamagnetic agent (left) is placed in a high magnetic field at a low temperature (<1K) which tips the Boltzmann distribution, encouraging high electron polarisation (red arrow on left side) of an electroparamagnetic agent (structure on the left side). Polarisation transfer to a carbon-13 labelled molecule (structure with red arrow on the right side) is induced by microwave irradiation.

d-DNP (Figure 8) involves a ^{13}C-labelled material, i.e. pyruvate being doped with an electroparamagnetic agent (EPA), with the sample cooled to <1K and placed in a strong magnetic field (approx. 3T)[1], [2]. The EPA is typically a free radical molecule. The cooling of the sample forces polarisation of the free electrons within the EPA (Equation 6), which, once a sufficient level of polarisation is reached, is irradiated with monochromatic microwave radiation, inducing the transfer of spin polarisation from the electrons within the EPA to the nuclei of ^{13}C-labelled material, via the Nuclear Overhauser Effect (NOE) [3]–[5]. The sample is dissolved by a solution (dissolution media - DM) heated to 130°C and then mixed with another to adapt the pH to physiologically acceptable levels (neutralisation media – NM) [3], [6]. The spin polarisation is short-lived; therefore, the sample is transferred from the hyperpolariser to the MR scanner as quickly as possible and injected into the test subject.

The process has been adapted for clinical use with a variety of filters used to remove EPA and any potential solid particulates after dissolution. Hyperpolariser systems such as the GE SPINLab are fully automated and also have quality control (QC) modules which analyse the polarised solutions upon dissolution to assess if they are safe to inject in patients [3], [6]. Presently, these factors make the methodology more clinically relevant and subsequently more applicable than both PHIP and SABRE.

Despite this, the technique does have some limitations, the first being the initial cost of the system, in the order of several million pounds; meaning that widespread use of the modality is limited by a significant financial barrier [7].

The ^{13}C-labelled material and EPA are placed within an apparatus called a fluid path (FP). This requires meticulous inspection prior to placing within the hyperpolariser as a number of faults, such as the FP exploding, could occur if factors such as moisture are not accounted for [8]. The FP also requires delicate handling and re-gluing of joints. The latter is necessary as a large amount of pressure is generated during the dissolution process, which often causes significant stress on the FP, if joints are not adequately connected the system can fail. Notably, the cost variable during *ex vivo* studies can be significantly reduced through the use of research fluid paths (RFP). These are regarded as more robust than FP as they are not irradiated with an electron beam (for sterility purposes); there is no additional filtering system, producing another point at which clinical FPs could potentially fail. Importantly, RFPs can be prepared in conventional labs, unlike FPs which require Good Manufacturing Practice (GMP) facilities, which incur significant cost. Considering the above the greatest limitations of d-DNP are the current quality of FPs and the short relaxation times of the hyperpolarised signal, although both PHIP and SABRE are subject to the latter variable. Despite this, work is ongoing to continue refining the stability of clinical FPs. Whilst hyperpolarised clinical trials using d-DNP are continuing, the cost associated with

each individual experiment means that optimising acquisition parameters and understanding how to get the best SNR is essential.

Parahydrogen Induced Polarisation

PHIP involves the nucleophilic addition of parahydrogen to an unsaturated species, in the presence of a heavy metal catalyst; the former's asymmetric addition induces a significant spin polarisation (Figure 9) [9], [10]. This polarisation can be transferred in an intramolecular manner via Spin-Order Transfer sequences (SOT) or field cycling to a ^{13}C nuclei [11], [12]. This polarisation transfer allows for the use of ^{13}C species as hyperpolarised contrast agents [10].

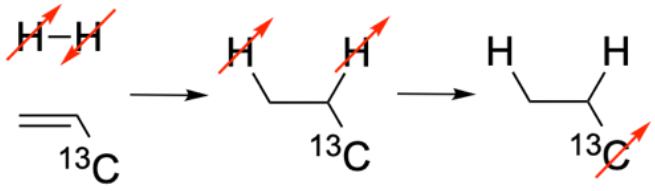

Figure 9 – Parahydrogen Induced Polarisation (PHIP), arises from the reaction of parahydrogen (far left) with an unsaturated version of the final target molecule. Upon nucleophilic addition (middle) the polarisation can be transferred to the carbon-13 labelled nuclei (right).

An initial limitation of PHIP was the production of hyperpolarised small molecules analogous to naturally occurring biomolecules, such as diethyl 1-^{13}C-succinate as PHIP would require reduced forms of such agents to undergo nucleophilic addition of parahydrogen[13], [14]. This was overcome by the development of sidearm hydrogenation (SAH); the addition of the parahydrogen molecule to a vinyl-ester species, such as vinyl acetate, afforded the generation of hyperpolarised species such as acetate, lactate and pyruvate [15], [16]. Whilst SAH does afford the fast generation of hyperpolarised biomolecules, there is still a need for somewhat complex, ^{13}C precursors contributing to an increase in the overall cost of the technique [17]. Another limitation, still prevalent, is the need to remove the heavy-metal catalyst. Whilst a rhodium catalyst's low toxicity allows for PHIP hyperpolarised solutions to be used in animal studies, if it is to be used in a clinical setting a filtering and purification step, prior to injection will be required. To overcome this, a PHIP method

wherein hyperpolarisation and polarisation transfer occur in an organic solution, eliminating the need for heavy-metal catalysts has been developed [10].

^{13}C-PHIP has been seen to be capable of polarising samples up to 25% [18], [19]. Hyperpolarisation and spin polarisation transfer occurs instantaneously, the equipment required is deemed to be relatively inexpensive when compared to other polarisation methods (such as d-DNP) and the procedure generally more reliable. Despite this, as with d-DNP, the hyperpolarised state does not last very long with the hyperpolarised state decaying in the order of several minutes [13], [17], [20].

Signal amplification by reversible exchange

SABRE eliminates PHIP's need for the addition of parahydrogen to an expensive unsaturated starting material (Figure 10).

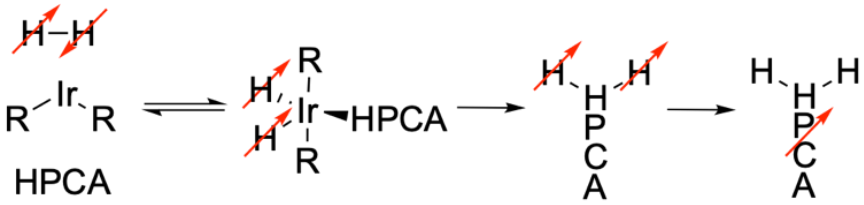

Figure 10 – Parahydrogen (H-H), and a hyperpolarised contrast agent (HPCA) are added to a metal catalyst such as ^{94}Iridium (R-Ir-R). The metal complex facilitates the hydration of the HPCA, with Spin-Order Transfer sequences used to transfer the polarisation (red arrow) from the hydrogen atoms to HPCA.

This method involves the simultaneous addition of parahydrogen and the target molecule to a metal catalyst (Ir^{94} is commonly used) [21]–[23]. After hydration, SOT sequences and field cycling allow for polarisation transfer to occur [23], [24]. Whilst the need for complex precursors is eliminated, for use in a clinical setting the heavy-metal catalyst would still need to be removed prior to injection. Similarly, to PHIP, SABRE methods for hyperpolarisation in aqueous media have been demonstrated, although these would still require the removal of the heavy-metal catalyst [25]–[27]. A significant advantage of SABRE is that the process can generate hyperpolarised samples with long-lived spin states, which exhibit a relaxation period greater than 20

minutes, a feat which is yet to be seen with other polarisation methods [7], [25]. Such relaxation times make the viability of such hyperpolarised agents similar to that of commonly used radioactive species for PET imaging. The method is as cost effective as PHIP and in some cases, depending on the molecule being polarised, it can be cheaper with polarisation levels of up to 50% have been observed [26], [27]. Another benefit of the method is the short time frame required for polarisation, with it taking approximately 1 minute to hyperpolarise samples [26], [27]. Despite the methodology's promise, *in vivo* studies have yet to be conducted, largely due to toxicity issues arising from the use of the catalyst, but also as the method has only recently begun to be adopted in a widespread manner. Automated SABRE systems have only recently been developed in academia, with no commercially available systems at the time of writing. The method's translation to clinical use faces many hurdles; nevertheless, the promise it shows is great [28].

Spin-Exchange Optical pumping

SEOP allows for the hyperpolarisation of noble gases such as ^{3}He and ^{129}Xe. Circularly polarised light of a specific wavelength is used to excite electrons on a metal catalyst (typically Rubidium), the relevant noble gas is then directed at the catalyst with collisions between the two forcing a transfer in spin polarisation (Figure 11) [29]. Clinical MR studies involving SEOP are ongoing with several demonstrating lung and brain imaging [30], [31].

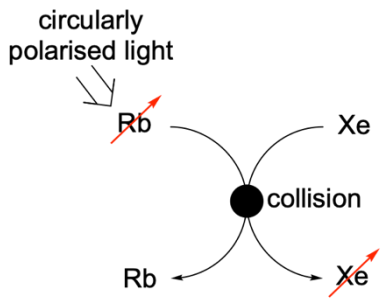

Figure 11 – Electrons on a metal catalyst such as Rubidium (Rb) are polarised with circularly polarised light. Noble gases such as ^{129}Xenon (Xe) are then combined with the catalyst forcing collisions which result in polarisation transfer.

The work described in this thesis employed the use of d-DNP for both preclinical and clinical hyperpolarised ^{13}C-MR studies. [1-^{13}C] pyruvate was exclusively used as a hyperpolarised agent, with polarisation performed on a GE SPINLab Hyperpolariser unit, via both RFPs and FPs.

Chapter 2: Clinical Hyperpolarised ^{13}C-MR

A number of clinical hyperpolarised ^{13}C-MR studies, implementing a range of sequences, have been performed since the first *in vivo* scans [1]. In patients with cancer, such studies offer a window into investigations of the Warburg effect (the preferred cellular metabolism of pyruvate into lactate over aerobic respiration)[1], [2], [32].

Pulse sequences used in hyperpolarised ^{13}C-MR

A limitation of hyperpolarised ^{13}C-MR is the short effective half-life and irreversible decay of the signal from the hyperpolarised agent, with that of [1-^{13}C] pyruvate observed as ~30 s *ex vivo* [33], [34]. Unlike conventional MR, the hyperpolarised signal does not recover; as a result, there is a need for specialised MR acquisition methods (pulse sequences) that provide the requisite combination of spatiotemporal and spectral resolution.

Several pulse sequences can be considered [35], [36]. Non-localised spectroscopy provides high spectral and temporal resolution, but it yields a single spectrum from a region that is defined by the sensitivity profile of the MR receiver coil [1]. Chemical shift imaging (CSI) enables signals to be spatially resolved but has a relatively poor temporal resolution [2], [36] [37]. Echo Planar Spectroscopic Imaging (EPSI) sequences afford improved temporal resolution but have limited spectral bandwidth, and they are particularly prone to errors caused by susceptibility gradients at air/tissue interfaces such as those which occur with prostate imaging procedures [38], [39].

Another possible approach employs the Dixon technique, invented for fat-water separation in ^{1}H-MRI [40], [41]. This approach involves the

acquisition of echo images at symmetric echo times, and it allows for the reconstruction of metabolite-specific chemical shift maps [40], with spectral resolution limited by the number of acquired echo images and reconstruction parameters [42]. If only a few metabolites are expected, and there is *a priori* knowledge of the chemical shifts, this technique is faster than EPSI.

The balanced steady-state free precession (bSSFP) sequence is widely used in anatomical MRI as it affords high spatiotemporal resolution and signal-to-noise ratio (SNR); many vendors are offering a rendition of the sequence (e.g., TrueFISP (true fast imaging with steady-state precession – Siemens), FIESTA (fast imaging employing steady-state acquisition – GE), and Balanced-FFE (balanced fast-field echo – Philips)). This sequence, adapted with a bipolar multi-echo (ME) balanced gradient readout and Dixon type post-processing, could provide an optimal balance of spectral sampling, spatial resolution, and overall acquisition time in hyperpolarised ^{13}C-MR studies [41], [43], [44]. Previous preclinical studies demonstrated this sequence in both phantom and animal subjects, successfully analysing the conversion of hyperpolarized [1-^{13}C] pyruvate into [1-^{13}C] lactate [44], [45].

A 3D variant of a previously described ME-bSSFP sequence (Figure 12) was used in this work with a slab-selective, sinc-shaped excitation pulse of flip angle (FA) α/2, followed by refocusing pulses of FA α with alternating polarity (±) [44]. Between 5 and 10 dummy cycles at the beginning of the pulse sequence were used to create a transient transverse magnetization [46]. A Cartesian centre-out k-space readout trajectory was employed with ($N_p \times N_s$) phase and slice encoding steps, and a bipolar multi-gradient-echo readout centred between refocusing pulses to acquire N_e consecutive echoes separated by a fixed difference in TE (ΔTE). An α/2 flip-back pulse, played out at the end of the sequence, transferred remaining transversal magnetization (M_T) back into longitudinal magnetization after the end of each scan [41], [44].

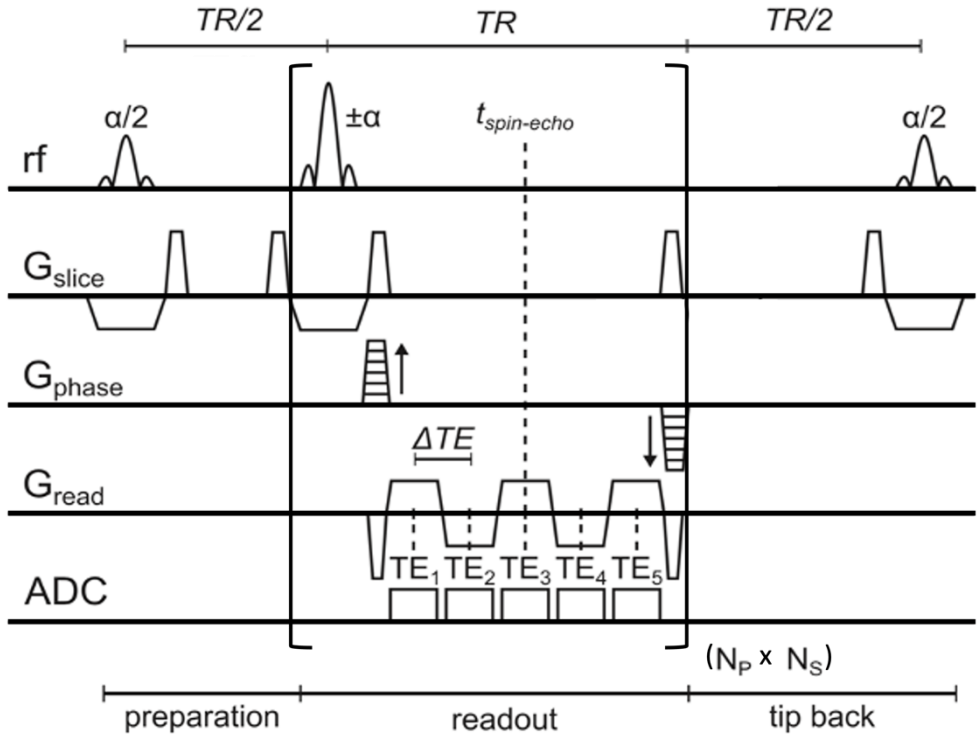

Figure 12 - Pulse sequence diagram for a ME-bSSFP sequence. A slab-selective excitation of α/2 and dummy cycles of ±α refocusing pulses were used for magnetisation preparation. The acquisition part is built of a bipolar gradient multi-echo readout with N echoes separated by ΔTE and centred around TR/2. Repetitions of the readout over the number of phase and slice (N_P and N_S) encoding steps result in a total acquisition time of $N_P \times N_S \times TR + 2 \times (TR/2)$.

Quantifying hyperpolarised ^{13}C-MR

Another significant challenge in hyperpolarised ^{13}C-MR studies regards the quantification of data obtained during such studies. The decaying nature of the hyperpolarised state affords the possibility of dynamic imaging which, in turn, allows for two distinct types of analysis to be performed. The first a graphical approach, analysing the direct change in metabolite signals within a voxel(s), as a function of time. The second involves the temporal modelling of enzymatic rate constants which describe the rate of reactions of specific enzymes involved in interacting with the hyperpolarised agent.

When analysing data obtained during hyperpolarised ^{13}C-MR studies metabolite maps are generated, with the maximum signal intensity of each relevant metabolite calculated on a voxel wise basis across the entire imaging volume. This is then repeated for each time point of the acquisition [47]. Typically, regions of interest (ROIs) are then drawn to

focus on a particular area of the anatomy, with the change in metabolite signals then plotted graphically as a function of time.

The aforementioned graphical methods (Figure 13) rise from the analysis of various features of the changing signal time course. This can vary from quantifying: the maximum signal to noise ratio (SNR) of individual metabolites, the sum of the SNRs over a period of time, the time at which a particular metabolite signal peaks or the rate of metabolite uptake. Another method (13f) involves deriving the rate of enzyme turnover (k_P), via an estimate of the T1 for pyruvate using the time taken for the lactate SNR to go from and back 0.8 (α) times its maximum value; wherein $k_P = (SNR_{MaxLac}/SNR_{MaxPyr})/T1_{Pyr}$.

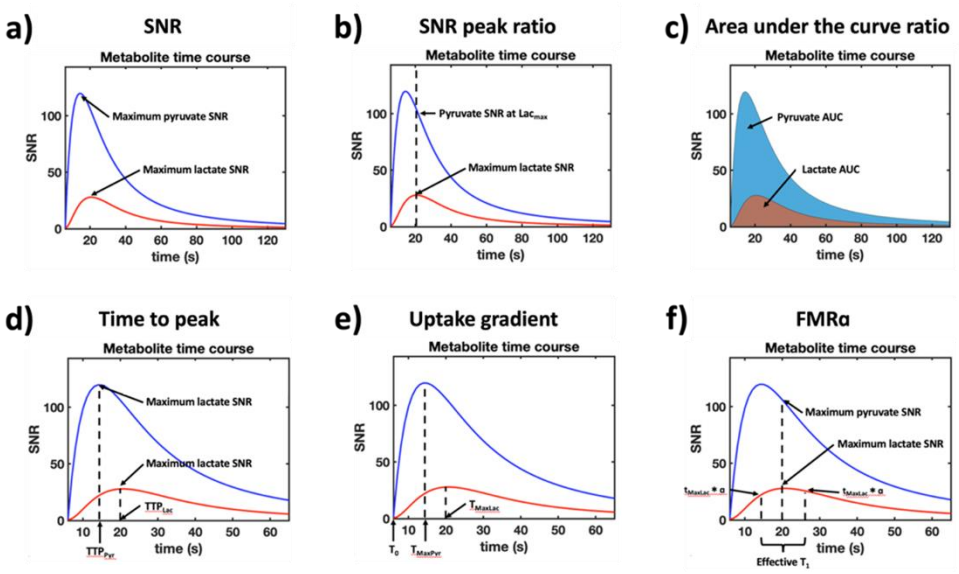

Figure 13 - Graphical methods used to analyse metabolite time course data obtained during hyperpolarised ^{13}C-MR studies. This includes the maximum metabolite SNR (a); the ratio of maximum metabolite SNRs (b); the ratio of the total metabolite SNRs between two species of interest (c); the time taken to reach the maximum SNR for a particular metabolite (d); the time taken for a metabolite to reach its maximum as a function of SNR (e) and the estimation of an enzyme rate constant through the ratio of maximum metabolite SNRs (f).

Kinetic analysis methods (Figure 14) implement models which consider the change in metabolite signals to estimate specific rate constants exhibited by enzymes relevant to the metabolic processes. Such models comprise of differential equations which describe the conversion of metabolites via specific enzymes.

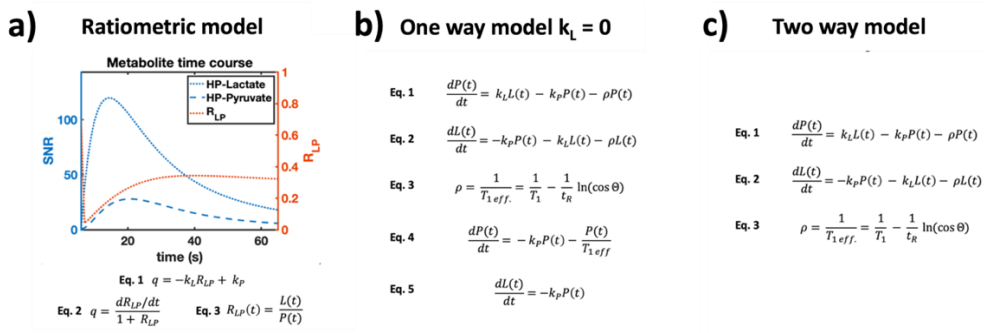

Figure 14 - Kinetic models can also be produced by passing metabolite data through differential equations which describe the enzymatic conversion of one substrate into another. The shown models describe how the enzymatic constants kP and kL for the forward and reverse reactions facilitated by LDH, are calculated, by using the changing lactate (L) and pyruvate (P) SNRs, with respect to time (t). Examples of these include a radiometric model (a) which uses the equation of the line produced by the ratio of metabolite signals (R_{LP}). (b) describes a model representative of the enzymatic reactions facilitated by the enzyme LDH, however the rate of the reverse reaction kL is assumed to be 0, this model also relies on assumptions of the T1 decay rate, the repetition time of the pulse sequence used (t_R) and the flip angle applied (θ). Another kinetic model is described (c) which also describes the differential equations the LDH enzyme, however, in this instance both the forward (kP) and reverse (kL) reaction constants are explicitly calculated.

The conversion of pyruvate to lactate through the enzyme lactate dehydrogenase (LDH), which allows for the quantification of two rate constants, kP and kL, representative of the rate of enzyme turnover for the forward (pyruvate to lactate) and reverse (lactate to pyruvate) reactions respectively.

The ratiometric model (14a) uses the changing ratio (RLP) of lactate (L) to pyruvate (P) SNRs, as a function of time to identify a steady state from which a line of best fit is calculated, the gradient of which is derived a kP and the y-intercept is kL. This methodology, however, requires a high temporal resolution, allowing for enough data points to be extracted to calculate the aforementioned line of best fit for the steady state.

The one-way kinetic model (14b) assumes that the reverse reaction is negligible (kL= 0), which allows for the coupled differential equations to be simplified into: -dL(t)/(dt *P(t) = kP, this is unlike the two-way model (14c) considers the reverse reaction (kL ≠ 0). These methods

are highly desirable when accurate fitting is desired, however, these can be both computationally intensive and time consuming.

Previous studies have recommended the use of either of these techniques, with one such finding an 'area-under-the-curve ratio' (AUC) of metabolites to be closely reflective of enzymatic activity [48]. A clinical study adapted this methodology to correlate tumour Gleason grade with lactate AUC [49]. Another study highlighted the potential limitations of this approach, including how it was only appropriate if the entire reaction, i.e., pyruvate uptake, as well as decay, is captured [44].

A phantom study concluded the time to achieve the maximum lactate signal within a voxel(s) (time to peak - TTP) correlated well with enzyme concentration across a range of concentrations, with a kinetic model estimating both the forward (k_P) and reverse (k_L) enzyme rate constants for the conversion of pyruvate via LDH, being a close second [47]. A clinical study found a similar kinetic model to conform most with increasing Gleason grade [50].

Identifying an optimal metric in a clinical setting is difficult without significant reproducibility studies. Similarly, phantom studies which do not demonstrate significant experimental reproducibility also present a limited interpretation. The variability across these studies has made it difficult to achieve a consensus on an optimal metric. The development of a highly reproducible phantom system could present an opportunity to identify such a metric.

There is clearly a need for a phantom platform to perform standardised experiments, as well as a pulse sequence which can maximise the quality of data obtained during hyperpolarised ^{13}C-MR studies.

Chapter 3: Phantoms in Hyperpolarised ^{13}C-MR

Attempts at clinically translating hyperpolarised ^{13}C-MR are ongoing; one challenge involves the need for test objects for pulse sequence optimisation and testing. At present, the most efficient pulse sequence for use in hyperpolarised ^{13}C-MR studies has yet to be identified, although several avenues are being explored, from balanced Steady-State Free Precession (bSSFP) to spectral-spatial excitation [38], [51]. To fully quantify the efficiency of these pulse sequences and understand the best way to quantify hyperpolarised ^{13}C-MR studies highly reproducible and stable platforms, in the form of phantoms, are required.

A variety of phantoms are widely used, and for the purposes of this chapter, they are categorised into two groups: static and dynamic phantoms, Firstly, static phantoms can be employed for a variety of purposes including: sequence parameter optimisation and the quality assurance of experimental setups [44], [52]. Dynamic phantom systems are specifically designed to allow for the replication of *in vivo* processes involving hyperpolarised agents [44], [53]–[55]. Within these groups there is further diversity in the types of phantom used. Presently, the field has no gold standard design regarding a phantom for use in hyperpolarised ^{13}C-MR studies. This chapter evaluates the uses of these different types of phantoms, commenting on their features, benefits and shortcomings, as well as recommending a set of criteria which an ideal set of phantoms must meet. Establishing these measures will allow for the development of standardised phantoms which will have the potential to make sequence optimisation and testing comparable between different sites [56]. In turn, this could allow for the eventual identification of an optimal sequence and metric for quantification for use in hyperpolarised ^{13}C-MR studies.

Static phantoms

'Static' phantoms used in hyperpolarised ^{13}C-MR studies can be described as test objects containing one or more carbon-13 labelled materials used for a variety of applications including: sequence parameter optimisation, coil positioning, signal quantification and for processing data [44], [57].

The need to acquire data quickly, with greater planar resolution and in a 3D manner is reflected by the widespread research aimed at developing novel pulse sequences in hyperpolarised ^{13}C-MR [39], [58], [59]. The development and optimisation of these sequences require static phantoms for validation of *in silico* models; at present, phantoms of different sizes and chemical compositions are used to this end [44], [60]. The size of the phantom used is dependent on the receiver coil used, the field of view of the sequence being tested and also, the tumour type being investigated. The metabolites within the static phantoms are also dependent on the chemical species being hyperpolarised [61].

Several smaller phantoms (diameter 5-10mm) have been described, with these test objects used to test the stability and reproducibility of pulse sequences [47], [61]. These smaller phantoms are often used in conjunction with surface or endorectal coils to mimic metabolite signals from lesions *in vivo*, with a focus on sequence sensitivity and defining sensitivity thresholds [61]. Larger test objects have also been demonstrated, with the most commonly used being head shaped enriched ethylene glycol phantoms [62].

Static phantoms have also been used in hyperpolarised ^{13}C-MR experiments, in both human and animal studies [63], [64]. Here static phantoms can be used for coil positioning, where the phantom is typically built into a coil and used as a spatial reference to align the coil as close to the site of interest as possible [1], [55]. These phantoms are also used for quantification by means of associating signal to noise ratio (SNR) of the thermally polarised species with its

known concentration. Many animal studies involve placing a static phantom next to the subject being injected, with the static phantom typically contains [1-^{13}C] lactate, [1-^{13}C] acetate and [^{13}C] urea, as potential reference compounds with SNR quantification being demonstrated in several instances [62].

The most widely used static phantom in clinical studies, involves a [1-^{13}C] urea phantom, built into most endorectal coils, which are used in hyperpolarised ^{13}C-MR prostate studies, with several sources illustrating the benefits of phantoms within coils, which include coil positioning and signal quantification [62], [65].

Static phantoms are also used for coil power calibration and testing [1], [66]. Over time the voltage output by a coil when transmitting and receiving during MR studies has been shown to change. Static phantoms are widely used to recalibrate coils, whilst also being used to adapt amplifier and receiver coil settings for use with novel pulse sequences [65], [67].

Another benefit of including thermally polarised phantoms within the field of view, during hyperpolarised ^{13}C-MR experiments is that they can provide a reference point for data reconstruction, during post-processing [68]. The most commonly used static phantom in animal studies is [1-^{13}C] lactate, whilst in human studies this tends to be [1-^{13}C] urea, as described earlier [1], [62]. Essentially, during pulse sequence optimisation the frequency difference between the metabolites of interest, typically represented in static phantoms, is quantified. After successfully identifying these frequency offsets, only a singular phantom is required as a reference during hyperpolarised ^{13}C-MR experiments for centre frequency positioning and subsequent data reconstruction [44], [65]. Without this reference point, during hyperpolarised ^{13}C-MR experiments, the acquisition centre frequency cannot be suitably placed, resulting in the entire process being potentially missed. Similarly, during post-processing reference frequencies are required for data reconstruction [55].

An ideal static phantom should possess several compartments, containing at least two metabolites; the concentrations of the metabolites between compartments should also vary. This would allow for a phantom suitable for assessing sequence stability, homogeneity, and linearity.

Dynamic phantoms

Dynamic phantoms are test object used to replicate metabolic processes, such as the Warburg effect in an *ex vivo* environment. Referred to as 'dynamic' in nature due to their ability in allowing for the analysis of reactions with signals which change as a function of time. These custom-made phantoms avoid the use of animal subjects and in some instance have been observed to be more reproducible platforms than animal studies [53]. Dynamic phantoms allow for the analysis of enzyme kinetics regarding the conversion of metabolites, proof-of-concept testing of different MR pulse sequences, as well as the optimisation of logistical operating procedures [54]. Furthermore, these test objects can be used to derive a metric by which hyperpolarised MR can be quantified in a clinical setting [47]. In order to achieve these objectives, however, highly reproducible systems are required.

The simplest of these dynamic phantoms is the falcon tube approach used to optimise operating procedures and quantify enzyme kinetics [47]. This involves filling a falcon tube of known volume with an enzyme suspended in a buffer and adding a hyperpolarised agent. This approach is cheap and effective as it affords proof of concept data for different pulse sequences to be used to analyse a variety of enzymatic processes. It allows for the optimisation of the steps taken during the manual processes during d-DNP, such as the transfer of the hyperpolarised solution to the MR scanner. The method also involved using metabolite concentrations similar to that in patient's

blood, making the phantom methodology more analogous to *in vivo* conditions [1], [47].

A conceptually similar phantom, involves the use of an NMR tube, filled with enzyme solution and injected with hyperpolarised solution [69]. These phantoms whilst difficult to use in MR scanners are more suited to NMR spectrometers. They do, however, still provide a platform on which operating procedures can be optimised and enzyme kinetics quantified [69].

In both types of phantom, considering the relaxation time of the hyperpolarised signal and that the chemical conversion was already underway before scanning/measuring begins, it could be assumed that a potentially significant portion of the process is being missed. This is largely as, mixing in both cases was performed manually, through the shaking of the vessels containing the hyperpolarised and enzyme solutions. The mixing processes involved removing the reaction vessel from the scanner/spectrometer to allow for injection and manual shaking. As such the chemical conversion of the metabolites begins before scanning/measuring begins.

The phantoms, whilst simple to use and cheap, have more limitations, largely concerning reproducibility. Several factors compromise reproducibility, such as phantom placement in the case of the falcon tube; the tube needs to be removed from the scanner prior to injection, repositioning the phantom in the exact same position without compromising field homogeneity between scans may prove challenging. Offline injection of the hyperpolarised solution in both cases means that hyperpolarised signal is lost during the injection and mixing processes. Moreover, there is no mechanism in either instance to mix phantom contents evenly; as the process is done by hand uneven mixing may compromise quantification. As a qualitative measure of the viability of monitoring a metabolic process or as a proof of concept when testing a novel sequence, the falcon tube and NMR tube are ideal; for more quantitative studies the aforementioned limitations need to be addressed.

A sled style metabolic phantom with a 3ml internal volume has been observed [53]. The phantom contained injection and exhaust ports, eliminating the need for removing the phantom from within the MR scanner, the study which first proposed this system, however, did not integrate automated injection. The hyperpolarised solution ([1-^{13}C] pyruvate) and lactate dehydrogenase (LDH) enzyme solution were mixed before injecting into the phantom and the procedure repeated seven times. The coefficient of variation regarding the ratio of lactate to pyruvate was derived as 12% with the study comparing variations in animal studies finding the phantom to be more reproducible. This phantom provided confirmation that a suitable architecture could be developed to analyse metabolic processes in an *ex vivo* environment via hyperpolarised MR. This method is not without its limitations. The hyperpolarised pyruvate was injected into the phantom, followed by another injection of enzyme solution. There is a distinct possibility, as the same injection lines where used for both solutions that mixing occurs and that the reaction begins before the enzyme solution reaches the phantom. This makes establishing suitable kinetic models from this methodology problematic. Considering the relaxation time of the hyperpolarised signal and the fact that the chemical conversion could be underway before scanning begins, it could be assumed that a potentially significant portion of the reactions were being missed. The main point of progression made with this phantom involved the introduction of a system where the need to remove system from the scanner was eliminated [53]. Whilst benefiting from remote injection, manual injection led to high variations in the end concentration of pyruvate, further reiterating the need for automated injection.

A multicompartment dynamic phantom was produced from three Eppendorf tubes [70] One compartment contained an LDH enzyme solution based on previous dynamic phantom work [53]. Another was filled with hyperpolarised [1-^{13}C] pyruvate, whilst the last contained water for coil loading. This dynamic phantom is the first of its kind to allow for the observation of the natural decay of the hyperpolarised [1-

^{13}C] pyruvate signal, as well as it's enzymatic conversion into [1-^{13}C] lactate, simultaneously. The natural decay of the solution allows for a useful reference standard by which to quantify both polarisation and enzymatic conversion across the entire acquisition time frame. This system, however, does not benefit from remote injection and requires removal from the scanner for injection of the solution. As such, all of the previously described issues which arise with the falcon and NMR tube are observed [47], [69]. Adapting this system so that it has the capacity for remote and automated injection could produce a reliable, and reproducible dynamic phantom.

Another multicompartment dynamic phantom was constructed, this time with the capacity for remote injection [54]. This phantom's key feature was the presence of two 3ml chambers within a 50ml syringe, allowing for two reactions to be observed simultaneously. The presence of a reference module containing [^{13}C] urea within the phantom allowed for more precise slice positioning prior to scanning. Reproducibility data for this system showed a 15-20% variability in the ratio of lactate to pyruvate across measurements, with reduced precision in comparison to the sled style phantom [53]. Despite this the multiple compartments allow for the more effective use of the hyperpolarised solution. The latter is produced in approximately 40ml batches when clinical samples are prepared, whilst prior metabolic phantoms used <1ml at a time, this phantom could be used to process up to 5ml of polarised agent depending on the solution concentration [44], [47], [53], [54], [69], [70]. This phantom and the methodology used to operate it, are not without their shortcomings [54]. As with the sled phantom the hyperpolarised and enzyme solutions are mixed prior to injection, potentially missing out on a significant portion of the chemical process [53], [54]. Data acquisition, however, begins prior to injection which maximises the potential amount of data acquired.

An ideal dynamic phantom would possess multiple chambers, allowing for a singular reaction, with several different concentrations to be observed simultaneously. This system would also have an additional

chamber into which only hyperpolarised agent would be injected, to observe its natural decay. These chambers would also need to benefit from remote and automated injection, eliminating several of the issues highlighted earlier, associated with removing the phantom from the scanner. This system should also have a chamber containing a reference static phantom, for quantification, coil testing and positioning purposes.

Enzymes are often used to mimic *in vivo* processes, whilst producing a good measure of how pulses sequences can be used in hyperpolarised ^{13}C-MR, they do not fully represent the complex, multienzyme systems found *in vivo*. Commonly used enzymes to in hyperpolarised ^{13}C-MR studies include LDH, Carbonic Anhydrase (CA) and Fumarate Hydratase (FH) [47], [71], [72]. The primary limitation of using enzymes in dynamic phantoms is their sensitivity to their environment. Enzyme activity is influenced largely by pH and temperature, raising significant concerns during hyperpolarised ^{13}C-MR studies as the final hyperpolarised agent, can often have variable pH and temperature [73]. For clinical translation, a sequence must be highly reproducible, to observe this, a dynamic phantom which is limited by the influence of temperature and pH is required.

Chemical catalysis is widely agreed to be more stable, reliable and reproducible than enzyme catalysed reactions. Largely due to a number of factors, as previously mentioned, such as pH, temperature, and enzyme stability [73]. The kinetics of chemical catalysis, whilst affected by pH and temperature can be more closely controlled through substrate and catalysis production. A hyperpolarised ^{13}C-MR study involving the chemical catalysis via hydrogen peroxide, of hyperpolarised [2-^{13}C] pyruvate into [1-^{13}C] acetate has been proposed [74]. The study involved several repetitions, with and without hydrogen peroxide, with phantom experiments being validated through an animal study. It found that the chemical conversion both *ex vivo* and *in vivo* was only limited by the initial concentration of the [2-^{13}C] pyruvate. The reproducibility of the procedure was quantified by

analysis of the hyperpolarised [1-^{13}C] acetate species' T_1, with little variance seen (47.7±0.5s). This work demonstrates the potential for an interesting step towards more reproducible experiments in the use of dynamic phantoms during hyperpolarised ^{13}C-MR studies.

Phantoms have many applications in hyperpolarised ^{13}C-MR studies. For clinical translation and cross-site studies, however, a standardised platform with both static and dynamic components, as described above, is necessary.

Chapter 4. Thesis Aims

This thesis will describe four areas of study, described in Chapters 6-9. The overarching theme of this thesis is the application of hyperpolarised ^{13}C-MR in clinical studies. Previous studies have demonstrated this in several instances. This body of work differs through its development of a reproducible phantom for testing and quantification purposes. It also describes the optimisation of an existing Multi-echo balanced Steady-State Free Precession (ME-bSSFP) sequence for use in hyperpolarised ^{13}C-MR studies.

Chapter 5: Dynamic Phantom Development

Having considered the limitations of previously described dynamic phantoms (Chapter 3), this chapter sought to:

- Develop a phantom which is compatible with most power injectors found in MR scanner rooms
- Through this create a system which is capable of remote and automated injection, eliminating the need to remove the phantom from the scanner to introduce the hyperpolarised contrast agent
- Quantify the system's reproducibility

Chapter 6: ME-bSSFP sequence optimisation

Observing the previous work done with ME-bSSFP experiments (Chapter 2), this work aimed to:

- Validate an existing ME-bSSFP simulator
- Identify optimal imaging parameters for hyperpolarised ^{13}C-MR studies of PCa

Chapter 7: Application of optimised ME-bSSFP with hyperpolarised ^{13}C-MR in subjects with prostate cancer

This chapter aimed to apply the optimised sequence identified in chapter 6 in a hyperpolarised ^{13}C-MR study with 5 patients. Specific aims include:

- Testing if it is possible to observe hyperpolarised signals in the prostate
- Identifying if there are statistical differences between healthy and tumourous tissue

Chapter 8: Metabolic imaging of pheochromocytoma

This chapter outlines a case study where a single subject with pheochromocytoma underwent an injection of hyperpolarised [1-^{13}C] pyruvate, with ^{13}C-images acquired using the ME-bSSFP sequence described in chapter 6. This chapter sought to:

- Test if hyperpolarised signals can be observed in pheochromocytoma
- Identify if there are differences, if any, between different tissue types in tumours

Section B

This section describes two areas of original preclinical research, the culmination of which is applied in the clinical research presented in section C.

The first of the chapters in this section, Chapter 5, describes the development of a novel dynamic phantom which aims to integrate an automated, remote injection system for contrast delivery. The key aim of this project was to develop a phantom with greater reproducibility than previously demonstrated.

The last chapter in this section, Chapter 6, explores the spatial and spectral optimisation of an ME-bSSFP sequence, as well as the testing of the optimised parameters identified, via the phantom developed in Chapter 5.

Chapter 5: Dynamic Phantom Development

For the following results chapter, the author of this thesis designed and manufactured the described phantom. During the mixing experiments the author had assistance from an experienced radiographer to identify an appropriate imaging sequence for the study, after which the author performed the remaining experiments. For the experiments involving hyperpolarised contrast the author filled the phantom, built research fluid paths, filled with pyruvate which underwent hyperpolarisation and set up both the phantom within the MR scanner and the carbon-13 acquisition protocol. During the experiment, the author had help from a research technician who extracted the hyperpolarised pyruvate from the polariser, as well as a radiographer who was operating the power injector.

Aims

For the phantom designed in this work we considered the following as essential points for its design:

- Automated remote injection avoids the need to remove the phantom from the MR scanner – in previous instances this was necessary, with the process contributing to potential field inhomogeneities. This also contributes towards reproducibility as a consistent amount of hyperpolarised agent can be introduced to the system between experiments.
- A remote and automated injection system is not enough and a mixing mechanism which disperses hyperpolarised agent throughout the phantom in a reproducible manner is also needed.
- A high level of reproducibility is required to afford a degree of consistency across experiments, ensuring that the changes made to our pulse sequence are the only contributing factor to any variance observed.

Background

Optimised pulse sequences require testing before use in large scale clinical trials. Testing in humans presents a large financial cost, especially in hyperpolarised ^{13}C-MR studies, requiring clinical grade equipment and clean rooms for material preparation. Whilst clean rooms are not necessary in animal testing and costs in comparison to human testing are lower, the variability between subjects and the ethics surrounding animal testing can pose some issues. As such, *ex vivo*, highly reproducible, yet cheap to produce and maintain systems are required for testing optimised pulse sequences. In the context of dynamic imaging, as is the case in hyperpolarised ^{13}C-MR, this need is met by dynamic phantoms. Here we propose a design which addresses some of the previously described limitations of dynamic phantoms (Chapter 3).

Methods

The phantom was designed using Fusion 360 (Autodesk, California, USA) and created using ULTEM (Plastock, High Wycombe, England). Mixing and automated injection testing was performed on a Philips Achieva 3T system (Philips Healthcare, Amsterdam, Netherlands), using a dStream, transmit/receive, 16-channel knee coil (Philips Healthcare, Amsterdam, Netherlands). Non-localised ^{13}C-MR spectroscopy experiments were performed on a Philips 3T Ingenia (Philips Healthcare, Amsterdam, Netherlands), using a single loop flex coil (RAPID Biomedical GmbH, Rimpar Germany). ^{13}C-MR images were acquired on a Siemens Biograph mMR 3T system (Siemens Healthineers, Erlangen, Germany), using an endorectal, receive-only coil (RAPID Biomedical GmbH, Rimpar, Germany). In all instances a MEDRAD Spectris Solaris EP MR injection system (MEDRAD, Pennsylvania, USA) was used to deliver contrast. All chemicals used in this study were sourced from Merck (Merck KGaA, Darmstadt, Germany). Data processing was performed using MATLAB (Mathworks, Massachusetts, USA), with custom, in-house data processing tools.

Phantom design

The dynamic phantom built for this study was composed of two sections, the body, and a lid, with the components making up each section described below:

- The main compartment was machined from cylindrical (⌀52mm/thickness: 35mm) ULTEM stock, with the exterior planed and the interior bore formed using a Chester lathe. Two sides of the exterior were flattened to avoid the phantom rolling during data acquisition and to allow for consistent positioning between experiments. A ⌀12.5mm hole was drilled on top of the phantom and an outlet designed and added, in the form of a ¼” male luer lock. Four further ⌀2.3mm holes were added to the open face, perpendicular to the outlet to position nylon screws, to allow for the lid to be fixed to the main compartment. Finally, an additional

groove (inner ⌀26mm/outer ⌀34mm) was machined on the same face to accommodate an O-ring which will provide a watertight seal between the lid and body.

- The lid (thickness 10mm) was produced from the same material as the body, and was machined in a similar manner, with two sides planed and four ⌀2.3mm holes were added. An additional ⌀12.5mm hole was made on the lid's largest face and an inlet, in the form of a ¼" male luer lock added. Upon the inlet being mounted a ⌀8mm nylon tube (length: 35mm) was hollowed out (internal ⌀4mm) and four additional holes added (Figure 15).

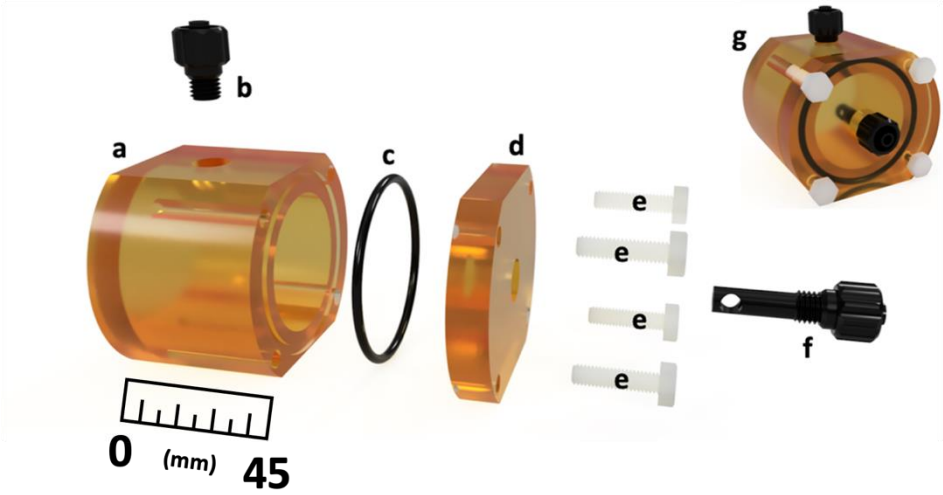

Figure 15 - Visualisation of the dynamic phantom, created and rendered in Autodesk's Fusion 360 – a) main body of the phantom, with a hole for b) a ¼" threaded male Luer lock outlet and a groove for c) a nitrile O-ring. d) The lid is fixed to the main body via e) four 6,6-Nylon M3 screws, whilst an additional hole was added to the lid to allow for f) a custom inlet to be fitted

A nitrile O-ring was placed between the lid and the body. These were fixed to each other through the use of four 6,6-Nylon screws. The phantom in this state is now ready to be filled and connected to any clinically used injection pump, using standard luer connectors. The cleaning process requires the removal of the screws, affording access to the entire main compartment. The inlet and outlet are threaded and as such can be unscrewed and removed for further cleaning if necessary.

The use of standardised luer connectors for the inlet and outlet allow for this phantom to be used in conjunction with most power injectors

found in an MR scanner room, affording both remote and automated injection. The internal nylon tube allows for the even distribution of hyperpolarised agent from the direct centre of the phantom. The modular design and ease of disassembly allow for the phantom to be readily reused, affording the repeated use of a system with the capacity for remote and automated injection.

Automated injection and mixing tests

The dynamic phantom was filled with deionised water (25ml), placed within the coil and then connected to a power injector, with two reference syringes placed either side. The injection lines were also filled with deionised water. The first reference syringe contained Gadoteridol (ProHance, 10ml), whilst the second was filled with deionised water (10ml). The dynamic phantom was infused with 4ml of Gadoteridol at varying injection rates. Four injection rates: 1,2,3 and 4ml/s were tested, with each repeated (n = 3), to assess which rate would contribute to the most effective mixing.

Image acquisition began at the start of injection, using a turbo spin echo sequence: FOV: 132x132x75 mm^3, Voxel size: 0.94×0.94×3 mm^3, slice thickness: 3 mm, no. of slices: 25, TR: 5400 ms, ΔTE: 109 ms, ETL: 38, NSA: 1, FA: 90, acquisition time: 6s.

Image uniformity was assessed using a method previously published by the National Electrical Manufacturers Association (NEMA) [75], [76]. This involved drawing regions of interest (ROIs) around the dynamic phantom and the two reference syringes. In each instance the maximum and minimum signals, S_{max} and S_{min} respectively, were identified and used to calculate the percentage image uniformity (Equation 12):

$$\mathrm{PIU} = 100 \cdot \left(1 - \frac{S_{max} - S_{min}}{S_{max} + S_{min}}\right) \qquad (12)$$

Analysis involved drawing an ROI over the dynamic phantom and plotting the change in signal intensity as a function of time, after the injection of Gadoteridol. Signal time courses were normalised to the maximum signal intensity across all rates, to allow for comparison.

Preparation of hyperpolarised [1-^{13}C] pyruvate

A GE SPINLab Hyperpolariser, was used to produce the hyperpolarised [1-^{13}C] pyruvate. [1-^{13}C] pyruvic acid (1.67g) was mixed with AH111501 electroparamagnetic agent (0.0323g) and 0.422g of the subsequent mixture loaded into a fluid path and then placed in the Hyperpolariser (See Appendix A for a detailed explanation of how research fluid paths are prepared).

The acid and EPA mixture was cooled to <1K, forming a uniform glass, which is then irradiated with microwaves for approximately 2h, achieving a polarisation level of 24.9±4.8%. Prior to injection the glass was dissolved with sterile water (38ml) and neutralised with 17.5g sterile trometamol buffer (333mM Tris and 600mM NaOH), affording hyperpolarised [1-^{13}C] pyruvate (250mM, 39.5±1.1ml). The hyperpolarised [1-^{13}C] pyruvate, was loaded into the power injector, with data acquisition beginning at the start of injection.

^{13}C-MR non-localised spectroscopy

The metabolic phantom was filled with varying concentrations (Table 1) of lactate dehydrogenase (LDH), β-nicotinamide adenine dinucleotide (NADH – 0.447g), dissolved in phosphate buffered saline (PBS – pH7.2, 30ml).

Enzyme Conc. (µg/ml)	Experiments performed
1.6	3
3.2	3
4.8	3

Table 1 - The enzyme concentrations used in the HP-MR experiments, and the amount of times the experiments were repeated are shown in the table below.

After filling the phantom with enzyme solution, it was placed in the scanner and connected to a power injector. Hyperpolarised [1-^{13}C] pyruvate is extracted from the hyperpolariser and injected into the phantom (4ml at 1ml/s). At the start of the injection process non-localised spectroscopy (FA: 10°, TR: 1000 ms, BW: 4000 Hz, NA: 1, temporal resolution: 1 s) was used to record the conversion of [1-^{13}C] pyruvate into [1-^{13}C] lactate via LDH. Prior to injection the scanner centre frequency was determined through the use of a 2M [1-^{13}C] acetate phantom. A 31Hz offset was applied to the acetate frequency to centre the scanner to the [1-^{13}C] lactate position. This adjustment was performed to account for the approximate difference between acetate and lactate.

After data acquisition, prior to Fourier transformation, the FIDs were apodised; then, after conversion into the frequency domain a first order phase corrections also applied. Signal to noise ratios (SNRs) were extracted by quantifying the area under the pyruvate and lactate peaks, these were then plotted as a function of time and then dividing this value by the standard deviation of a portion of the spectra where no signal was expected [77]. Baseline corrections were performed on the time courses using the last 10 measurements. The lactate to pyruvate area under the temporal curve (LP_{AUC}) ratio and enzyme rate constant (k_P) for a one directional model ($k_L = 0$) were then calculated for each experiment. The coefficient of variance of the aforementioned metrics was determined and tabulated as a means to gauge the phantom's reproducibility.

^{13}C-MR imaging

Prior to the injection of hyperpolarised [1-^{13}C] pyruvate, the dynamic phantom was filled with a mixture of lactate dehydrogenase (4.8µg/ml) and NADH (4.4mM) in phosphate-buffered saline. Upon the dynamic phantom being filled it was put in the scanner and connected to a power injector (Figure 13). Hyperpolarised [1-^{13}C] pyruvate was then

introduced into the system (4ml at 1ml/s). Prior to injection of the hyperpolarised contrast a turbo spin echo sequence: FOV: 180x140x90 mm^3, Voxel size: 0.7×0.7×3 mm^3, slice thickness: 3 mm, no. of slices: 30, TR: 5400 ms, TE: 109 ms, ETL: 15, NSA: 1, FA: 90; was utilised, in the sagittal and axial planes, to align the dynamic phantom with the most sensitive part of the endorectal coil; guided by a [^{13}C] urea phantom within the coil. Additionally, a dual gradient echo sequence was also obtained for each patient; FOV: 360×360×80 mm^3, Voxel size: 1.4×1.4×10 mm^3 FA: 15°, TR: 329 ms, TE_1: 2.39 ms, TE_2: 7.17 ms, ETL: 2, NSA: 3. At the point of injection a multiecho-bSSFP sequence: FOV: 90×90×80 mm^3, voxel size: 11.3×11.3×10 mm^3, FA: 24°, TR: 15.8 ms, ΔTE: 1.1 ms, NE: 7, NSA: 6; was used. The transmit and receive frequencies were centred on the lactate resonant frequency (Δf = 0Hz) by positioning them +620 Hz from the resonance of the urea (Δf = -620Hz) phantom within the endorectal coil. To avoid alternating chemical shift displacements of the off-resonant metabolites in the bipolar readout, a wide gradient bandwidth of BW_{read} = 1200 Hz/px was utilised. Four consecutive multiecho-bSSFP acquisitions were obtained directly after completion of injection. This was followed by acquisition of a non-localised spectrum using a single non-localised spectrum FA: 10°, TR: 1000 ms, NSA: 1, the main purpose of which was to identify frequencies for metabolite map reconstruction via IDEAL. This was followed by a further four multiecho-bSSFP acquisitions and a non-localised spectrum; this was repeated for a total acquisition time of 2m30s.

Signal to noise ratios (SNRs) were extracted by defining a ‘noise volume’, this involved calculating the standard deviation of signal intensities obtained in the last 5 measurements on a voxel-by-voxel basis. The signal intensity metabolite maps at each time point were then divided by the respective noise volumes, converting them into SNR maps. Regions of interest (ROIs) were drawn around the phantom volume and the change in metabolite SNRs extracted and plotted as a function of time. Baseline corrections were performed on the time courses using the last 10 measurements. LP_{AUC} and k_P were

derived from the time course data. Similarly, to the analysis in the non-localised spectroscopy work, the coefficient of variance of the LP_{AUC} and k_P metrics were calculated and tabulated.

Results

Automated injection and mixing tests

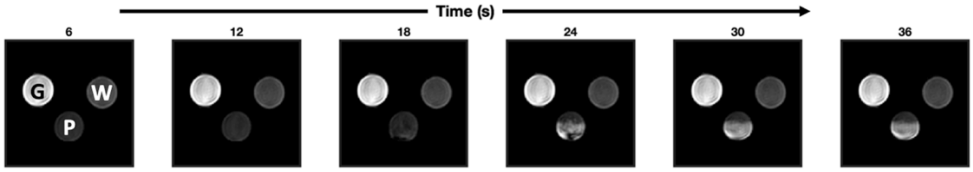

Figure 16 - Change in Signal intensity within dynamic phantom (P) as a function of time, upon the injection of contrast agent at 1mls^{-1}. Gadoteridol (G) and water (W) references are also shown.

The change in signal within the dynamic phantom (P), during the injection of contrast, is demonstrated, for a single slice, in Figure 16. Here we can also see the reference tubes with Gadoteridol (G) and water (W). The mixing process is complete within 30s. The end of the mixing process was defined as the time point at which the signal observed within the phantom no longer changed more than 1% of the previous measurement (Figure 17).

The influence of the injection rate on the mixing process is shown in Figure 17, with two notable observations: firstly, the faster injection rates result in the mixing process ending more quickly.

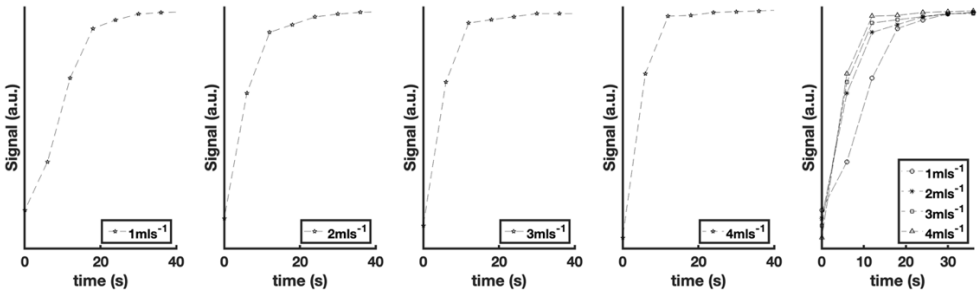

Figure 17 - Increase in signal within the entire dynamic phantom volume, after the injection of contrast agent at different rates. The final plot (far right) shows the change in signal for all injection rates on one diagram, allowing for comparison.

The PIU at 60s after the start of injection was calculated for each experiment at each injection rate, with the mean and standard deviation for each noted (Table 2).

Figure 16 demonstrates the increase in signal within the phantom as a result of the injection of the gadoteridol contrast, further region of interest analysis was performed to understand the effects of the variable injection rate on replicating bolus arrival time (Figure 17) *in vivo* and PIU (Table 2).

ROI	% Image uniformity (PIU) at different injection rates (ml/s)			
	1	2	3	4
	Mean ± St. Dev.	Mean ± St. Dev.	Mean ± St. Dev.	Mean ± St. Dev.
Gadoteridol	94 ± 2	96 ± 1	94 ± 3	95 ± 2
Water	96 ± 2	96 ± 1	96 ± 2	96 ± 3
Phantom	64.33 ± 4.04	73.67 ± 2.08	79.33 ± 2.52	84.33 ± 2.16

Table 2 - Percentage image uniformity across the entire dynamic phantom, at 60s after the injection of contrast agent. The PIU for different injection rates are also shown.

Table 2 shows a significant increase in PIU, within the dynamic phantom, when increasing injection rate. As expected the PIU values within the Gadoteridol and water reference standards showed high PIU values. There was also no significant change in PIU within the standards with increasing injection rate.

^{13}C-MR Spectroscopy

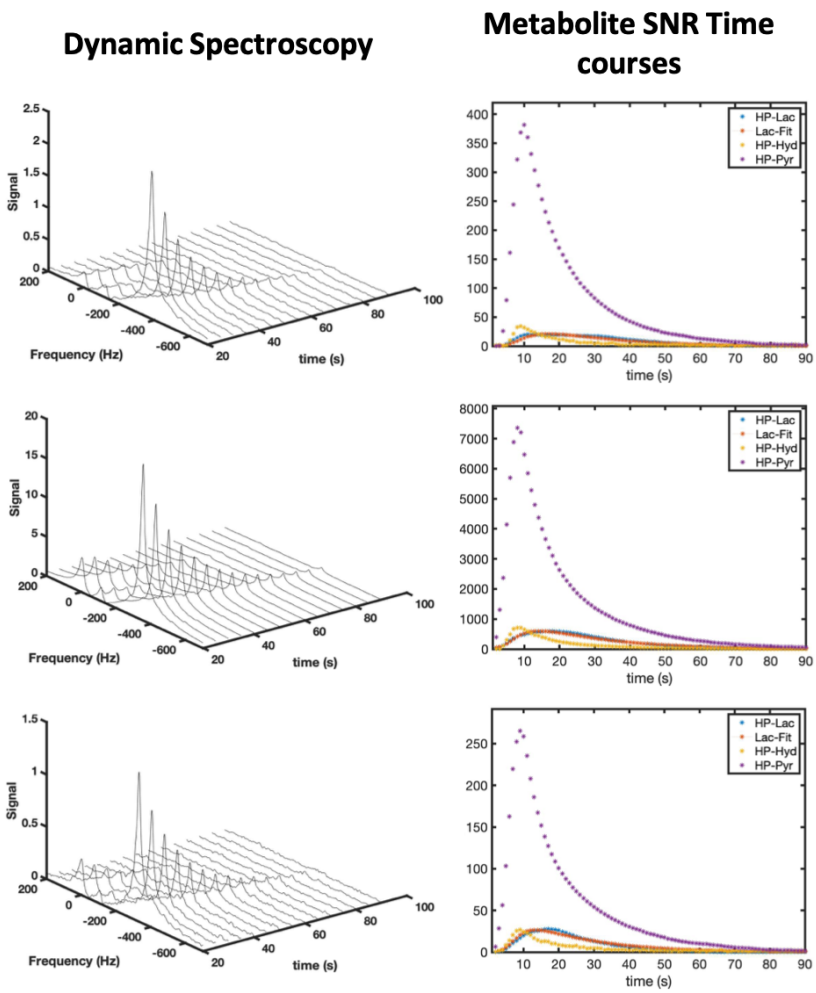

Figure 18 - Waterfall plots, showing every fifth spectra obtained and the corresponding SNR time courses (at full temporal resolution) are shown for all experiments involving the use of LDH enzyme (top row - 1.6µg/ml, middle row 3.2 1.6µg/ml and bottom row 4.8 1.6µg/ml). The change in SNR for lactate (blue), pyruvate hydrate (yellow) and pyruvate (purple) are shown in the time courses (right hand side column). An output of the kinetic model used to derive k_P in this study is a lactate fit time course (red), this is also shown in the time courses.

Spectra were compiled in the form of a waterfall plot (Figure 18), with the corresponding SNR time course also shown for each example. Generally, the lactate SNR is seen to proportionally increase, in relation to the pyruvate time course, with increasing enzyme concentration. By quantifying the signal time courses the LP_{AUC} and k_P can be calculated.

LP_{AUC} and k_P were seen to increase proportionally with increasing enzyme concentration. Across both metrics the maximum coefficient of variation was 13.22% with the average at 9.15% (Table 3).

Enzyme Conc. (µg/ml)	LP_{AUC}	Mean	Coeff. Var.	k_P (s^{-1})	Mean	Coef. Var.
1.6	0.10	0.098	13.22	0.0098	0.0099	9.09
	0.10			0.0109		
	0.19			0.0092		
3.2	0.09	0.0155	3.85	0.0152	0.0155	7.10
	0.07			0.0168		
	0.09			0.0146		
4.8	0.12	0.0252	10.55	0.0222	0.0252	11.11
	0.10			0.0257		
	0.14			0.0277		

Table 3 -The mean lactate to pyruvate area under the temporal curve (LP_{AUC}) and kinetic rate constant (k_P) for the measurements at each enzyme concentration were calculated. The coefficient of variation of each metric for each set of enzyme concentrations was also calculated

^{13}C-MR Imaging

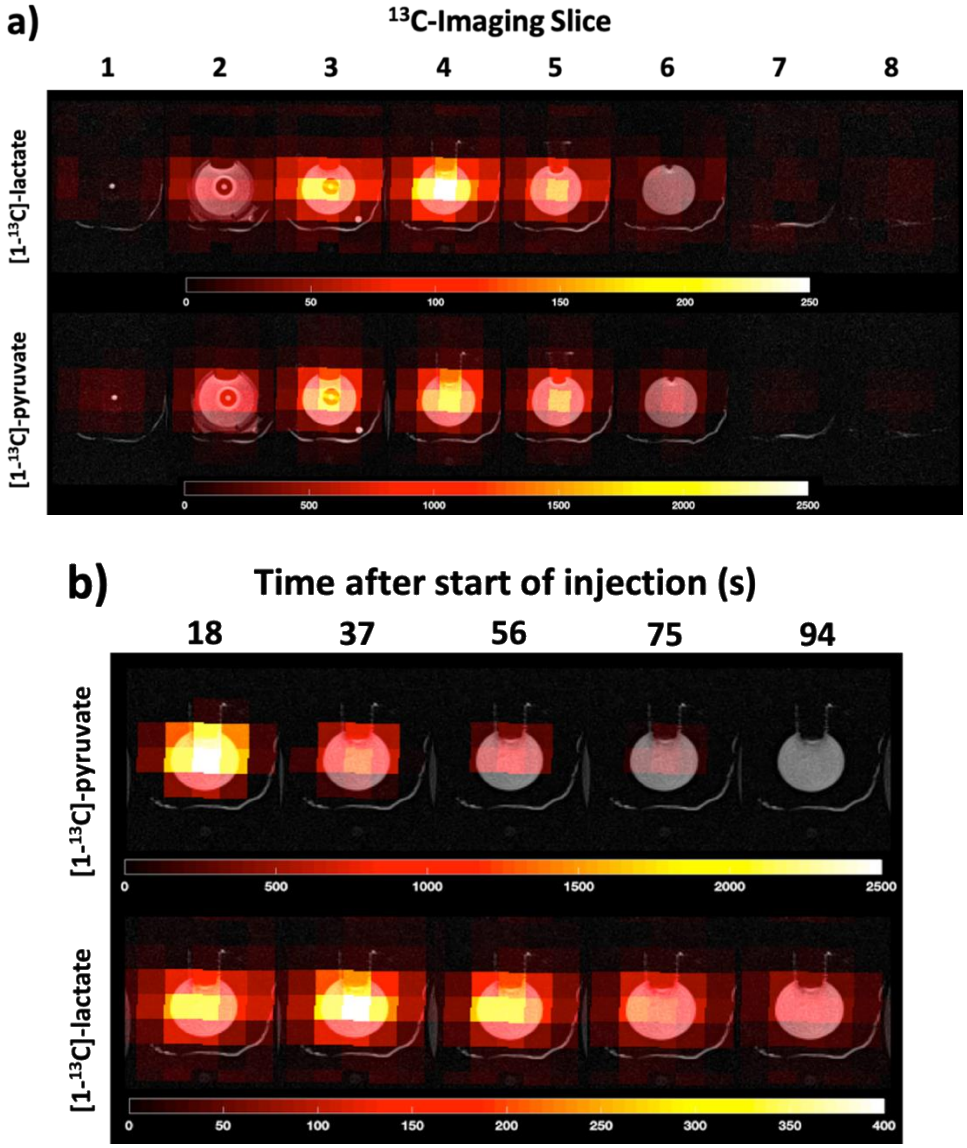

Figure 19 - Distribution of [1-^{13}C] pyruvate and [1-^{13}C] lactate within the dynamic phantom, at t = 12s are shown (a). The change in [1-^{13}C] pyruvate and [1-^{13}C] lactate signals at the centre of the phantom are shown up to 94s after the start of injection (b). The metabolite maps were overlaid on a set of T_2-weighted reference images.

The ME-bSSFP metabolite maps (Figure 19) localise both signals, [1-^{13}C] lactate and [1-^{13}C] pyruvate, within the dynamic phantom. The [1-^{13}C] lactate signals showed a slow build-up and decay curve (Figure 20), while the [1-^{13}C] pyruvate signal showed fast arrival in the chamber followed by decay.

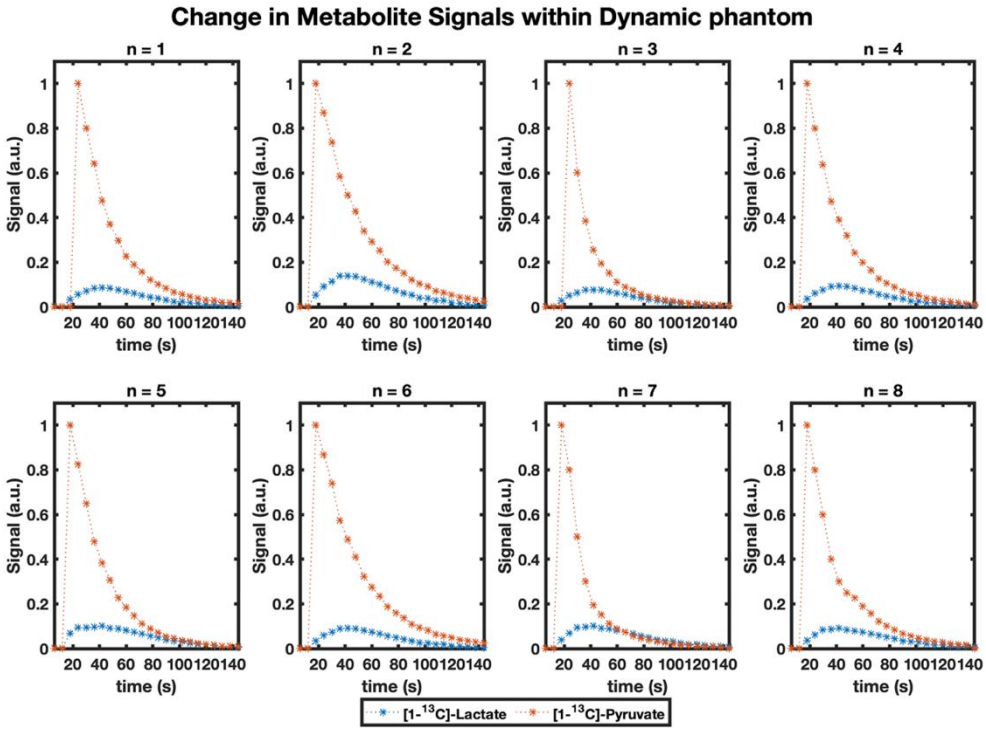

Figure 20 - The change in [1-^{13}C] lactate (blue) and [1-^{13}C] pyruvate (red) signals within the dynamic phantom up to 2m30s after the start of injection of 4ml hyperpolarised [1-^{13}C] pyruvate. Time curves are shown for all eight runs in the reproducibility study. These time curves were used to produce the analyses below.

Quantification of these images was performed by plotting the change in individual metabolite signals for the voxels covering the entire phantom. Analysis of the time curves for each measurement (Table 3) was performed by calculating LP_{AUC} ratios and k_P.

	Experiment									
Metric	1	2	3	4	5	6	7	8	**Mean**	**Coef. Var.**
LP_{AUC}	0.18	0.20	0.22	0.19	0.22	0.15	0.21	0.20	0.19	10.97
k_P	0.034	0.046	0.051	0.040	0.044	0.031	0.040	0.041	0.041	15.45

Table 4 -Graphical and kinetic analysis was performed on the metabolite time curves from all experiments in this study, the lactate to pyruvate area under the curve (AUC) ratio and kinetic rate constants (k_P) were calculated

Discussion

This work has presented a reproducible dynamic phantom system for use in hyperpolarised ^{13}C-MR studies, integrating remote and automated injection, allowing for the entire reaction to be recorded in real time.

Previous hyperpolariser studies, in prostate, have found the arrival of the pyruvate bolus to be between 20-30s [1]. For the purposes of identifying an optimal metric by which to analyse our data, we need to be able to replicate these time courses in as similar a manner as possible. As such a range of injection rates were tested. The point of maximum signal within the phantom, post injection, was defined as analogous to the moment of hyperpolarised [1-^{13}C] pyruvate bolus arrival. Whilst an injection rate of 1mls^{-1} took up to 30s to reach the maximum signal. There were little discrepancies from 2mls^{-1} and faster injection rates (Figure 17), however, there was a clear increase in the PIU with increasing injection rate (Table 2).

The increase in PIU at higher injection rates could be attributed to the subsequently higher pressures being used, forcing more interaction between the contrast and water within the phantom.

One limitation of this study is evident in Figure 17 at t = 36s, the contrast appears to settle at the bottom of the phantom. The contrast did in fact mix well with the water within the phantom, as demonstrated by the PIU values. Due to differences in density, however, between the water-contrast mix (approx. 1.140gml^{-1}) and the remaining water in the phantom that the contrast did not mix with, we observe two layers. This could be overcome in future studies through the use of two liquids with similar densities, but different T_1 and T_2 relaxations.

Another issue was that the PIU method is sensitive to the SNR of an image, with S_{min} and S_{max} diverging significantly at lower SNRs, affording reduced PIU values [76].

Controls put in place to mitigate these potential issues included: the use of an automated injection system to limit experimental variability, as well as the use of identical acquisition parameters and positioning during phantom setup.

The dynamic phantom demonstrates the capacity to observe the conversion of [1-^{13}C] pyruvate, through LDH, into [1-^{13}C] lactate, through both ^{13}C-spectroscopy (Figure 18) and ^{13}C-imaging (Figure 19), in a reaction analogous to that observed in clinical hyperpolarised ^{13}C-MR studies [1], [2]. The phantom has allowed us to capture the entire enzymatic reaction time course, with remote injection eliminating the need to remove the device from the MR scanner, as seen in previous studies [47]. The phantom's large size and use of a pressure outlet also eliminated the need to mix the relevant enzyme and hyperpolarised contrast prior to injection in the phantom [54].

Three factors can contribute to the rate of decline in [1-^{13}C] pyruvate signal: relaxation of the hyperpolarised state, deterioration of the signal via radiofrequency pulse excitation, and lastly, enzymatic conversion via LDH into [1-^{13}C] lactate. The evolution of the [1-^{13}C] lactate signal reflects its active enzymatic production from [1-^{13}C] pyruvate, which then, similarly to [1-^{13}C] pyruvate, undergoes an active signal decay due to both relaxation and pulse excitation.

The metabolite signal time courses extracted from both the non-localised spectroscopy and imaging studies offer a real time visualisation of the chemical conversion of [1-^{13}C] pyruvate to [1-^{13}C] lactate when compared to previous dynamic phantoms [47], as the current system allows for the entire process of [1-^{13}C] lactate signal generation being captured. Previous designs required mixing of the hyperpolarised agent and enzyme solution outside of the phantom, prior to injection, causing a portion of the reaction to be missed. Notably, the coefficient of variation in the imaging study (n = 8) for the metabolite signals at each time point was calculated as <16% and <11% for the AUC ratio and k_P, respectively (Table 3), demonstrating

the reproducibility of the experiments using the dynamic phantom. Similarly, the non-localised spectroscopy study showed lower average coefficient of variations for LP_{AUC} (9.2%) and k_P (9.1%) (Table 3).

The analysis of the metabolite signal time courses demonstrates how such a phantom can be used to investigate a variety of metrics of interest and showed the robust and reproducible nature of the dynamic phantom. The AUC method, which has been shown, under certain conditions, to provide a model-free surrogate of k_p [48], [50], which itself showed the lowest coefficient of variance across all analytical methods, possibly due to its insensitivity to pyruvate uptake [47]. The dynamic phantom, in the ^{13}C-imaging study also presents a lower coefficient of variation (11.6%) for the lactate to pyruvate AUC ratio than a previously described system (19.0%) that utilised manual injection [53]. This demonstrates the improvements that can be made through a system capable of facilitating automated injection. In clinical hyperpolarised ^{13}C-MR automated injection of the hyperpolarised agent is a standardised practice to reduce variability. This phantom takes our hyperpolarised ^{13}C-MR experiments one step closer to the clinical reality.

Enzymatic reactions are temperature sensitive, to mitigate the impact of temperature on the experiments the LDH and NADH were allowed to equilibrate to room temperature prior to preparing the phantom solution. There is also variation in the polarisation of the pyruvate upon dissolution (between 25.0 – 37.0°C) [36]. This alongside the difficulty in measuring the temperature of the phantom solution post-injection is a limitation of the system. Despite this, the metrics extracted across the experiments undertaken in this body of work and the coefficients of variance calculated suggest that the system has a good experimental reproducibility.

Prior to both clinical and preclinical hyperpolarised ^{13}C-MR studies, MR scanners most often need to be calibrated and adjusted for quality assurance purposes [44]. This study utilised an endorectal coil with an

in-built [^{13}C] urea phantom. It is uncommon, unfortunately, to find other multinuclear coil types with similarly in-built phantoms for reference. This could be solved in the current design by adding a static chamber, filled with carbon-13 labelled compound, within or on top of the current dynamic phantom system, allowing for calibration and adjustment without the need for an external phantom.

Another factor to consider involves the amount of hyperpolarised [1-^{13}C] pyruvate used in comparison to how much is needed for a single experiment. Typically, for clinical experiments, 40ml of hyperpolarised [1-^{13}C] pyruvate are produced per fluid path, with each taking >4h to produce. Adjusting the formulation used to prepare hyperpolarisation fluid paths is possible. However, a more practical development might be integrating multiple chambers into the current design for simultaneous experiments with different concentrations of enzymes. Such dynamic phantoms with multiple chambers have been described previously [44], [78] but did not have the capacity for automated injection.

Summary

The system demonstrably reduced the variance of kinetic analysis outcomes by incorporating an automated injection system for the hyperpolarised agent. The capacity for integrating any automated injection system found in a scanner room and the means to vary enzyme concentration within the phantom indicate that this setup has the opportunity to mimic a range of metabolic reactions, at varying rates, potentially reflecting different tissue types. This system could also be used as part of more extensive studies, identifying the best metric by which to quantify dynamic, hyperpolarised, ^{13}C metabolic imaging data; or supporting the development and optimisation of new ^{13}C-MR sequences for possible future clinical routine.

Chapter 6: ME-bSSFP sequence optimisation

For the following results chapter, an existing 3D ME-bSSFP sequence and simulator which describes its behaviour were presented to the author of this thesis, who was tasked with translating this sequence for use in clinical hyperpolarised 13C-MR work focused on metabolic prostate imaging. The author of this thesis undertook phantom work to understand the sensitivity profile of an endorectal coil, using this information, as well as discussions with experienced radiologists to identify an appropriate field of view for the sequence and resolution. Using this information the author modified the existing simulator, to allow for multiple input parameters, allowing for a broad range of spectral parameters to be simulated faster than the original model. The results from this modelling were validated using phantoms built by the author. The author also modifications made to an existing IDEAL model, assessing the efficacy of using an a priori field map as an additional input into the model to resolve echo data.

Aims

The following aims were outlined as essential to optimising and clinically translating Multi-echo balanced Steady-State Free Precession (ME-bSSFP).

- Produce an ME-bSSFP sequence that can provide full coverage of even the largest prostates during hyperpolarised ^{13}C-MR studies.
- Optimise the spectral parameters for an ME-bSSFP sequence to maximise metabolite signals observed during hyperpolarised ^{13}C-MR studies.

Background

Clinical hyperpolarised ^{13}C-MR presents an opportunity to interrogate metabolism *in vivo* in real time. Presently, there is a focus on the conversion of pyruvate into lactate, as some theorise that cancer aggressiveness can be correlated with lactate production [79]. This has been especially demonstrated in subjects with prostate cancer [1], [79]. One significant limitation of hyperpolarised ^{13}C-MR studies is the short-lived nature of the hyperpolarised state. An acquisition method with a high spectral and spatiotemporal resolution is needed to maximise the hyperpolarised signals.

Several pulse sequences have been demonstrated as feasible means by which to quantify metabolism during hyperpolarised ^{13}C-MR studies [80], [81]. Non-localized spectroscopy provides high spectral and superb temporal resolution (often <1s), but it yields only a single spectrum from a region that is defined by the sensitivity profile of the MR excitation and receiver coils [1]. Chemical shift imaging (CSI) enables signals to be spatially resolved but has a relatively poor temporal resolution [2], [37]. Echo-planar spectroscopic imaging (EPSI) sequences afford improved temporal resolution but have limited spectral bandwidth, and they are particularly prone to errors caused by susceptibility gradients at air/tissue interfaces, such as those which occur with prostate imaging procedures [62]. Instead of broad- or multiband excitation and sophisticated spectral-spatial signal encoding, a metabolite-specific excitation combined with a fast signal readout has also been shown to be a robust approach [82].

Another possible approach employs the Dixon technique, invented for fat-water separation in ^{1}H-MRI [40], [41]. This approach involves the acquisition of echo images at different echo times (TEs), and it allows for the reconstruction of metabolite-specific chemical shift maps, with the spectral resolution being limited by the number of acquired echo images and reconstruction parameters [42]. If only a few downstream hyperpolarised metabolites are expected, and there is *a priori*

knowledge of the chemical shifts, this technique allows immense reduction of spectral bandwidth and thus reduction of scan time [83].

The balanced steady-state free precession (bSSFP) sequence is widely used in anatomical MRI as it affords high spatiotemporal resolution and signal-to-noise ratio (SNR); many vendors are offering a rendition of the sequence (e.g., TrueFISP (true fast imaging with steady-state precession – Siemens), FIESTA (fast imaging employing steady-state acquisition – GE), and Balanced-FFE (balanced fast-field echo – Philips)). This sequence, adapted with a bipolar multi-echo (ME) balanced gradient readout and Dixon type post-processing, could provide an optimal balance of spectral sampling, spatial resolution, and overall acquisition time in hyperpolarised ^{13}C-MR studies [41], [43], [44]. Previous preclinical studies demonstrated this sequence in both phantom and animal subjects, successfully analysing the conversion of hyperpolarized [1-^{13}C] pyruvate into [1-^{13}C] lactate [44], [45].

A 3D variant of a previously described ME-bSSFP sequence (Figure 12) was used in this study with a slab-selective, sinc-shaped excitation pulse of flip angle (FA) α/2, followed by refocusing pulses of FA α with alternating polarity (±) [44]. Between 5 and 10 dummy cycles at the beginning of the pulse sequence were used to create a transient transverse magnetization [46]. A Cartesian centre-out k-space readout trajectory was employed with ($N_p \times N_s$) phase and slice encoding steps, and a bipolar multi-gradient-echo readout centred between refocusing pulses to acquire N_e consecutive echoes separated by a fixed difference in TE (ΔTE). An α/2 flip-back pulse, played out at the end of the sequence, transferred remaining transversal magnetization (M_T) back into longitudinal magnetization after the end of each scan [41], [44].

The magnitude of a magnetisation vector (M), representative of species with and without off-resonance spins, can be described in three planes, M_x, M_y and M_z. M_z is typically considered to be parallel to the reference magnetic field B_0, whilst M_x and M_y are considered, in

combination, as perpendicular to the field . The evolution of the magnetisation vector can be represented by the following equations , which are a combination of the result of resolving Equation 10 and 11 with respect to time, with decay constants T_1 and T_2 (Equation 13):

$$\begin{bmatrix} M_{xy}(t) \\ M_z(t) \end{bmatrix} = \begin{bmatrix} e^{-i\omega t}e^{-t/T2} & 0 \\ 0 & e^{-t/T1} \end{bmatrix} \cdot \begin{bmatrix} M_{xy}(0) \\ M_z(0) \end{bmatrix} + \begin{bmatrix} 0 \\ (1 - e^{-t/T1}) \end{bmatrix} \cdot M_z^{eq} \quad (13)$$

The excitation (R), via a radiofrequency (RF) pulse, of the species represented by the vector M(0) can be described, in matrix form, as a rotation applied on M(0), as a function of flip angle and phase:

$$R_{\alpha,\psi} = \begin{bmatrix} \cos(\alpha)\sin(\psi)^2 + \cos(\psi)^2 & (cos(\alpha) - 1)\cos(\psi)\sin(\psi) & \sin(\alpha)\sin(\psi) \\ (\cos(\alpha) - 1)\cos(\psi)\sin(\psi) & \cos(\alpha)\cos(\psi)^2 + \sin(\psi)^2 & \sin(\alpha)\cos(\psi) \\ -\sin(\alpha)\sin(\alpha) & -\sin(\alpha)\cos(\psi) & \cos(\alpha) \end{bmatrix}$$

A bSSFP sequence can be described by applying R to M (Equation 15) in the following order:

$$R_{\frac{\alpha}{2},0} \xrightarrow{\frac{TR}{2}} R_{\alpha,\pi} \xrightarrow{TR} R_{\alpha,0} \xrightarrow{TR} \ldots \xrightarrow{TR} R_{\alpha,0} \xrightarrow{TR} R_{\alpha,\pi} \xrightarrow{\frac{TR}{2}} R_{\frac{\alpha}{2},0} \quad (15)$$

TR refers to the repetition time, otherwise referred to as the time between RF pulses. The signal intensity of the excited species is equivalent to the magnitude of the transverse magnetisation component $M_{xy}(TE, \omega)$ at a discrete echo time TE. This simulator was based on a previous iteration used to optimise a preclinical ME-bSSFP sequence for use in hyperpolarised ^{13}C-MR studies [44]. The code listings for this simulator are available in Appendix C.

With steady-state techniques such as ME-bSSFP, the signal amplitude varies periodically due to phase advances [84]. This signal variation can cause a failure of the sequence's refocusing mechanism

and can result in banding artefacts [84]. The artefacts can be mitigated by using a short repetition time (TR). Among other reasons, [1-^{13}C] pyruvate is an interesting molecule for hyperpolarisation due to its rather long T_1 and T_2 relaxation constants, reported as 15-30 s and 0.9 s, respectively [41], [44]. For such spin systems with $T_1 >> T_2$, the use of small FA lowers the pulse sequence-induced consumption of the hyperpolarized magnetization by keeping the major fraction of the excited magnetization in longitudinal orientation where the dominant decay rate is T_1 [46]. At the same time, FA must be high enough to achieve sufficient measurable transverse magnetization for good SNR. However, the use of high FA (>30°) and short TRs may be prohibited by the MRI system, to limit specific absorption rate (SAR) of energy in patients. All of these concerns suggested the need for careful selection of TR and FA to preserve signal lifetime, avoid high SAR, and afford a high SNR [42], [84], [85]. The aforementioned simulator can be used to identify an optimal combination of spectral parameters to avoid banding artefacts and maximise signal.

This study aimed to investigate the optimisation and application of a three-dimensional (3D) ME-bSSFP sequence for metabolic, whole-organ prostate imaging in hyperpolarised ^{13}C-MR studies. Optimal spectral parameters were identified by modelling the bSSFP signal as described above.

Methods

All *in silico* simulations were developed and run using custom MATLAB 2022b scripts (Mathworks, Natick, USA). The empirical phantom studies throughout this chapter were performed on a 3T Siemens Biograph mMR, with an endorectal coil and clamshell transmitter used as described in Chapter 5. The chemicals used to create phantoms were sourced from Merck (Merck Group, Munich, Germany).

Testing endorectal coil sensitivity limit

To determine an optimal field of view and voxel resolution for the ME-bSSFP acquisition volume the size of the prostates of individuals with PCa had to be considered. A recent study found that men with a larger prostate volume (>72cc) had a greater risk of biopsy confirmed PCa than those with a smaller prostate volume (<38cc) [86]. To cover even the largest prostates (beyond the size of that reported in a recent review [86]), the field of view was set to 90 x 90 x 80 mm.

To determine the lateral, in-plane coverage of the coil a large ethylene glycol (2M, 1L) phantom (Figure 21) was scanned via an ME-bSSFP sequence: (FOV): 180 x 180 x 80 mm^3, voxel size: 7.5 x 7.5 x 10 mm^3, FA: 30°, TR: 21 ms, number of echoes (NE): 13, number of signal averages (NA): 1. The change detected in the phantom's signal to noise ratio was then plotted as a function of distance, from the urea reference phantom within the endorectal coil to the edge of the field of view. The distance at which SNR fell below 1 was deemed to be the upper limit of the coil's sensitivity profile.

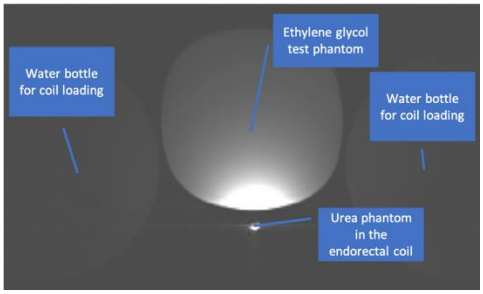

Figure 21 - Experimental set up used to map the sensitivity profile of the endorectal coil, this involved placing a large (1L) ethylene glycol phantom on top of the endorectal coil, with water placed adjacent to this set up for coil loading.

Identifying an optimal resolution for ME-bSSFP acquisitions

To identify an optimal resolution an acetate (3M, 100ml) phantom (Figure 23) was placed on top of the endorectal coil and scanned using the following ME-bSSFP parameters (Table 5).

Mat. Size	Resolution (cm x cm x cm)	TR (ms)	NoE	BW per Pixel (Hz)	FA (°)	ΔTE (ms)	NSA	Acq. time (s)
8*8	11.3*11.3*10	19.5	9	1200		1.02	38	
10*10	9*9*10	19.5	9	1201		1.06	30	
12*12	7.5*7.5*10	19.5	9	1201	30	1.10	25	~6
14*14	6.4*6.4*10	19.5	9	1236		1.11	21	
16*16	5.6*5.6*10	22.5	11	1202		1.18	16	

Table 5 - ME-bSSFP parameters used to identify a suitable spatial resolution. Included are references to the repetition time (TR), the No. of echoes (NoE) used, bandwidth per pixel (BW per Pixel), the flip angle (FA), the difference in echo times (ΔTE), and the number of signal averages (NSA

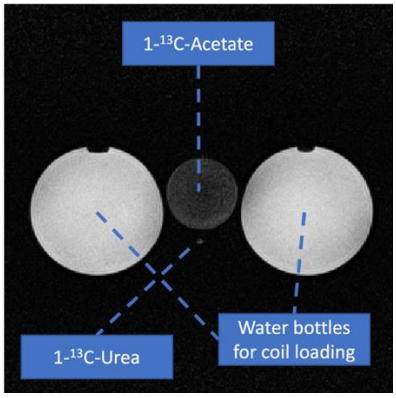

Figure 22 - Experimental set up used to determine an optimal resolution for the ME-bSSFP sequence

The change in SNR across the phantom as a function of the distance from the endorectal coil was calculated and plotted for each resolution.

Modelling endorectal coil sensitivity profile

PCa imaging in hyperpolarised ^{13}C-MR studies necessitates the use of endorectal coils, which are known to have an inhomogeneous profile, wherein its sensitivity drops the further one moves from the coil, as a function of the Biot-Savart law (Equation 16).

$$B = \frac{Isin\phi dz}{4\pi R^2} \qquad (16)$$

Wherein B(r) is the magnetic field value at a given point (r), R is the distance from said point to a piece of wire (dz – representative of the coil element), $sin\phi$ = r/R and I is a small element of current. By modelling this profile correction, it can potentially be applied to images acquired using coils with an inhomogeneous profile, thereby amplifying areas of low signal and providing a qualitative improvement in image quality [87]. Equation 16 was modelled by first identifying the position of the element within the endorectal coil, assumed to be in a similar position to the urea phantom within it. A mask was then created matching the FOV and resolution of the scan to which the modelled profile is eventually applied. Relative to the position of the coil element, equation 16 is applied to each voxel in the mask, affording the modelled coil profile similar to that seen in Figure 30c.

The modelled profile was then applied to a T_2-weighted axial turbo spin echo sequence: FOV: 180x140x90 mm^3, Voxel size: 0.7×0.7×3 mm^3, slice thickness: 3 mm, no. of slices: 30, TR: 5400 ms, TE: 109 ms, ETL: 15, NSA: 1, FA: 90; was acquired during a clinical scan with the endorectal coil and compared to a T_2-weighted axial image acquired with a body coil. A comparison of the distribution of the signal intensities within the peripheral zone was made via a Kolmogorov-Smirnov test, between the two coil types, before and after profile correction of the endorectal coil image.

Spectral optimisation

A previously described numerical simulator was used to calculate theoretical bSSFP signals for various TRs: 8-22 ms and FA: 5-35° [44]. This was done to find optimal imaging parameters for on-resonant lactate (Δf = 0) and off-resonant pyruvate (Δf = -385 Hz). Simulator parameters: number of pulses = 64, TE_{center} = TR/2, T_1 = 13.1 s, T_2 = 0.6 s. These simulations were empirically validated using a [1-^{13}C] lactate phantom and the 3D ME-bSSFP sequence on the 3T MRI; field of view (FOV): 90 x 90 x 80 mm^3, voxel size: 11.3 x 11.3 x 10 mm^3, FA: 10-30°, TR: 8-22 ms, number of echoes (NE): 7, number of signal averages (NA): 6. A paired t-test was performed using the simulated and empirical data. To determine if there were any statistically significant differences between the simulator and the empirical data.

The simulator was subsequently used to calculate signal evolutions for a set of TR values and fixed FA hyperpolarized [1-^{13}C] pyruvate imaging: TR: 15.8/17.6/21.0 ms, FA: 24°, Δf: -700 - 100Hz, number of pulses = 64, TE_{center} = TR/2, T_1 = 13.1 s, T_2 = 0.6 s. These T_1 and T_2 values were chosen as they were measured for a lactate phantom produced for the empirical testing portion of this study. The T_1 and T_2 values measured for this phantom were 13.1 s and 0.6 s respectively. The volume of the cylindrical phantom was 2.3ml, with housing material machined from a polyetherimide stock. The phantom was also doped with sodium azide (0.23% w/v) and gadoteric acid (0.15% w/w).

When selecting an optimal TR/FA combination a brief analysis of the field inhomogeneities in a typical patient undergoing a hyperpolarised ^{13}C-MR study, using an endorectal coil, was performed. The size of the field inhomogeneities was considered relative to the size of pass bands generated by TR/FA combinations when selecting an optimal set of spectral parameters.

Avoiding signal aliasing

Signal aliasing can become an issue if a ΔTE is not correctly identified, this is due to the relationship between ΔTE and the sampling rate, Nyquist frequency (f_{Nyq}), given by equation 17[84], [85].

$$f_{Nyq} = \frac{1}{2\Delta TE} \qquad (17)$$

An inappropriate ΔTE will afford spectral wrap, making metabolites at specific frequencies indistinguishable (Figure 23) [85].

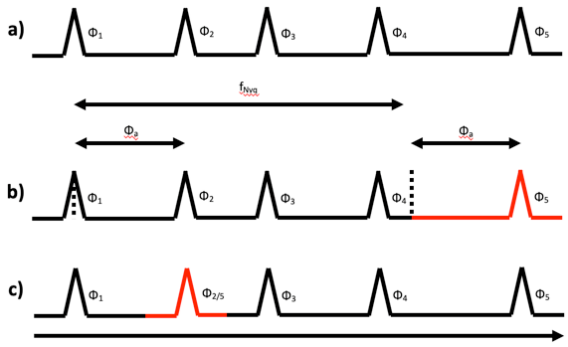

Figure 23 - a) a spin system containing five peaks; b) the selection of an inappropriate ΔTE is demonstrated, the Nyquist frequency (fNyq) shows how the offset between Φ1 and Φ2 (Φa) is equal to the offset between fNyq and Φ5; c) the aliasing effect is shown demonstrating how signals can become indistinguishable if an appropriate ΔTE is not selected.

To avoid the aforementioned signal aliasing f_{Nyq} was modelled as a function of ΔTE, via equation 17, with ΔTE bands shown where signal aliasing could occur; this simulation was used to identify an optimal ΔTE (Table 6).

		ΔTE (ms)		
Metabolite	**Δf (Hz)**	**Lactate**	**Hydrate**	**Alanine**

Lactate	-30:30	-	-	-
Hydrate	-100:130	-	-	-
Alanine	-195:215	-	-	-
Pyruvate	-360:-400	1.17-1.53	1.67-2.28	-
Urea	-610:-630	0.75-0.86	0.93-1.07	1.14-1.31

Table 6 – Pyruvate, it's downstream metabolite frequencies and the frequency ranges at which they appear. The f_{Nyq} and corresponding ΔTE (ms) at which aliasing can occur between metabolites is also shown, up to a maximum ΔTE of 2.5.

To visualise the effects of signal aliasing ME-bSSFP data was simulated via equation 18 and applied to a mask for visualisation purposes.

$$S(TE_n) = \left(met_1 + \sum_{m=1}^{M} met_m e^{j2\pi\Delta f_m TE_n} \right) . e^{j2\pi\varphi TE_n} \qquad (18)$$

Where $S(TE_n)$ is an echo image, n is the NoE, m is the total no. of metabolites, Δf_m the frequency offset for the respective metabolites, met_1 is the signal intensity of the on-resonance frequency, met_m is the signal intensities of the off-resonance frequencies and φ the field inhomogeneity.

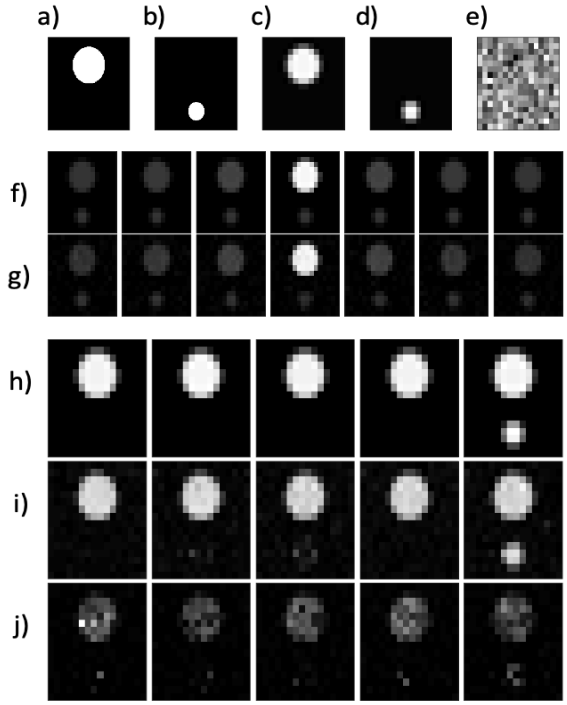

Figure 24 - Simulated data demonstrating how the IDEAL model separated echo data in the spectral domain. Two masks were generated (a-b), a gaussian filter was applied to these and

they were downsampled to match a matrix size seen in HYP-MR data (c-d). Echo data (n = 7, ΔTE = 1.1ms) was then generated using an a priori field map (e), in the positions shown, for five metabolites: met 1: Δf = 0Hz, signal intensity = 1 a.u., met 2: Δf = -120Hz, signal intensity = 1 a., met 3: Δf = -200Hz, signal intensity = 1 a., met 4: Δf = -385Hz, signal intensity = 1 a., met 5: Δf = -620Hz, signal intensity = 1 a. (f – left to right). To the subsequent echo data (g), gaussian noise was applied (h) such that the SNR of the bottom phantom was 10 a.u.. The echo data was then separated via the IDEAL model with (i) and without (j) the use of the field map.

Two masks were generated, downsampled to the bSSFP resolution and combined. ME-bSSFP echo data was created via equation 18 and applied to each voxel in the combined mask for a specific number of metabolites, frequencies and intensities. The difference in echo times (ΔTE), between the echo times (TE_n), used to generate this echo data, was varied to identify parameter values that would avoid signal swaps upon the echo data being resolved, in turn producing metabolite maps (Figure 24).

Large phantom			**Small phantom**		
met	**Δf**	**SI**	**met**	**Δf**	**SI**
1	0	1	**1**	-	-
2	-120	1	**2**	-	-
3	-200	1	**3**	-	-
4	-385	1	**4**	-	-
5	-620	1	**5**	620	1

Table 7 – Parameters used to create the echo data for the simulations. The no. of echoes was set at 7, field offset ψ at -100Hz, and the ΔTE varied from 0.50ms to 1.15ms

All empirical ME-bSSFP echo data acquired in this study were resolved using an IDEAL model, further details of which can be found in Appendix B.

Results

Testing endorectal coil sensitivity limit

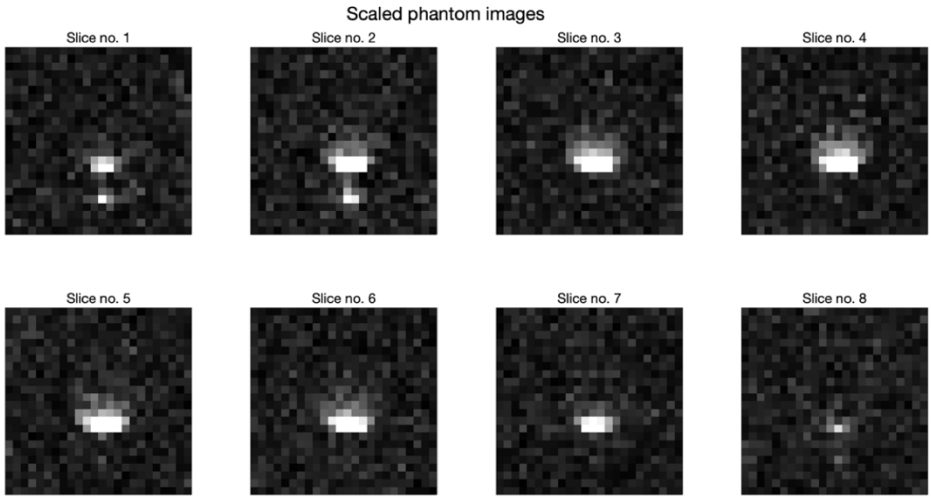

Figure 25 - signal recorded in the ethylene glycol phantom as part of an attempt to understand the sensitivity profile of the endorectal coil

Images of the ethylene glycol phantom clearly demonstrate the endorectal coil's inhomogeneous profile (Figure 25). Upon analysing the evolution of the phantom's signal graphically it can be seen that at the coil's most sensitive portion (slices 3 and 4) suggest that an SNR of above one can be observed until approximately 80mm from the endorectal coil. When the signal falls below this threshold no signal is observed, only noise (Figure 26).

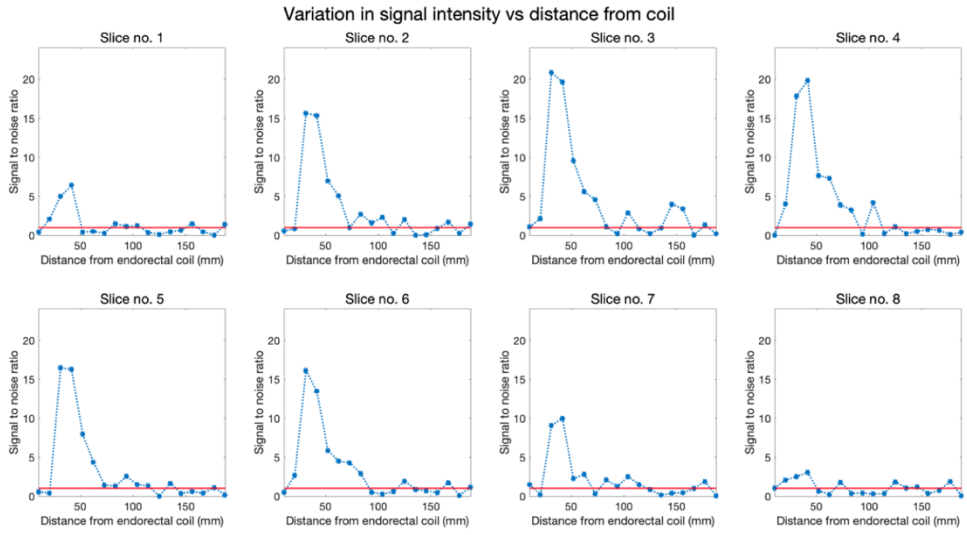

Figure 26 - Change in signal to noise ratio as a function from distance from the endorectal coil was plotted for each slice spanning the coil.

Identifying an optimal resolution for ME-bSSFP acquisitions

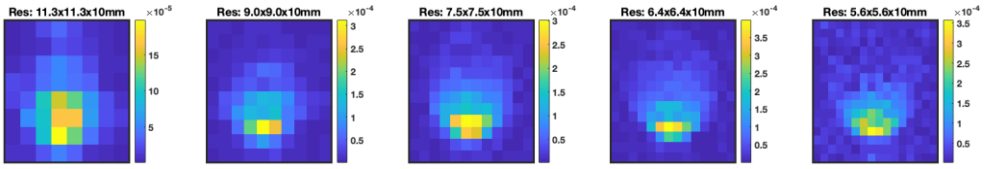

Figure 27 – metabolite maps produced from the acetate phantom scanned as part of identifying an optimal resolution. These scans were performed with an identical field of view (90 x 90 x80 mm) and demonstrate the change in visibility of the carbon-13 signal within the phantom as a function of increasing resolution (from left to right).

The ME-bSSFP scans with progressively higher resolution (Figure 27) demonstrate that whilst a smaller voxel size may improve the qualitative perception of the image, it does not, however, allow for the entire phantom to be imaged properly. This is especially seen as when using a resolution higher than 9x9x10mm the SNR in the voxels at the top of the phantom tend to 1, indicative of noise (Figure 28). As such, a resolution of 9x9x10mm could be used, however, as the SNR plots suggest that towards the periphery of the phantom is low (< 3), utilising the lower voxel volume of 11.3x11.3x10mm may be a better option.

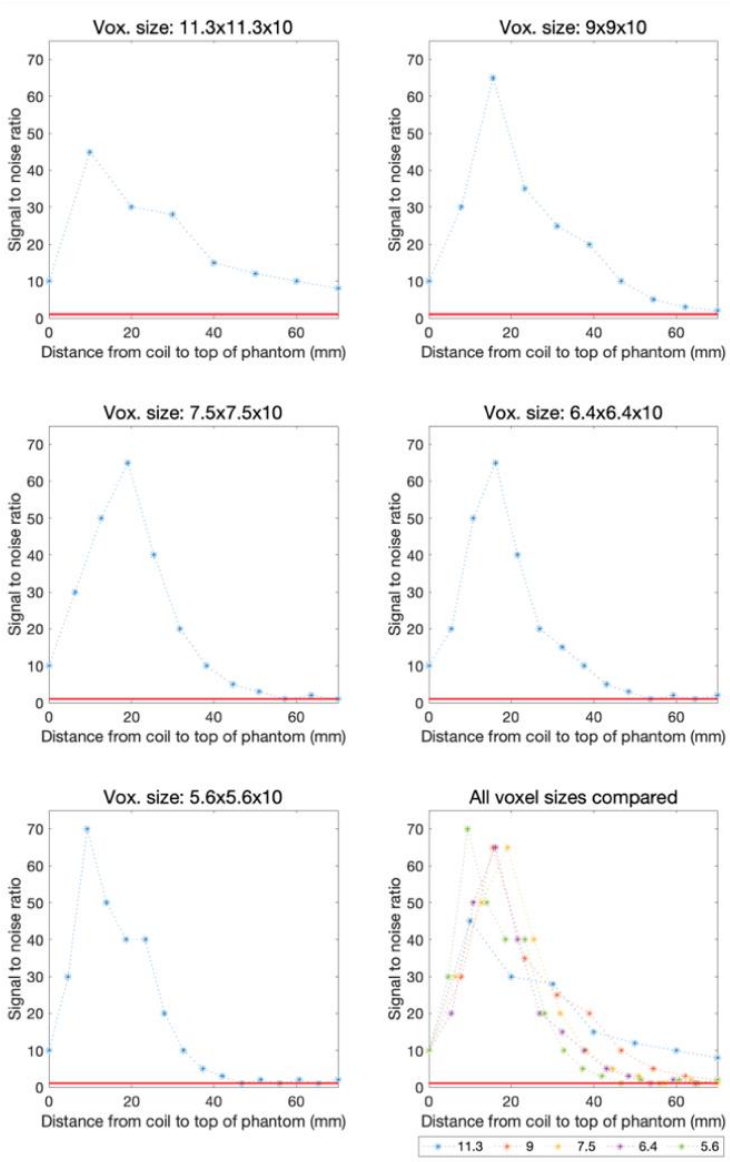

Figure 28 - change in acetate signal to noise ratio as a function of the distance of the voxels from the endorectal coil. Five graphs are shown, each from a scan with a different voxel size. The final graph (bottom left) shows all of the others overlaid.

Modelling and applying coil sensitivity profile

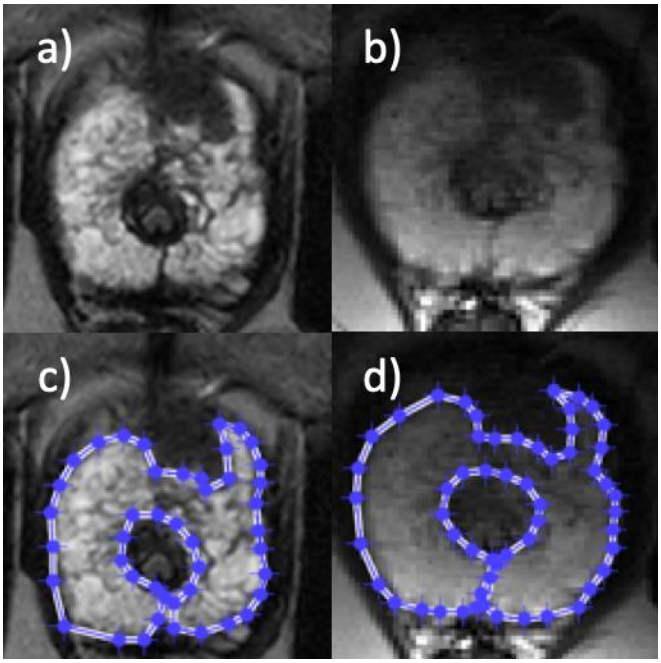

Figure 29 - a) T_2-weighted image acquired of a prostate using a body coil. b) T_2-weighted image of the same prostate acquired with an endorectal coil

The regions of interest drawn around the peripheral zone (Figure 29) for the subject used in this work is highlighted in blue. An effort was made to exclude the transition zone due to its highly inhomogeneous nature.

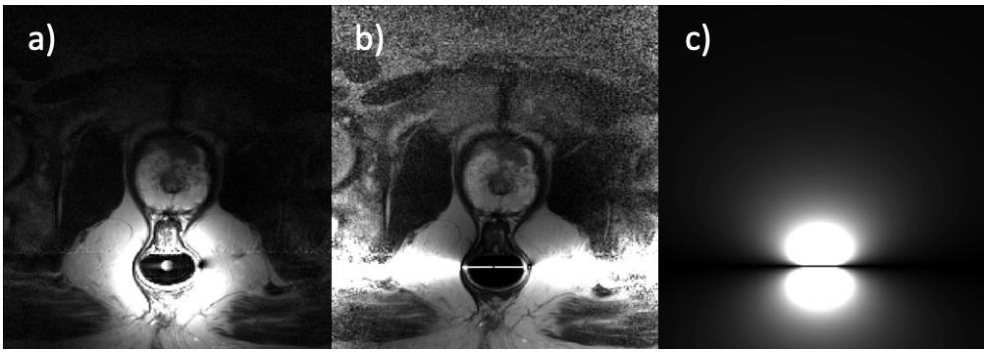

Figure 30 - a) T_2-weighted, full field of view, image of a prostate acquired with an endorectal coil. b) image shown in a corrected by the application of a mask generated to model the sensitivity profile of the coil (c) as per equation 16.

The mask generated by modelling equation 16 was applied to the image acquired with the endorectal coil (Figure 30). Doing so provides detail toward the upper portion of the image, allowing for an improved qualitative view. Flaring of the signal intensities in the voxels

perpendicular to the coil, in the corrected map is expected due to the profile of the mask generated.

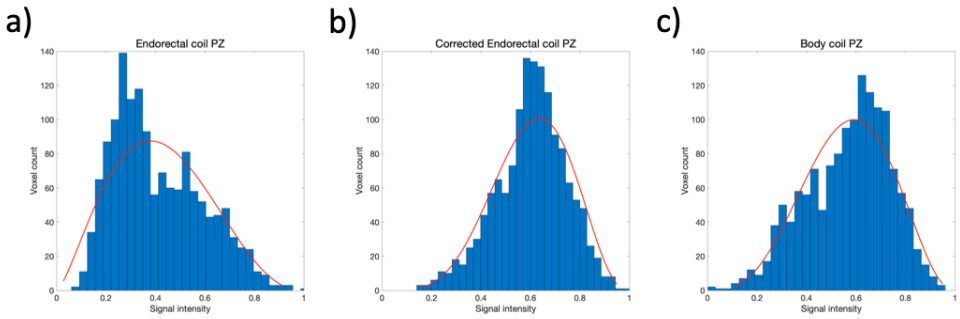

Figure 31 - distribution of signal intensities of the voxels within the subject's peripheral zone are shown. a) shows the histogram of the uncorrected PZ, b) shows a histogram of the PZ upon being corrected by a mask generated to model the sensitivity profile of the coil. c) shows a histogram for the PZ of the subject's T_2-weighted scan obtained by a body coil.

Analysing the signal distributions (Figure 31) before and after the correction to the endorectal coil images suggests that after applying the mask the corrected image's peripheral zone signal intensities bear a closer resemblance to those taken with the body coil, than prior to the correction being performed.

The empirical distribution functions were calculated and plotted for the pairs of distributions to better quantify the impact of applying the mask.

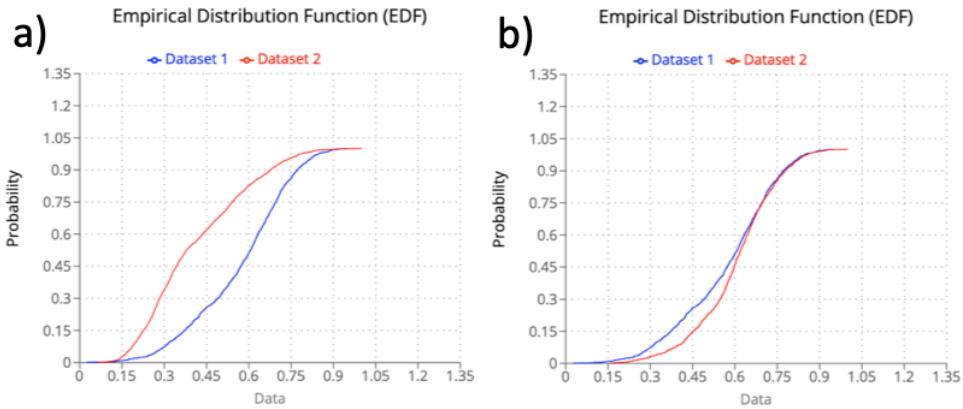

Figure 32 - The empirical distribution functions were plotted and compared between the body coil PZ (Dataset 1 in both instances) and uncorrected endorectal coil PZ (dataset two in a) signal intensities (a), as well as between the body coil and the corrected endorectal coil PZ (dataset two in b) signal intensities (b). This figure was produced from Quest Graph™ Kolmogorov-Smirnov (K-S) Test Calculator." AAT Bioquest, Inc., https://www.aatbio.com/tools/kolmogorov-smirnov-k-s-test-calculator

The graphs shown demonstrate that the empirical distribution functions were closer between the body and endorectal coil images upon applying the mask. From this Kolmogorov-Smirnov D statistics and p values were calculated for each pair of distributions (Figure 32). A threefold reduction in the D value was observed upon applying the mask. Although it should be noted that in both instances a p value of < 0.05 was found suggesting that there was still a significant difference between the body and endorectal coil signal intensities, even after correction (Table 8).

Distribution pair	D	p
Body-Uncorrected endorectal	0.3824	<0.05
Body-Corrected endorectal	0.1152	<0.05

Table 8 – Results of comparing the pairs of distributions, before and after correction, with a Kolmogorov-Smirnov test

Spectral Optimisation

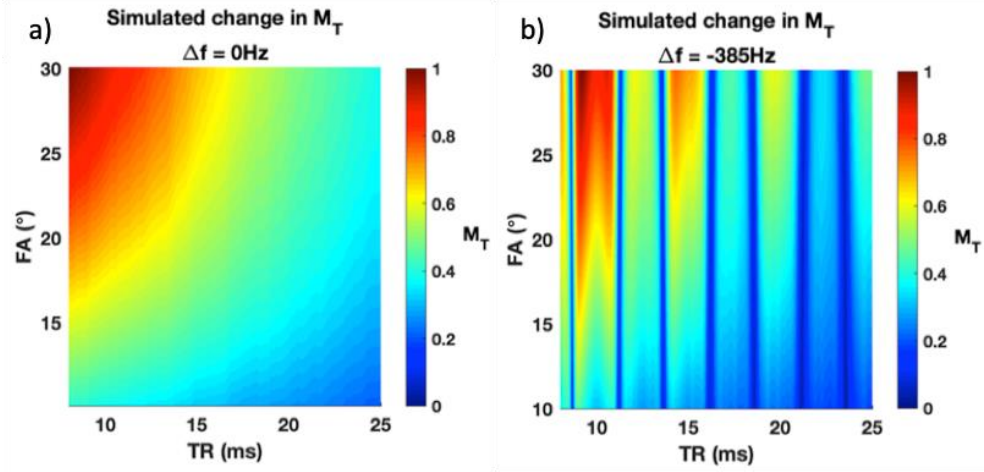

Figure 33 – The ME-bSSFP signal response was modelled for a range of TR (8-25ms) and FA (10-30°) values. These simulations were performed at 0Hz (a) and -385Hz (b). The transverse magnetisation (M_T) is representative of the signal response.

The correlation coefficients between normalised empirical and simulated data for FA and TR at Δf = 0Hz and Δf = 385Hz were all found to be greater than 0.96, affording values similar to a previous study (Figure 33 and 34) [44]. Further analysis using paired t-tests found no statistically significant differences between the mean values of the normalised empirical and simulated data ($p > 0.05$), across all testing experiments, affirming the simulator's ability to appropriately reflect the ME-bSSFP sequence's empirical performance (Table 9).

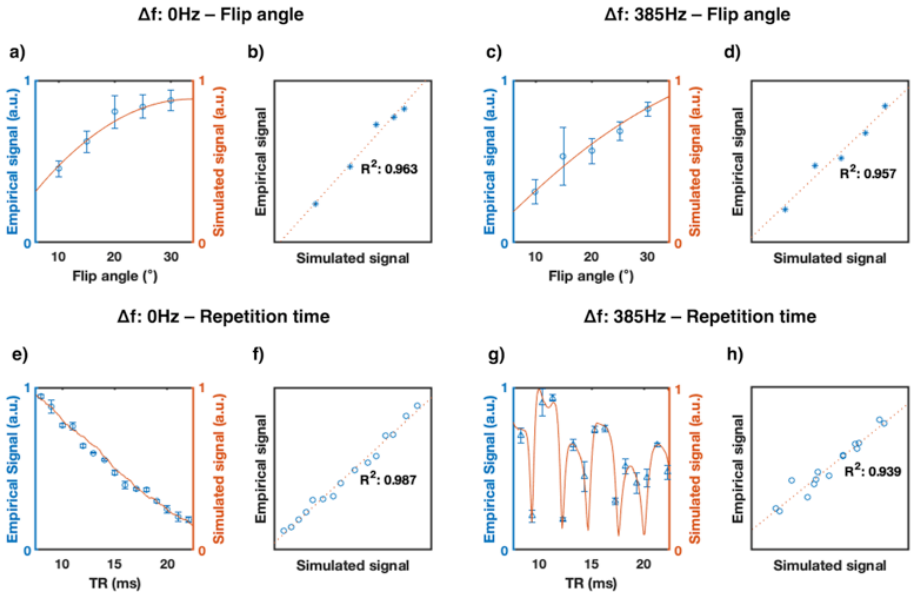

Figure 34 - Simulated and empirical experimental results for testing of the ME-bSSFP simulator: change in empirical and simulated signal as a function of flip angle at 0Hz (a) and 385Hz (c), at a constant repetition time (19.5ms); change in empirical and simulated signal as a function of repetition time at 0Hz (d) and 385Hz (g) at a constant flip angle (30°). Correlation

between resulting signal (Simulated and Empirical) as a function of changes in flip angle between empirical and simulated signals at 0Hz (b) and 385Hz (d). Correlation between resulting signal (Simulated and Empirical) as a function of changes in repetition time between empirical and simulated signals at 0Hz (f) and 385Hz (h).

Δf: 0Hz		**N**	**Mean**	**St. Dev.**	**95% CI**		**R^2**	**Pearson**	**t-test p**
FA	Simulated	5	0.823	0.201	0.429	1.218	0.963	0.988	0.552
	Empirical	5	0.814	0.185	0.451	1.177			
TR	Simulated	12	0.805	0.111	0.587	1.023	0.987	0.994	0.279
	Empirical	12	0.751	0.151	0.454	1.048			

Δf: -385Hz		**N**	**Mean**	**St. Dev.**	**95% CI**		**R^2**	**Pearson**	**t-test p**
FA	Simulated	5	0.599	0.239	0.131	1.067	0.957	0.982	0.552
	Empirical	5	0.567	0.272	0.034	1.177			
TR	Simulated	12	0.716	0.172	0.378	1.054	0.939	0.969	0.279
	Empirical	12	0.595	0.254	0.097	1.092			

Table 9 - Correlation between empirical and simulated signals using ME-bSSFP at Δf = 0Hz (top) and Δf = -385Hz (bottom). N refers to the number of measurements taken, whilst the mean, standard deviation and 95% confidence intervals are also shown. The R^2 and Pearson correlation coefficient between the simulated experiments and their respective empirical studies are shown, whilst the p-values from paired t-tests are included.

FA optimisation

The maximum applicable flip angle was limited to 24° at the scanner due to SAR limitations, with the signal response at Δf = 0 Hz and -385 Hz subsequently modelled (Figure 35). Using this value, three

potential TRs: 15.8, 17.6 and 21.0 ms were identified. A lower R such as ~11ms or ~13ms could not be selected due to scanner limitations.

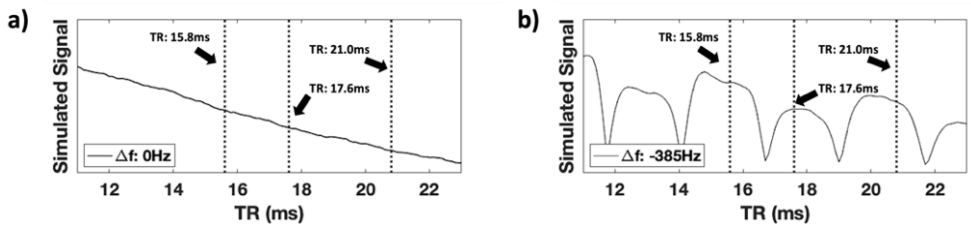

Figure 35 – Change in simulated signal (transverse magnetisation – M_T) as a function of TR for a fixed flip angle (24°) at Δf=0 (a) and Δf=-385 (b). On these graphs a) and b) the repetition times: 15.8,17.6 and 21.0ms are shown by dotted black lines.

TR optimisation

Further modelling demonstrated that the expected lactate frequency (0 Hz) consistently appeared in the middle of areas of high signal (pass bands), whilst the respective pyruvate frequency (-385 Hz) was not in the middle of a pass band (stop band) for TR = 17.6 ms; as such this TR was excluded (Figure 36). Despite both 15.8 and 21.0 ms being deemed suitable for use, 15.8 ms was chosen for further use due to the improved overall temporal resolution (~6 s) it provided compared to 21 ms (~8 s).

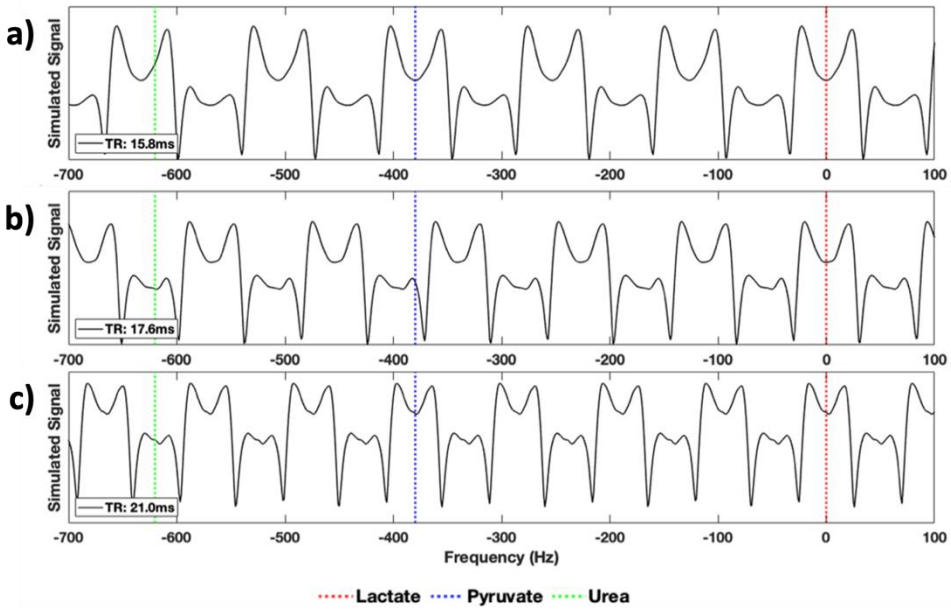

Figure 36 - Change in simulated signal (transverse magnetisation – MT) as a function of frequency for a fixed flip angle (24°) at different repetition times: 15.8 (a),17.6 (b) and 21.0ms (c). In each instance the expected resonance frequency of lactate (Δf = 0, red), pyruvate (Δf = -385, blue) and urea (Δf = -620, green) are shown by dotted lines to indicate whether metabolites appear in pass or stop bands

Field map analysis

With prostate imaging involving the use of an endorectal coil, large inhomogeneities arise when air becomes trapped in the rectum, which may result in spectral shifts, potentially causing metabolites to appear in stop bands. As such wide and flat pass bands are preferred, when selecting a suitable TR. Dual gradient echo acquisitions were obtained for each subject after the completion of the me-bSSFP scans, from which field maps were calculated. This was done to better understand whether field inhomogeneity would influence signal amplitude from the selected ME-bSSFP parameters. The phase difference between each set of images was divided by the difference in echo time to afford a field map (equation 19):

$$\psi = \frac{\Delta\theta}{\Delta TE} \qquad (19)$$

Where ψ is the B_0 inhomogeneity in Hz and Δθ is the difference in the phase images from the two echoes (Figure 37):

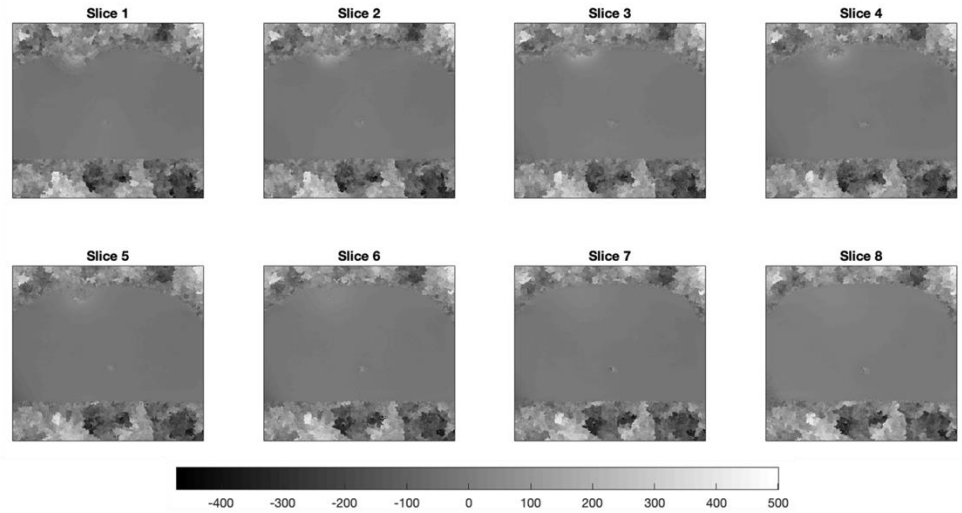

Figure 37 - field map slices generated via the processing of a dual gradient echo sequence, via equation 19, for Subject 1.

By segmenting the abdomen, the field inhomogeneities can be better visualised (Figure 38):

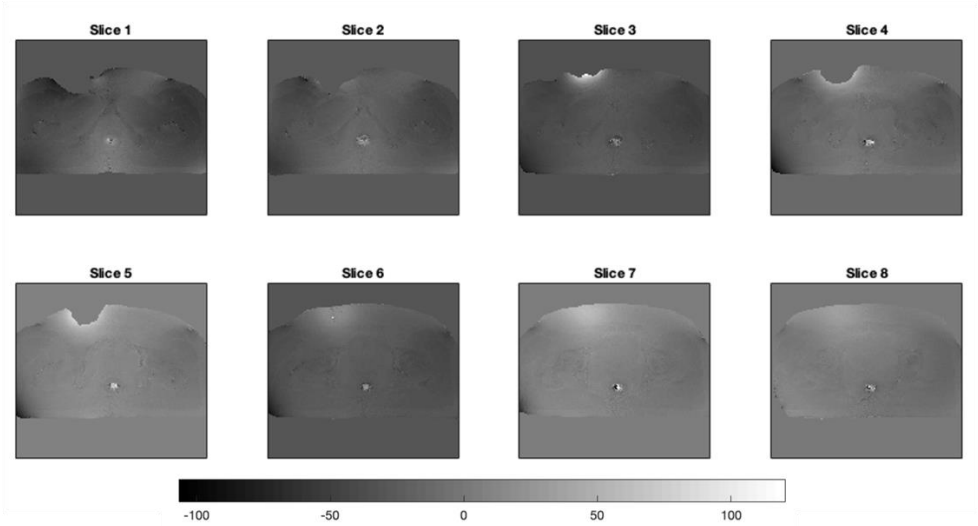

Figure 38 – Segmented abdominal field maps produced via drawing a region of interest around the data seen in the previous figure. This allows for a localised understanding of field inhomogeneity

Quantitative analysis of these field maps show a high signal in the rectum, which can be attributed to the presence of air. The variation across the entire abdomen, excluding the rectum is ±22Hz. The inhomogeneity in the endorectal coil itself, varies between -167 to 240Hz, across all patients recruited for this study and is in a range likely to be noise. Further analysis of the field maps showed that in the prostate there was a field inhomogeneity of 0.47±0.55 Hz (mean ± 95% CI), across the entire cohort (Figure 39).

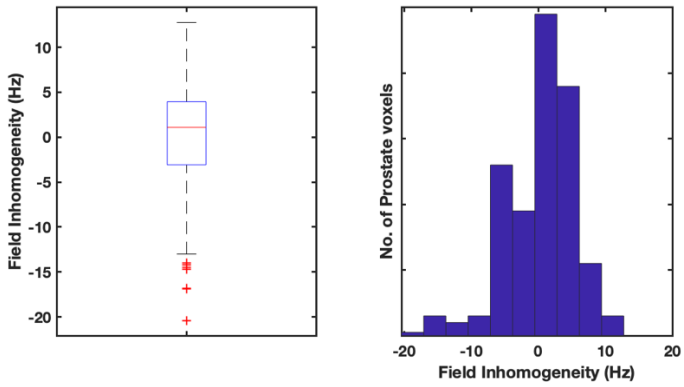

Figure 39 - Variation in field inhomogeneity in the prostate, across all patients, shown in the form of a boxplot (left) and a histogram (right)

Field map analysis, alongside the earlier signal modelling was used to select an optimal TR. Despite a TR of 21.0ms showing both lactate and pyruvate appearing in the middle of pass bands a TR of 15.8ms was chosen due to the wider nature of the pass bands considering the potential effects of field inhomogeneity across the abdomen, excluding

the rectum. The higher estimated M_T in said bands was also an influencing factor, whilst the shorter TR would contribute to a preferred, faster temporal resolution. Urea was not considered further when selecting TR and FA as it is not of metabolic interest, appearing only in a phantom within the endorectal coil, used for FA calibration, scanner frequency centring and physical positioning purposes.

Avoiding signal aliasing

An inappropriately selected ΔTE can impact the IDEAL model's ability to resolve me-bSSFP data. This is due to the Nyquist frequency (sampling rate) and its relation to ΔTE (equation 17). Specific ΔTEs can afford spectral wrap, making pairs of metabolites at specific frequencies, for a given ΔTE, indistinguishable (Figure 40).

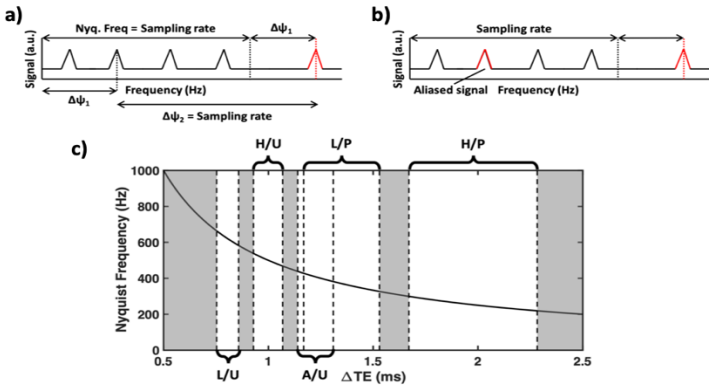

Figure 40 - a) a spin system containing five species is shown. In this case the ΔTE results in a Nyquist frequency falling in between the final two species. If the Nyquist frequency is found to be equal to the offset between the second and last species ($\Delta\psi_2$) an aliasing effect is observed (b).

Using the echo data simulator described (equation 18), datasets were produced, with varying ΔTE to visualise the issues highlighted regarding Nyquist frequency (Figure 41).

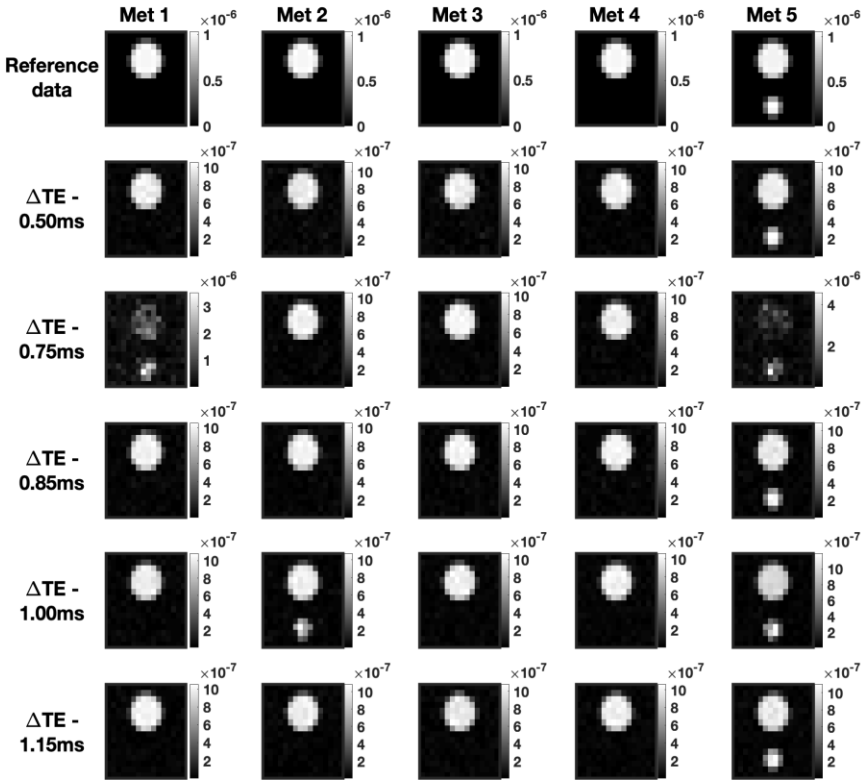

Figure 41 - A single slice of bSSFP data was generated as described in Figure 24 with metabolites; met 1: Δf = 0Hz, Signal intensity = 1 a.u.; met 2: Δf = -120Hz, Signal intensity = 1 a.u.; met 3: Δf = -200Hz, Signal intensity = 1 a.u.; met 4: Δf = -390Hz, Signal intensity = 1 a.u.; met 5: Δf = -620Hz, Signal intensity = 1 a.u.; in the large phantom and met 5: Δf = -620Hz, Signal intensity = 1 a.u. in the smaller phantom (shown in the top row – reference data). The ΔTE in each instance was varied for a constant no. of echoes (n = 7) and a priori field maps used to separate the echo data. This was done to illustrate the signal aliasing effect described earlier.

Discussion

The use of the ME-bSSFP MRI pulse sequence for hyperpolarised ^{13}C-MR has previously been reported in preclinical studies [32], [41], [51]. Translation of the technique from preclinical to clinical scanners, however, necessitated optimisation. This work successfully demonstrated the validation of a numerical simulator which models ME-BSSFP behaviour, whilst then proceeding to use said simulator to identify optimal spectral parameters for use in human studies. We also showed the modelling of the coil sensitivity profile for an endorectal coil, the process of selecting a spatial resolution, as well as steps to limit image artefacts. Parameter optimisation was performed considering optimal conditions for PCa imaging in hyperpolarised ^{13}C-MR studies.

Compared with external coils, an endorectal coil offers the advantage of higher sensitivity, which is critical for studies such as these that are very demanding of SNR. However, their sensitivity profile is spatially dependent; it is highest in the vicinity of the coil and drops off with distance. This work found a suitable resolution by which to potentially image anterior tumours.

A 9 x 9 x 8 cm^3 FOV was chosen due to the size of the largest possible prostate, but also because of the sensitivity profile of the coil. ^{13}C-imaging found the coils sensitivity for a 6 second scan to be no greater than 7cm from the endorectal coil. A 9 x 9 cm in plane FOV was determined to be suitable to avoid wrap artefacts from the top of the prostate. The decision to image eight slices was made so as to ensure the entirety of the rectum could also be captured, again to avoid potential signal wrap.

Considering the relationship of voxel size and SNR, the profile of the coil and the short-lived nature of the hyperpolarised state a decision was made to select voxel dimensions of 1.13 x 1.13 x 1 cm^3 with a field of view of 9 × 9 × 8 cm^3. Whilst the resolution seemed large

compared ^{1}H-imaging, other hyperpolarised ^{13}C-MR studies have demonstrated sequences with similar resolutions and as such to maintain diagnostic quality imaging, ensure full prostate coverage, and achieve adequate temporal resolution, the larger voxel sizes were chosen[50], [79]. A higher spatial resolution would be beneficial; however, it should be noted that this would compromise temporal resolution and require a greater number of excitations and phase encoding steps, both of which are likely to negatively impact the longitudinal hyperpolarised signal [88].

This work also briefly explored the possibility of modelling the endorectal coil sensitivity and using this to improve image quality. Whilst the distribution of signal intensities upon correction was promising there was still a significant difference when compared to a body coil. This measure also amplifies noise at the periphery of images and as such can make areas containing noise inadvertently seem as though they contain signal.

An optimal TR/FA combination were derived using an *in-silico* model, which was validated using empirical data [41], [44]. The Pearson correlation coefficients between empirical and simulated signals were in a similar range to a previous study using the same *in-silico* model [44]. While a high FA was found to afford an increased signal, consideration had to be given to limiting FA to protect the non-renewable hyperpolarised longitudinal magnetisation. SAR concerns were also considered. Lower FA (< 30°) and the use of a limited number of dynamic acquisitions within a specified time were required to keep SAR within the acceptable range. This was balanced against having too low a FA as this would have resulted in decreased SNR. The selected spatial resolution afforded a limited number of excitations for imaging, in turn allowing for the maintenance of an acceptable longitudinal hyperpolarised signal to allow for repeated temporal acquisitions. With these constraints, a limited range of acceptable TRs were identified as indicated by the *in-silico* model *i.e.* 15.8 ms, 17.6 ms and 21 ms. A TR of 17.6 ms, despite being in a pass-band, was not

chosen as it would have compromised the refocusing mechanism, which ME-bSSFP relies upon to produce a strong signal at the central echo (TR/2) [88]. Whilst both 15.8 ms and 21.0 ms were suitable, the former was chosen to achieve a better temporal resolution. The total acquisition time for imaging the full prostate, including six-fold averaging, was 6s.

The importance of selecting an appropriate time interval between echoes in a multi-echo sequence was observed. This will be particularly important as during clinical hyperpolarised ^{13}C-MR studies we aim to maximise our lactate signal by setting it as our centre frequency. In doing so, as we expect both pyruvate hydrate (which is in a pH dependent equilibrium with pyruvate) and urea (from the phantom within the endorectal coil) signals there is a significant chance of signal aliasing. Whilst these may not be metabolites that we will aim to quantify directly there is still a desire to minimise spectral artefacts in an aim to improve image quality.

Summary

This body of work successfully demonstrated the optimisation of an existing ME-bSSFP sequence for potential use in the clinical metabolic imaging of PCa by identifying a combination of suitable spatiotemporal and spectral parameters.

Section C

The following section presents original research across two chapters demonstrating the application of ME-bSSFP, for the purposes of quantifying tumour metabolism, in hyperpolarised ^{13}C-MR studies.

Chapter 7 presents a cohort of 5 patients with biopsy confirmed tumours who underwent hyperpolarised ^{13}C-MR scans. Comparisons were made between healthy and tumorous regions to assess the suitability of using ME-bSSFP for PCa imaging in hyperpolarised ^{13}C-MR studies.

Chapter 8 describes a case study wherein a subject with a large pheochromocytoma was recruited as part of a hyperpolarised ^{13}C-MR study. Comparisons between different tissue types (cystic, solid, and necrotic) were made.

Chapter 7: Application of optimised ME-bSSFP in clinical prostate cancer subjects with HP-MR

In this chapter the parameters identified by the author in chapter 6 were used to produce a 3D ME-bSSFP sequence, which was then tested in subjects with histologically confirmed prostate cancer. The author manned the MR control room, whilst a research technician dealt with the preparation of a clinical fluid path and subsequent handling of the hyperpolarised agent. A clinical team composed of two clinicians and a nurse were involved in recruiting and handling the patient on the day of the scan. The author performed all data processing and data analyses.

Aim

Demonstrate the optimised ME-bSSFP sequence's ability to quantify tumour metabolism, in a clinical environment, using hyperpolarised ^{13}C-MR

Background

There are several pulse sequences being used in conjunction with hyperpolarised ^{13}C-MR to quantify prostate metabolism [1], [79]. Multi-Echo balanced steady state free precession has been previously demonstrated in preclinical hyperpolarised ^{13}C-MR experiments and has shown great promise due to its high spatiotemporal resolution, suggesting that it may be suitable for whole organ coverage in metabolic imaging of the prostate.

Methods

All data processing was performed using MATLAB (MathWorks, Natick, MA, USA). Carbon-13 labelled materials were obtained from Merck (Kenilworth, NJ, USA). All patient work was performed using a custom-designed ^{13}C clamshell transmit and dual tune $^{1}H/^{13}C$ receive-only endorectal coil (dimensions: 97x31x22mm) housing a 1 ml, 8M ^{13}C-urea phantom for power calibration (Rapid Biomedical GmbH, Rimpar, Germany), on a 3T Siemens Biograph mMR (Siemens Healthineers, Erlangen, Germany). Multi-parametric MRI (mpMRI), including Diffusion Weighted Imaging (DWI) and Dynamic Contrast-Enhanced Imaging (DCE) were performed on a 3T Philips Ingenia (Philips, Amsterdam, Netherlands).

Cohort description

Five subjects with PCa were recruited based on biopsy results and multiparametric MRI (mpMRI). All subjects were found to possess Gleason grade 3+4 tumours and underwent a hyperpolarised ^{13}C-MR study. Written informed consent to participate in a pelvic hyperpolarised ^{13}C-MR study was obtained from each subject. This study was conducted as part of the Hyperpolarised ^{13}C-Pyruvate Study (ID: NCT03687645).

Preparation of hyperpolarised [1-^{13}C] pyruvate

[1-^{13}C] pyruvic acid was mixed with AH111501 electron paramagnetic agent and loaded into a fluid path under aseptic conditions [2]. The fluid path was irradiated with microwaves at <1 K for approximately 2 h in a clinical hyperpolariser (SPINLab, GE Healthcare, Chicago, Il), resulting in a polarisation level of 19.9-35.6 %. The frozen sample was then dissolved with sterile heated water (38ml) and neutralised with 17.5 g sterile trometamol buffer (333 mM Tris and 600 mM NaOH); >40 ml of hyperpolarised [1-^{13}C] pyruvate solution was produced at concentration: 251-270 mM, temperature: 35.6-39°C and pH: 6.7-7.6. Injection of the hyperpolarised agent started 70-81 s after dissolution,

with data acquisition beginning immediately after the completion of injection.

^{1}H imaging

In brief, our protocol used high resolution T_2-weighted ^{1}H images, for tumour localisation and a B_0 map for IDEAL processing of the carbon-13 echo images. Prior to injection of hyperpolarised [1-^{13}C] pyruvate, anatomical axial and sagittal T_2-weighted (^{1}H-T_2W) images were acquired with a turbo spin-echo (TSE) sequence for tumour localisation; FOV: 180x140x90 mm^3, voxel size: 0.7×0.7×3 mm^3, TR: 5400 ms, TE: 109 ms, slice thickness: 3 mm, no. of slices: 30, echo train length (ETL): 15, NSA: 1, FA: 90°. Additionally, a dual gradient echo sequence was obtained for each patient; FOV: 360×360×80 mm^3, voxel size: 1.4×1.4×10 mm^3 FA: 15°, TR: 329 ms, TE_1: 2.39 ms, TE_2: 7.17 ms, Echo Train Length (ETL): 2, No. of Signal Averages (NSA): 3. This sequence was used to calculate a field map required during the processing of the ME-bSSFP metabolite signals.

^{13}C imaging

The same ME-bSSFP sequence: FOV: 90×90×80 mm^3, voxel size: 11.3×11.3×10 mm^3, FA: 24°, TR: 15.8 ms, ΔTE: 1.1 ms, NE: 7, NSA: 6; was used for all five subjects. The transmit frequency was centred on the lactate resonance frequency (Δf = 0Hz) by positioning it +620 Hz from the peak resonance of the urea phantom within the endorectal coil. A wide readout bandwidth of BW_{read} = 1200 Hz/px was utilised, to reduce alternating chemical shift displacements of the off-resonant metabolites in the bipolar readout. For each patient, four consecutive ME-bSSFP acquisitions were obtained directly after completion of the injection. This was followed by the acquisition of a non-localised spectrum using a single free induction decay (FID): FA: 10°, TR: 1000 ms, NSA: 1, the main purpose of which was to identify frequencies for metabolite map reconstruction via an IDEAL model (See Appendix B). This was followed by a further 15 ME-bSSFP

acquisitions, an additional non-localised spectrum and another 15 ME-bSSFP acquisitions.

Data analysis

The echo images obtained during ^{13}C-MR imaging were passed through an IDEAL model [44], using the calculated field map as an initial guess, with metabolite maps reconstructed at the frequencies identified in the non-localised spectra. For the clinical dataset, quantification involved extracting the change in metabolite SNR as a function of time for voxels (regions of interest – ROIs), including the histologically confirmed tumour site and healthy tissue within the same anatomical zone. Lactate-to-pyruvate area under the temporal curve (LP_{AUC}) ratios were calculated [47], [55]; a one directional kinetic model was also used to derive the forward rate constant (k_P) for the enzymatic conversion of pyruvate to lactate.

Results

Nonlocalised ^{13}C-spectroscopy

Nonlocalised spectroscopy was performed for each patient around 25s after the completion of injection to detect the appropriate frequencies for metabolite map reconstruction (Figure 42).

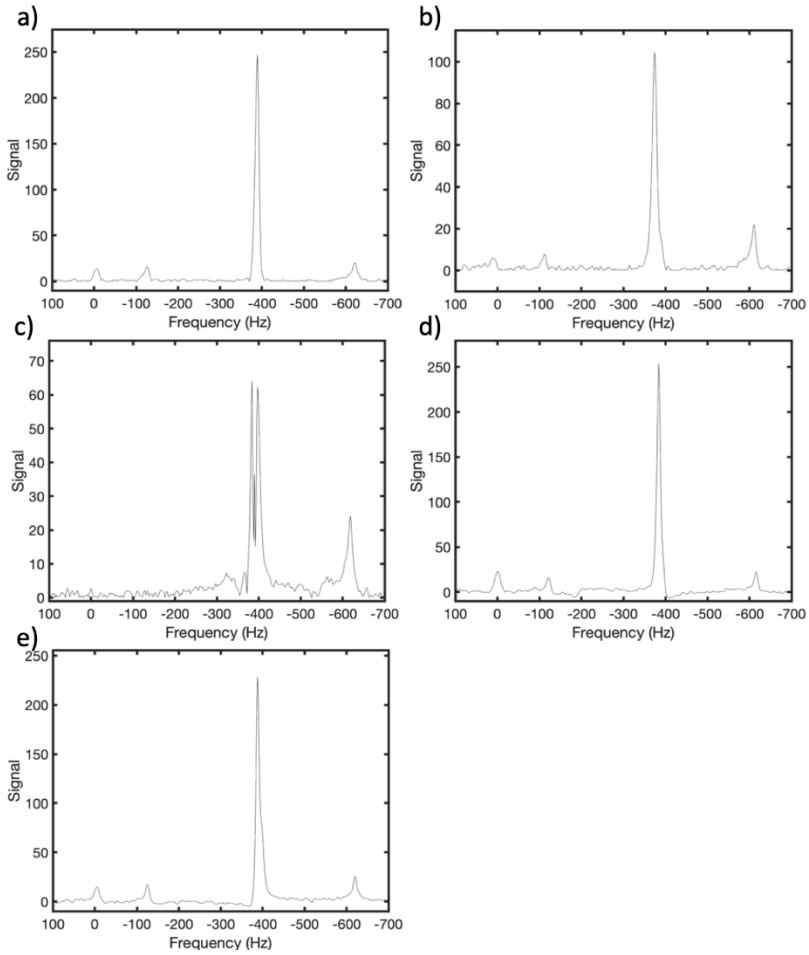

Figure 42 - Non-localised spectra obtained 25s after the completion of injection of hyperpolarised [1-^{13}C] pyruvate. Peaks are observable at ~0Hz, -120Hz, ~-400Hz and ~-620Hz, representative of lactate, pyruvate hydrate, pyruvate and urea respectively.

Pyruvate (~ -400Hz) and pyruvate hydrate (~ -120Hz) was observed in all subjects. A urea (~ -620Hz) peak was also evident in the spectra for each patient, this was from a phantom within the endorectal coil, used for positioning and power calibration. Lactate (~ 0Hz) was observed in the spectra of four out of the five patients included in this study.

Subject 1

Subject 1 possessed biopsy confirmed Gleason 3+4 tumours in the transitions zone (Figure 43).

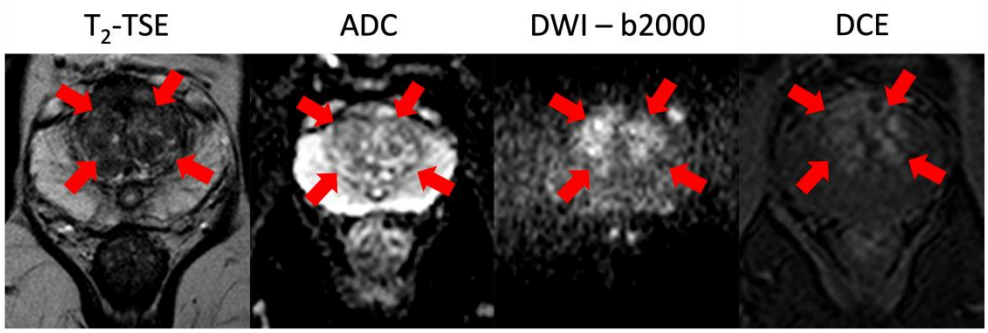

Figure 43 – (From left to right), T_2-weighted turbo spin echo, Apparent Diffusion Coefficient, Diffusion weighted Imaging and Dynamic Contrast Enhanced scans were obtained for subject 1, prior to the hyperpolarised ^{13}C-MR study. The tumour position is highlighted with red arrows.

The tumour spanned across several slices which is also highlighted via red arrows on the T_2-weighted axial scans acquired moments before the subject underwent injection of hyperpolarised [1-^{13}C] pyruvate.

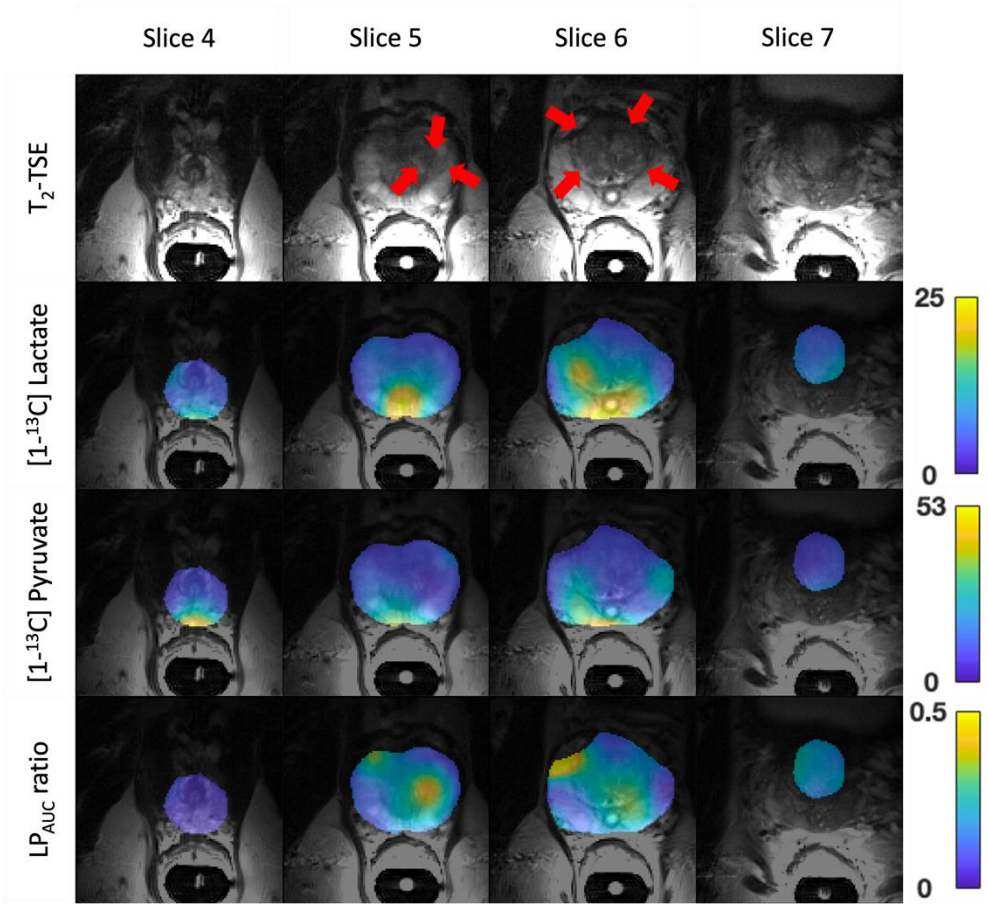

Figure 44 – Total metabolite-specific carbon signal for lactate (second row from top), pyruvate (third row from the top) and the lactate to pyruvate ratio (bottom row), overlaid on T_2-weighted

reference images (top row) for the entire prostate, for subject 1. The tumour position is highlighted by the red arrows (top row).

These were not easily identifiable via mpMRI; however, metabolite-specific total carbon signal maps indicate the presence of a strong lactate signal in the area containing the tumour. The LP_{AUC} ratio map also indicates a high lactate presence, relative to pyruvate at the tumour site, compared to the rest of the prostate (Figure 44).

Region of interest analysis demonstrated the production of lactate at the tumour site, whilst in a nonsuspicious area, as confirmed through histology and mpMRI there was low pyruvate present and little to no lactate signal (Figure 45).

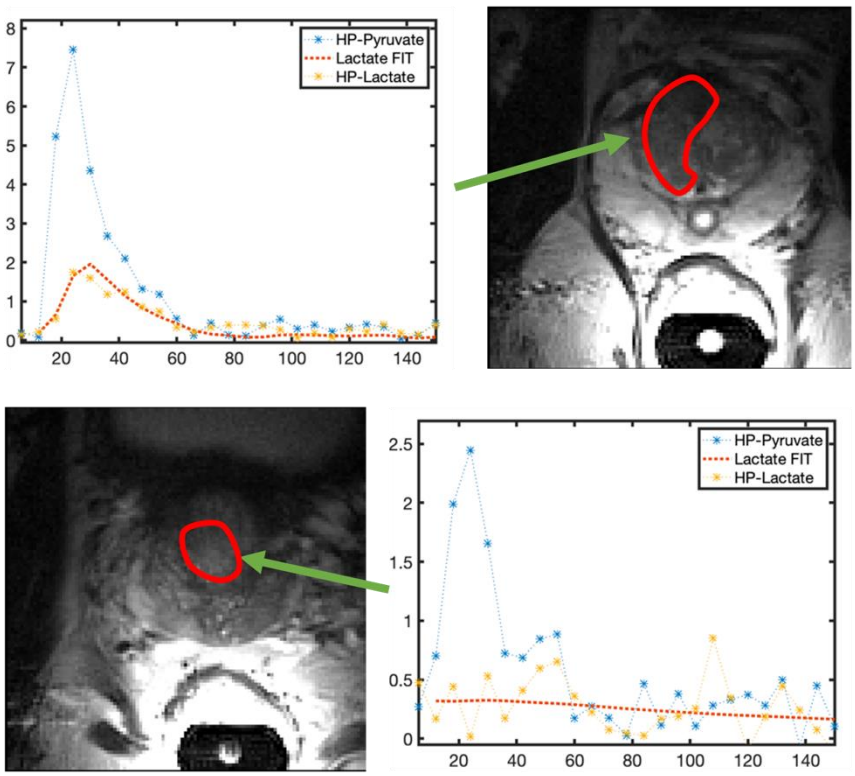

Figure 45 – The change in metabolite Signal to Noise Ratios (SNRs) for pyruvate in blue and lactate in yellow are shown for the biopsy confirmed tumour area (top row) and a healthy region (bottom row), for subject 1. The specific regions of interest are highlighted in red.

Subject 2

Subject 2 possessed an apical anterior, peripheral zone, Gleason grade 3+4, tumour, clearly observable in the mpMRI scans done prior to the hyperpolarised ^{13}C-MR study. The tumour position is highlighted on the mpMRI scans using red arrows (Figure 46).

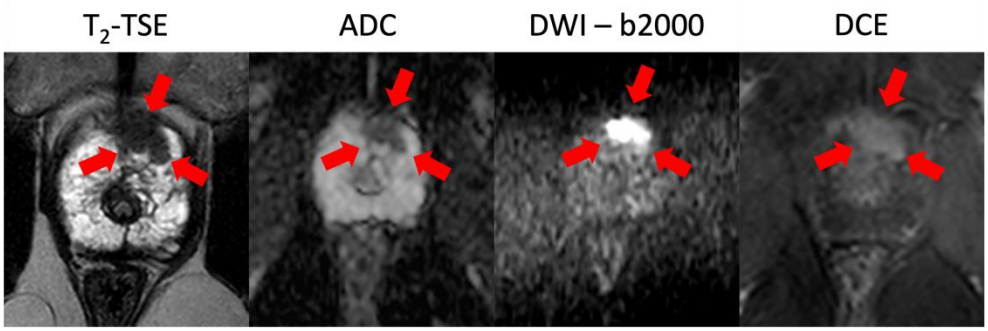

Figure 46 – (From left to right), T_2-weighted turbo spin echo, Apparent Diffusion Coefficient, Diffusion weighted Imaging and Dynamic Contrast Enhanced scans were obtained, for subject 2, prior to the hyperpolarised ^{13}C-MR study. The tumour position is highlighted with red arrows, showing a large anterior, apically positioned, posterior zone tumour.

The tumour spanned several slices on the T_2-TSE performed just before the injection of the hyperpolarised agent. The lactate and pyruvate total signal distributions do not show any particularly strong presence at the tumour site. The LP_{AUC} map, however, indicates the clear presence of a higher lactate to pyruvate presence at the tumour site, relative to the rest of the prostate (Figure 47).

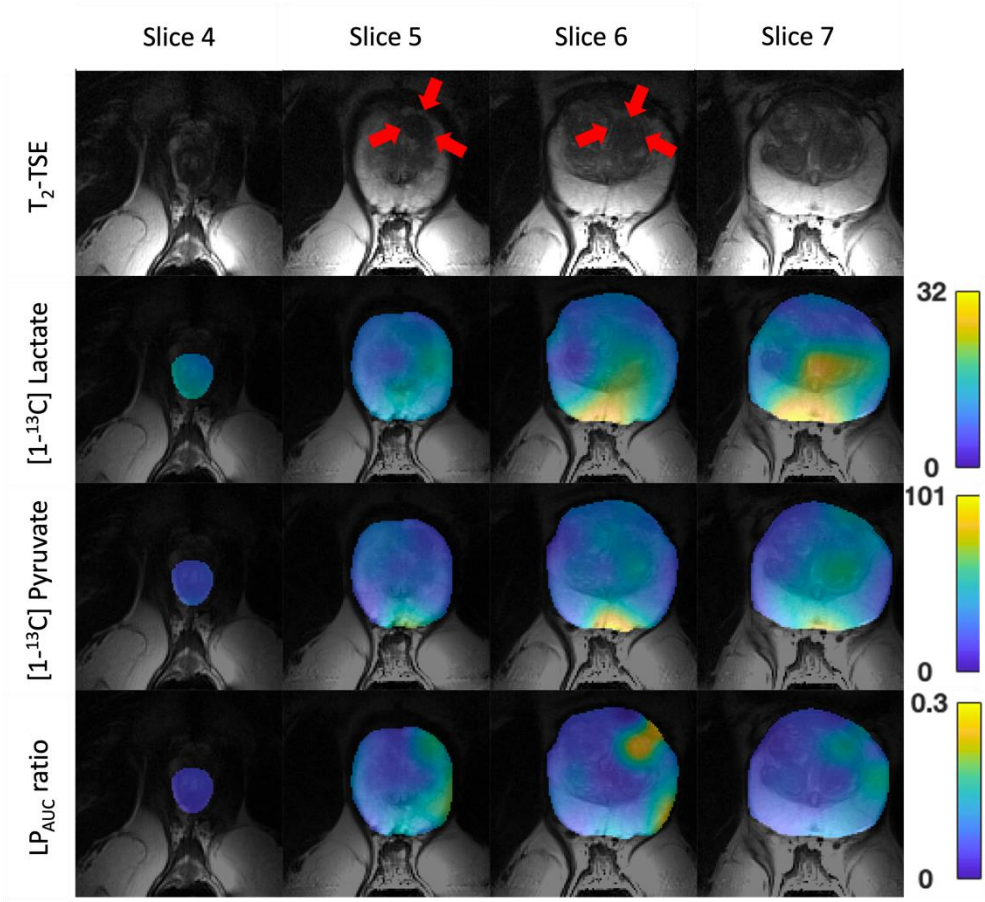

Figure 47 - Total metabolite-specific carbon signal for lactate (second row from top), pyruvate (third row from the top) and the lactate to pyruvate ratio (bottom row), overlaid on T_2-weighted reference images (top row) for the entire prostate, for subject 2. The tumour position is highlighted by the red arrows (top row).

Comparing the metabolite signal time courses (Figure 48) at the tumour site and a healthy area demonstrated a greater amount of lactate at the tumour site. Interestingly, the lactate metabolite SNR is very low in this instance (peak lactate < 2).

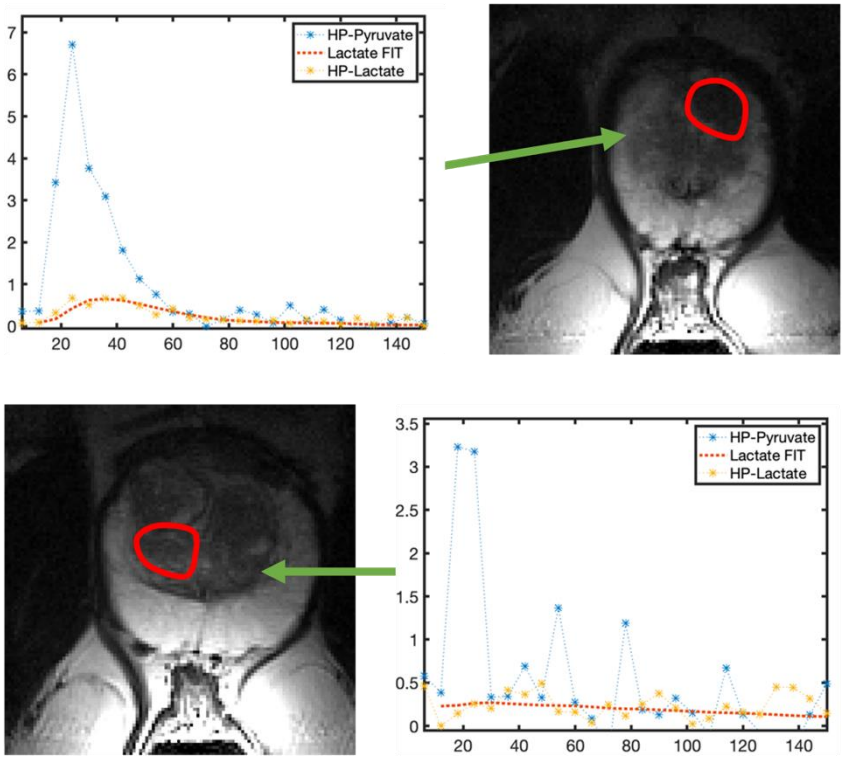

Figure 48 – The change in metabolite Signal to Noise Ratios (SNRs) for pyruvate in blue and lactate in yellow are shown for the biopsy confirmed tumour area (top row) and a healthy region (bottom row), for subject 2. The specific regions of interest are highlighted in red.

Subject 3

Subject 3 had a series of left sided, posterior, mid-gland tumours, highlighted on the mpMRI scans using the red arrows (Figure 49). A biopsy confirmed the tumour as Gleason grade 3+4.

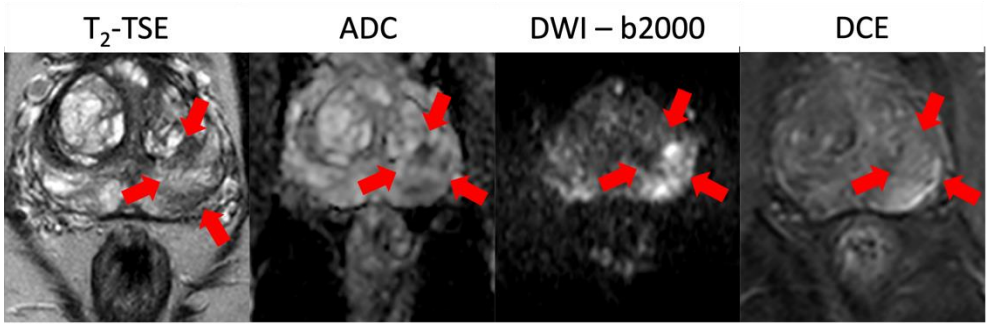

Figure 49 – (From left to right), T_2-weighted turbo spin echo, Apparent Diffusion Coefficient, Diffusion weighted Imaging and Dynamic Contrast Enhanced scans were obtained, for subject 3, prior to the hyperpolarised ^{13}C-MR study. The tumour position is highlighted with red arrows, showing a small, posterior, posterior zone tumour.

The tumours spanned across multiple T_2-TSE slices, as shown below, with no clear pyruvate or lactate localisation in the total metabolite specific maps. The LP_{AUC} ratio maps however, suggest that there is a greater amount of lactate, relative to pyruvate, at the tumour site (Figure 50).

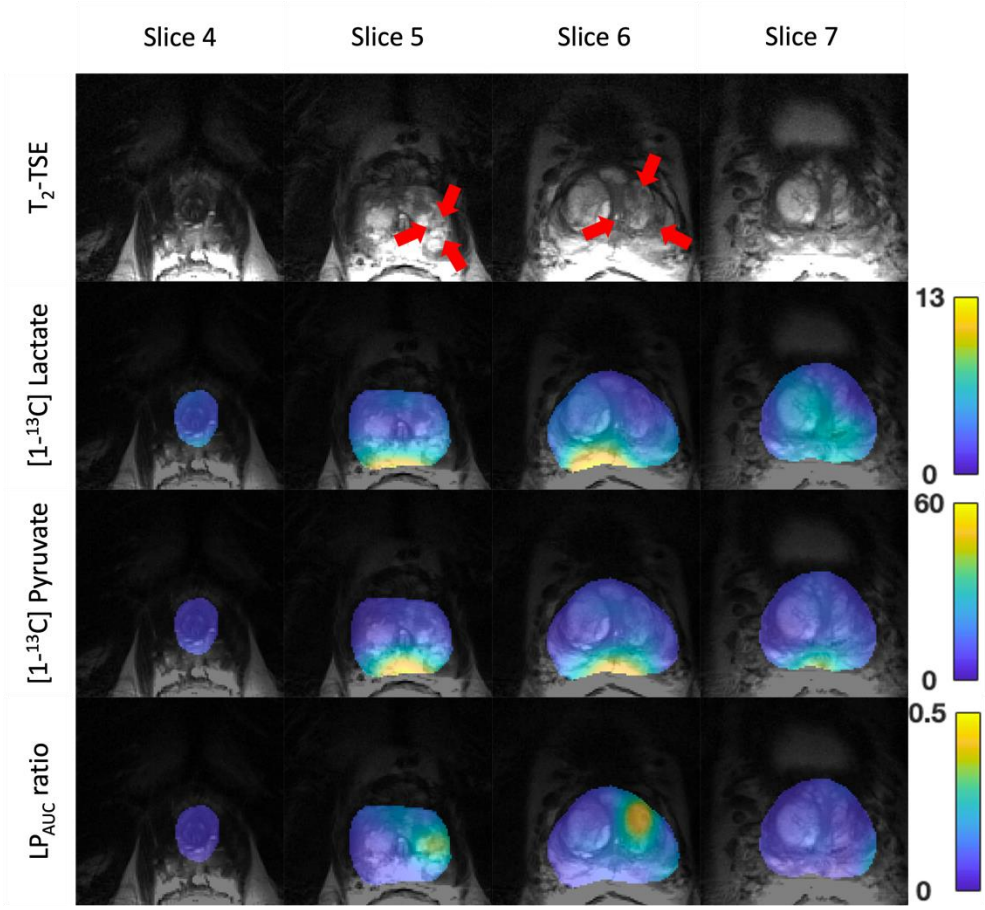

Figure 50 - Total metabolite-specific carbon signal for lactate (second row from top), pyruvate (third row from the top) and the lactate to pyruvate ratio (bottom row), overlaid on T_2-weighted reference images (top row) for the entire prostate, for subject 3. The tumour position is highlighted by the red arrows (top row).

Further analysis of the change in metabolite signals within regions of interest (Figure 51), including the tumour site and a healthy region confirmed the presence of lactate at the tumour site, albeit with a maximum SNR of < 2.

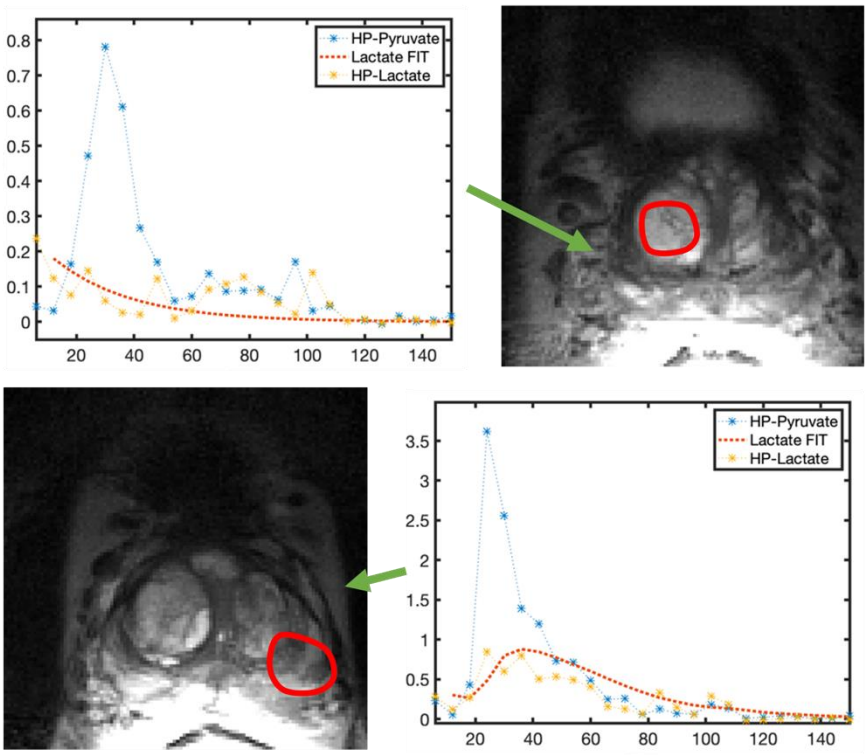

Figure 51 - The change in metabolite Signal to Noise Ratios (SNRs) for pyruvate in blue and lactate in yellow are shown for the biopsy confirmed tumour area (top row) and a healthy region (bottom row), for subject 3. The specific regions of interest are highlighted in red.

Subject 4

Subject 4 possessed a small, left sided, mid-gland, posterior zone tumour, biopsied as Gleason grade 4+3 (Figure 52). The tumour is mpMRI visible and is highlighted by red arrows.

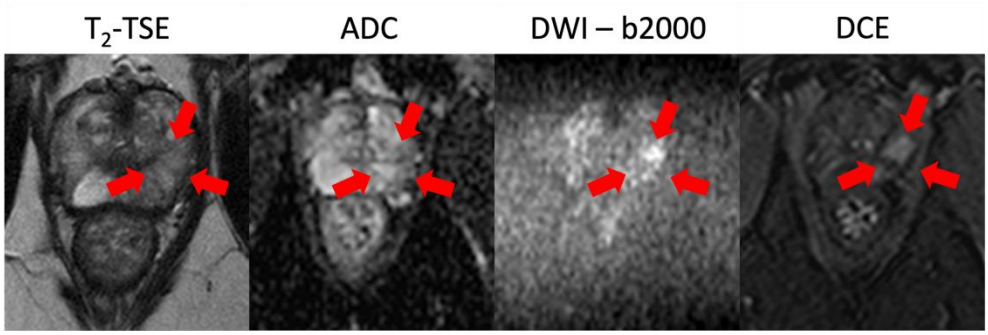

Figure 52 - (From left to right), T_2-weighted turbo spin echo, Apparent Diffusion Coefficient, Diffusion weighted Imaging and Dynamic Contrast Enhanced scans were obtained, for subject 4, prior to the hyperpolarised ^{13}C-MR study. The tumour position is highlighted with red arrows, showing a small, left-sided, apically positioned, posterior zone tumour.

The metabolite specific total carbon signal maps (Figure 53) show strong signals from the tumour site for both lactate and pyruvate maps.

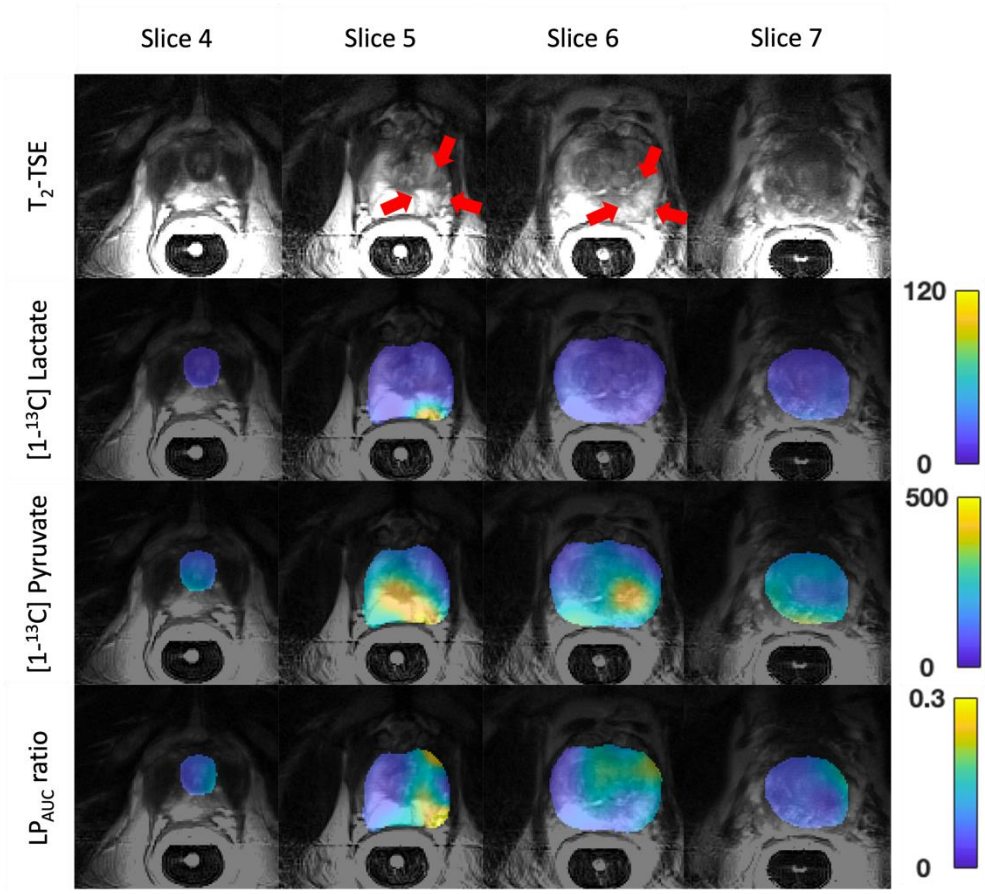

Figure 53 - Total metabolite-specific carbon signal for lactate (second row from top), pyruvate (third row from the top) and the lactate to pyruvate ratio (bottom row), overlaid on T_2-weighted reference images (top row) for the entire prostate, for subject 4. The tumour position is highlighted by the red arrows (top row).

Further analysis of the metabolite signal time courses was performed for regions of interest (Figure 54) at the tumour site and another healthy region, with the former demonstrating a significant amount of lactate, when compared to the latter.

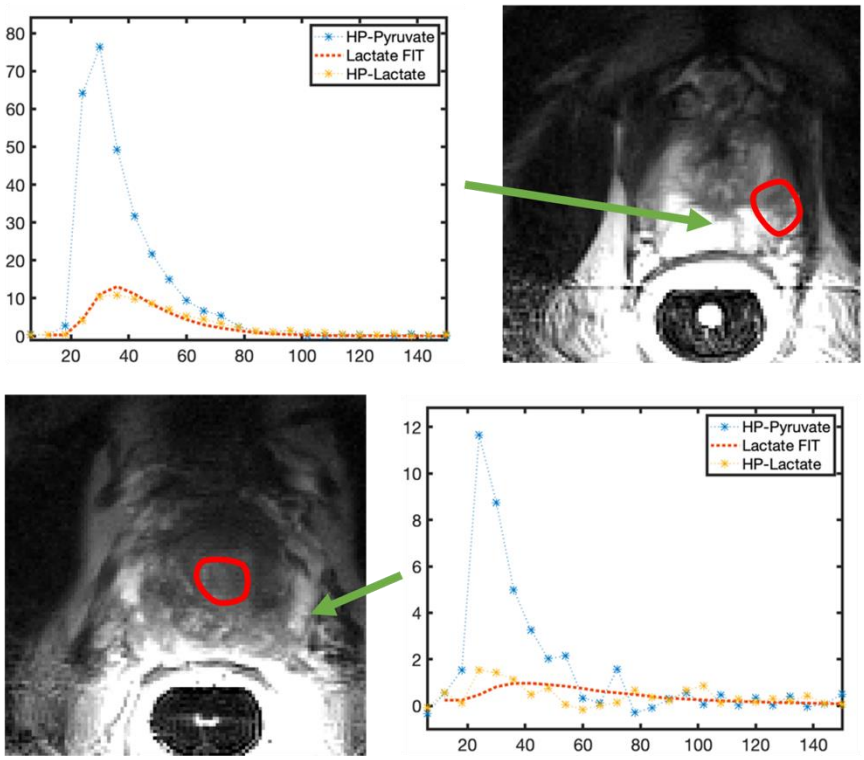

Figure 54 - The change in metabolite Signal to Noise Ratios (SNRs) for pyruvate in blue and lactate in yellow are shown for the biopsy confirmed tumour area (top row) and a healthy region (bottom row), for subject 4. The specific regions of interest are highlighted in red.

Subject 5

Subject 5 possessed a small, left sided, transition zone tumour, which upon biopsy was classified as a Gleason 3+4 tumour (Figure 55). The tumour position is shown on the mpMRI via the red arrows.

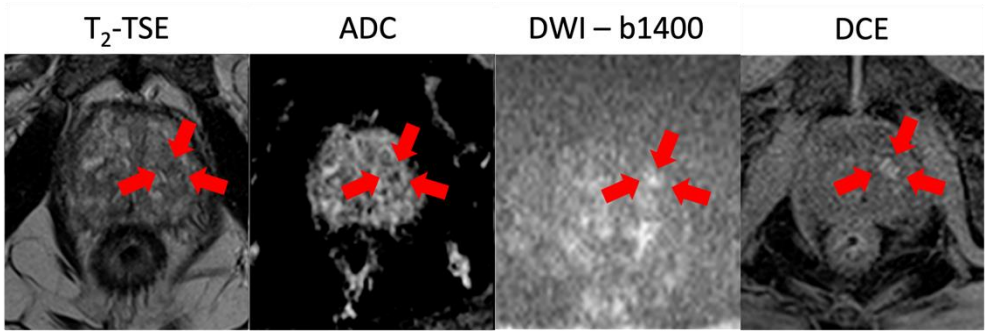

Figure 55 -(From left to right), T_2-weighted turbo spin echo, Apparent Diffusion Coefficient, Diffusion weighted Imaging and Dynamic Contrast Enhanced scans were obtained, for subject 5, prior to the hyperpolarised ^{13}C-MR study. The tumour position is highlighted with red arrows, showing a small anterior, transition zone tumour.

The metabolite-specific total carbon signal maps (Figure 56) do not demonstrate noticeable amounts of either pyruvate or lactate at the tumour site. The LP_{AUC} ratio map, however, shows a significant amount of lactate at the pyruvate site, when compared to pyruvate in the rest of the prostate.

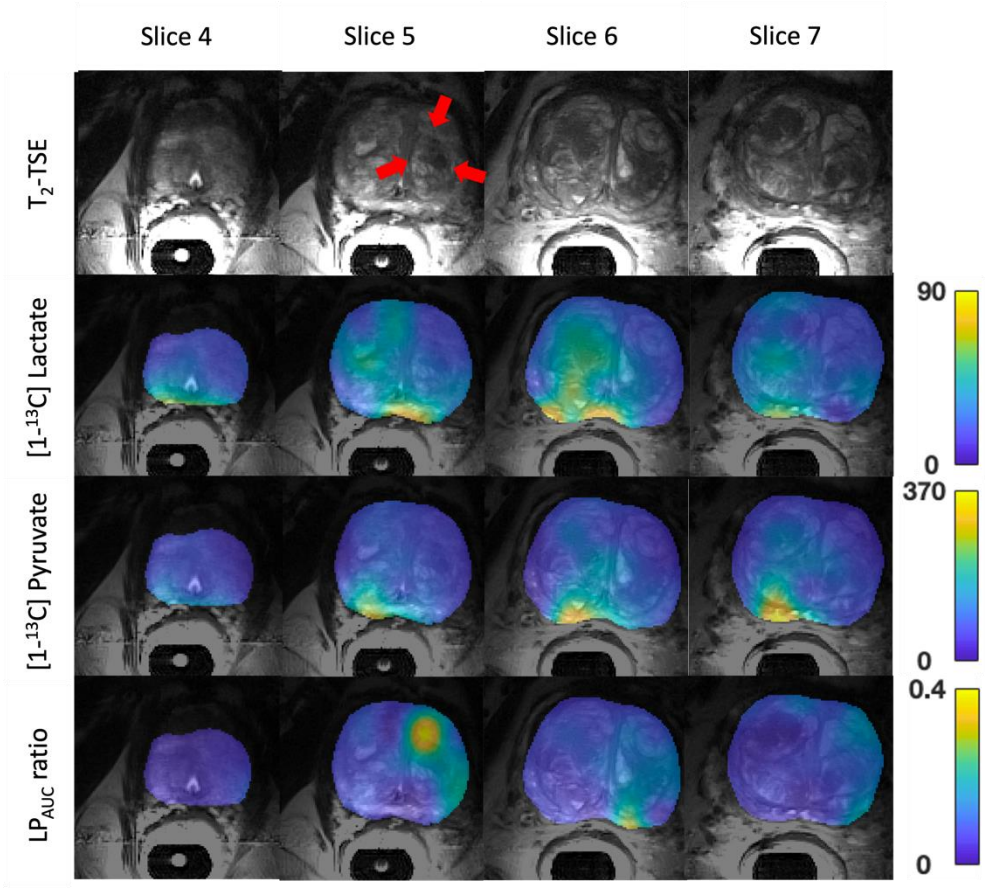

Figure 56 - Total metabolite-specific carbon signal for lactate (second row from top), pyruvate (third row from the top) and the lactate to pyruvate ratio (bottom row), overlaid on T_2-weighted reference images (top row) for the entire prostate, for subject 5. The tumour position is highlighted by the red arrows (top row).

Region of interest analysis (Figure 57) confirms the presence of more lactate (SNR > 5) at the biopsy confirmed tumour site than at a healthy region (SNR < 3).

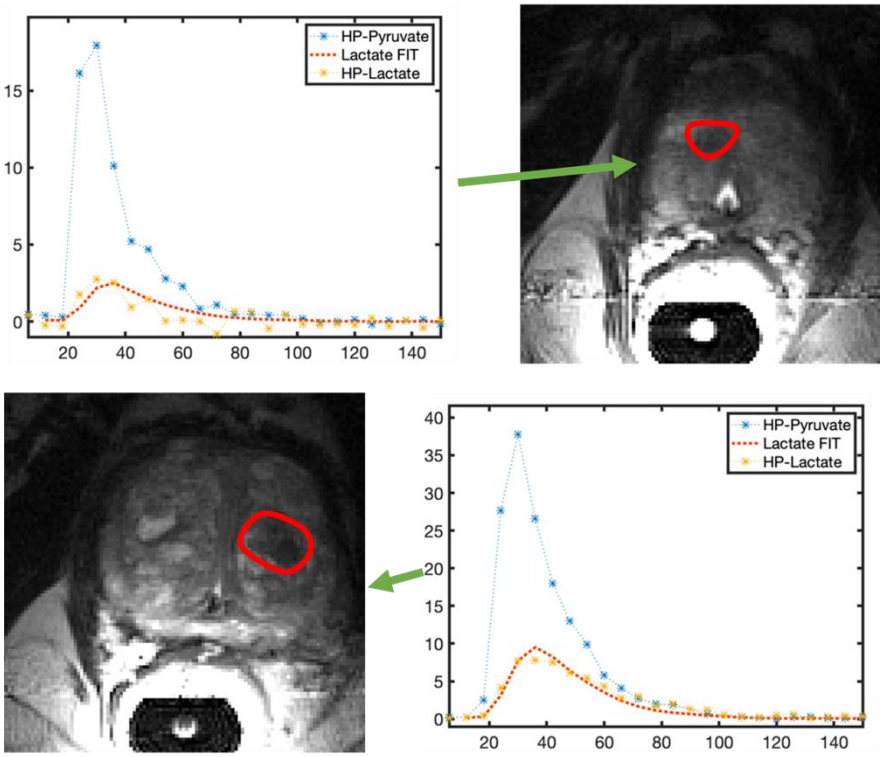

Figure 57 - The change in metabolite Signal to Noise Ratios (SNRs) for pyruvate in blue and lactate in yellow are shown for the biopsy confirmed tumour area (bottom row) and a healthy region (top row), for subject 5. The specific regions of interest are highlighted in red.

Cohort Summary

From the time courses extracted from the tumour sites and healthy regions for each subject LP_{AUC} and k_P values were calculated (Table 10).

Subject	Tumour		Healthy	
	LP_{AUC}	k_P	LP_{AUC}	k_P
1	0.45	0.0366	0.23	0.0015
2	0.27	0.0100	0.12	0.0021
3	0.49	0.0156	0.18	0.0021
4	0.26	0.0220	0.10	0.0070
5	0.39	0.0331	0.18	0.0048
Mean ± SD	0.37±0.10	0.0235±0.0113	0.16±0.05	0.0035±0.0023

Table 10 – Lactate to pyruvate area under the temporal curve (LP_{AUC}) ratio and kinetic rate constant (k_P) calculated for the tumour and healthy regions for all five patients involved in this study

Comparisons of these metrics via boxplots and paired t-tests afforded p values of <0.05, in both instances, indicating a statistically significant difference between the metabolism observed in tumorous and healthy tissue (Figure 58).

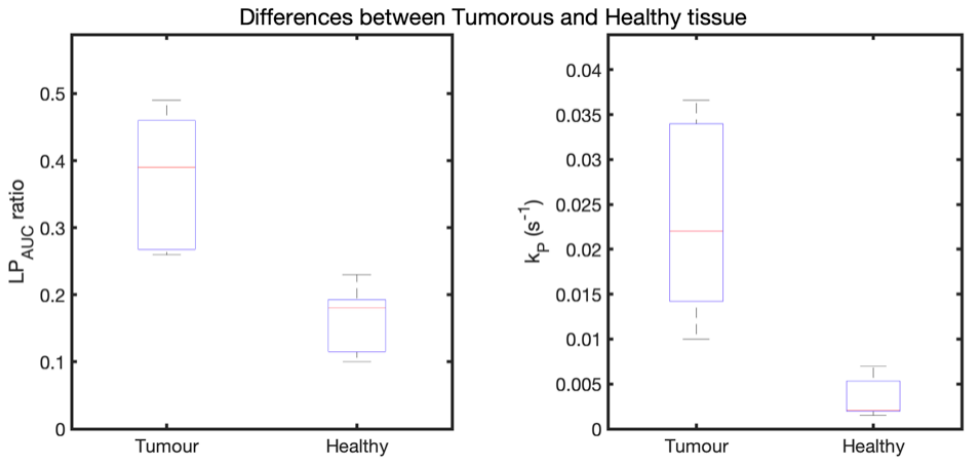

Figure 58 - Boxplots showing the differences in the distributions of LP_{AUC} and k_P values between Tumorous and healthy tissue

Discussion

This study demonstrated the successful implementation of ME-bSSFP as a means of quantifying PCa metabolism using hyperpolarised ^{13}C-MR, as shown by the statistically significant higher degrees of metabolism in tumorous tissue, compared to healthy regions as seen in previous studies [1].

We observed hyperpolarized pyruvate and lactate signals in all patients within this study (n = 5), both within prostate tissue and the rectal wall. These signals were corroborated by non-localized spectroscopic signals acquired during the same scanning sessions. Compared with external coils, an endorectal coil offers the advantage of higher sensitivity, which is critical for studies such as these that are very demanding of SNR [1], [89]. However, their sensitivity profile is spatially dependent; it is highest in the vicinity of the coil and drops off with distance [89]. For this reason, and because of its highly vascular nature, particularly strong lactate and pyruvate signals are seen from the rectal wall. This can result in substantial partial volume effects for nearby posterior tumours, as both may fall within the same voxel and complicate the visual display of metabolite maps. For visualization purposes the image was cropped to display signals from just the prostate region. A higher spatial resolution would be beneficial; however, it should be noted that this would compromise temporal resolution and require a greater number of excitations and phase encoding steps, both of which are likely to negatively impact the longitudinal hyperpolarized signal [46].

ME-bSSFP has been demonstrated as a feasible method by which to quantify PCa metabolism, and whilst the technique is now available for clinical evaluation, further parameter optimization and exploration of strategies such as compressed sensing can be pursued [39]. As mentioned, the of the primary objectives for this study was to achieve full prostate coverage, as such our first compromise, due to the decaying nature of the hyperpolarized signal, involved selecting a 3D

volume with lower spatial resolution, over a high-resolution single-slice acquisition. Due to the greater number of pulses introduced through having to excite multiple slices, which inevitably decay the hyperpolarized state faster, a larger voxel size was employed to maximize the potential signals acquired. The voxel size finally selected was chosen such that signals from the largest prostates, with potential tumours up to 60 mm away from the endorectal could be acquired. Finer resolutions may be possible, however, would require compromising full organ coverage.

Another technical limitation of this study involves the metrics used to quantify the metabolite information obtained during the hyperpolarised ^{13}C-MR studies. Whilst previous studies have been performed, attempting to identify an optimal metric, there is still no consensus amongst the hyperpolarised ^{13}C-MR community. LP_{AUC} and k_P were chosen in this instance due to their use in other hyperpolarised ^{13}C-MR studies involving PCa.

The small cohort size in this study is not sufficient to make conclusions regarding biological trends in larger populations. It was, however, of sufficient size to demonstrate, as a proof-of-concept, the ME-bSSFP sequence's propensity for metabolic prostate imaging, using hyperpolarised ^{13}C-MR. Further, larger scale, studies will be required to further define the role of hyperpolarised ^{13}C-MR in the diagnosis and treatment of PCa.

Summary

This study demonstrated the optimization and application of a ME-bSSFP sequence in the metabolic imaging of PCa in conjunction with hyperpolarized ^{13}C-MRI. We successfully demonstrated, with whole organ coverage, quantitative differentiation of metabolism in tumorous and healthy tissue in 8 patients using the same ME-bSSFP imaging protocol

Chapter 8: Metabolic imaging of Pheochromocytoma

A clinician, external to UCL, approached the hyperpolariser team with the aim of imaging the world's first pheochromocytoma using hyperpolarised ^{13}C-MR. Similar to the prostate work the author manned the MR control room, whilst a research technician dealt with the preparation of a clinical fluid path and subsequent handling of the hyperpolarised agent. A clinical team composed of two clinicians and a nurse were involved in recruiting and handling the patient on the day of the scan. The author performed all data processing and data analyses. The publication arising from this work was written by the author and the aforementioned external clinician.

Aims

This work sought to demonstrate the feasibility of quantifying the metabolism of a type of neuroendocrine tumour, pheochromocytoma, through the injection of hyperpolarised [1-^{13}C] pyruvate and subsequently ^{13}C-MRSI. A portion of this work is has been published by the British Journal of Radiology: Case Reports.

Background

Pheochromocytomas (PCC) and paragangliomas (PGL), cumulatively referred to as PPGLs, are neuroendocrine tumours arising from neural crest-derived cells in the sympathetic and parasympathetic nervous systems [90]. PCCs form in the centre of the adrenal gland whilst PGLs form outside [91]. Predicting future tumour behaviour and the likelihood of metastatic disease remains problematic as genotype-phenotype correlations are limited, disease has variable penetrance and, to date, no reliable molecular, cellular or histological markers have emerged [92].

At present, imaging modalities for PPGLs can be either anatomical: Computed Tomography (CT) and Magnetic Resonance Imaging (MRI), functional, scintigraphy and Positron Emission Tomography (PET) or a combination of both methods (SPECT/CT or PET/CT). Anatomical imaging methods follow clinical suspicion and positive biochemical tests, with the role to detect and locate a PPGL. Once this has been obtained, functional imaging can be utilised to confirm the source of the increased production of catecholamines. For most cases, ^{123}I-MIBG scintigraphy, ^{18}F-FDG PET or Gallium-68 Dotatate PET/CT is used [91]. These imaging modalities may be able to inform the presence of PPGL, but they are unable to delineate tumour characteristics. Despite recent advances, malignancy in PPGLs can only be defined in advanced stages, and the inability to predict tumour behaviour does not allow for optimal therapeutic planning.

A non-invasive imaging modality capable of quantifying tumour metabolism would greatly aid PCC diagnosis and treatment planning. The limitation of both CT and functional imaging is radiation exposure, which needs to be limited in subjects who need life-long surveillance and multiple scans. Notably, PET imaging does not provide an understanding of intrinsic cellular metabolism, which is instead inferred from cellular uptake of a given isotope and consequently tumour localisation. A non-ionising alternative to exploring tumour metabolism could involve hyperpolarised ^{13}C-MR.

Organic molecules involved in the TCA cycle can be labelled with carbon-13, an MR active nuclei; these however exist at relatively low *in vivo* concentrations (approx. 1.1%) [93]. The signal from these carbon-13 labelled metabolites can be boosted via dissolution dynamic nuclear polarisation d-DNP, a form of hyperpolarisation wherein the molecules gain nuclear spin (polarisation) exceeding thermal equilibrium by 10^4-10^5 fold [1]. These hyperpolarised carbon-13 molecules can then be injected *in vivo* and their conversion into other metabolites recorded via ^{13}C-MR [2]. Recent clinical studies have focused on analysing the Warburg effect with several tumour

types tested; but to date no work has analysed PPGL metabolism via hyperpolarised ^{13}C-MR [1], [2], [36].

An individual with histologically confirmed PCC were recruited for a pilot study to explore the feasibility of quantifying neuroendocrine tumour metabolism through hyperpolarised ^{13}C-MR using ME-bSSFP.

Methods

All data processing was performed using previously described MATLAB tools (MathWorks, Natick, MA, USA), bSSFP echo data was resolved using an IDEAL model. All MR-based patient work was performed using a 16 channel, receive only, surface coil, containing a 1ml, 8M [^{13}C] Urea phantom, for power calibration, (Rapid Biomedical GmbH, Rimpar, Germany) on a 3T Siemens Biograph mMR (Siemens, Munich, Germany).

Tumour characteristics

	PG001
Tumour size (mm x mm)	65x41
Location	Right adrenal
^{18}F-FDG	Some avidity
^{68}Ga-Dotatate	High avidity
^{123}I-MIBG	Some avidity
Plasma metanephrines	Raised
Status	Slowly spreading widespread metastatic disease
Treatment	Chemotherapy

Table 11 - Tumour size, location, status, and response to PET scans performed before the start of this study.

The subject was recruited due to the presence of a large pheochromocytoma. Written informed consent to participate in an abdominal hyperpolarised ^{13}C-MR study was obtained from the subject. This study was conducted as part of the Hyperpolarised ^{13}C-Pyruvate Study (ID: NCT03687645).

PET/CT scans

Existing PET/CT scans were used to recruit individuals to this study, ^{123}I-MIBG, ^{68}Ga-Dotatate and ^{18}F-FDG images were overlaid on a reference CT scans.

Preparation of hyperpolarised [1-^{13}C] pyruvate

[1-^{13}C] pyruvic acid was mixed with AH111501 electroparamagnetic agent and loaded into a GE fluid path (GE Healthcare, Chicago, Il). This was irradiated with microwaves at <1K for approximately 3h in a clinical hyperpolariser (SPINLab, GE Healthcare, Chicago, Il), resulting in a polarisation level of 25%. The frozen sample was then dissolved with sterile water (38ml) and neutralised with 17.5g sterile trometamol buffer (333mM Tris and 600mM NaOH); affording 40ml of hyperpolarised [1-^{13}C] pyruvate solution. This was then injected into the subject within 78s with MR acquisition beginning immediately after the completion of injection (12s).

^{1}H-imaging

The tumour position was anatomically localised using T_2-weighted scans, performed in the axial: field of view: 250x250x30mm; matrix size: 192x192x10; slice thickness: 30mm; TR: 5640ms; ΔTE: 108ms; No. of echoes: 15; flip angle: 90°; NSA: 3 and coronal: field of view: 460x370x30mm; matrix size: 256x206x10; slice thickness: 30mm; TR: 5630ms; ΔTE: 107ms; No. of echoes: 15; flip angle: 90°; NSA: 3; planes.

Prior to contrast injection a dual echo gradient sequence: field of view: 250x250x30mm; matrix size: 256x256x1; slice thickness: 30mm; TR: 4.8ms; ΔTE: 107ms; No. of echoes: 2; flip angle: 15°; NSA: 1; was employed to assess the inhomogeneity across the field of view. A field map was calculated from this and used in post-processing as part of a custom IDEAL algorithm.

^{13}C-imaging

Four consecutive 2D multiecho-balanced steady state free precession (me-bSSFP) acquisitions with: field of view: 250x250x30mm; matrix size: 12x12x10; slice thickness: 30mm; TR: 15.8ms; ΔTE: 11ms; No. of echoes: 7; flip angle: 30°; NSA: 16; were acquired immediately after the completion of injection.

A nonlocalized spectroscopy sequence: TR: 1ms; flip angle: 10°; NSA: 1, BW: 4000Hz was then acquired. This was followed by another set of four me-bSSFP acquisitions and an FID. This was repeated for a total acquisition time of 2m30s.

Data processing

A previously described IDEAL algorithm with a bipolar echo correction, utilising an *a priori* field map was used to resolve the echo data afforded by the 2D me-bSSFP, with the nonlocalized spectra used to identify the frequency of the metabolites; this was done to afford maps of [1-^{13}C] pyruvate and its downstream metabolites [44], [60], [94]. Analysis was performed on regions of interest, with the mean SNR of each ROI found for each individual metabolite and plotted as a function of time post-injection. SNR was defined as the mean signal from the voxels within an ROI, for a given time point, divided by the standard deviation within the ROIs at the last time point recorded (2m30s post-injection).

Results

PET/CT imaging

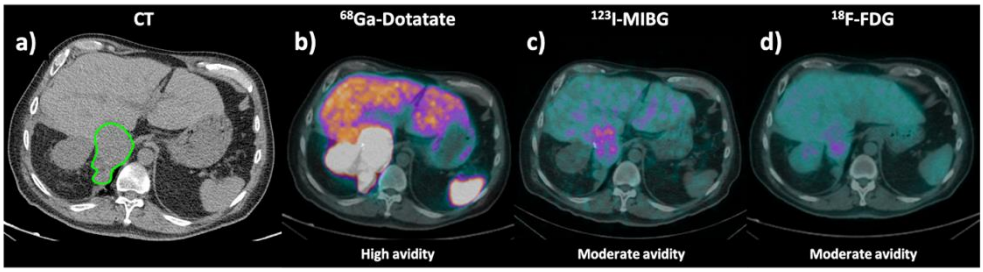

Figure 59 - PET scans using a range of contrasts, ^{18}F-FDG, ^{68}Ga-Dotatate and ^{123}I-MIBG, overlaid on a reference CT image. The relative avidity of each contrast to the tumour site is also mentioned.

The moderate avidity observed in the ^{18}F-FDG scans is consistent with the modality's low specificity to neuroendocrine tumours (Figure 59) [95]. The avidity in both instances of ^{123}I-MIBG, radiologically confirms these as neuroendocrine tumours, due to the compound's similar structure the catecholamine norepinephrine, a molecule commonly secreted by PCCs [96].

^{1}H imaging

Prior to injection with hyperpolarised [1-^{13}C] pyruvate, multiplanar T_2-weighted MRI was performed to localise the tumour (Figure 60). Due to the 2D nature of the carbon-13 imaging sequence, careful placement of the field of view was required. The tumour was outlined in green on each image.

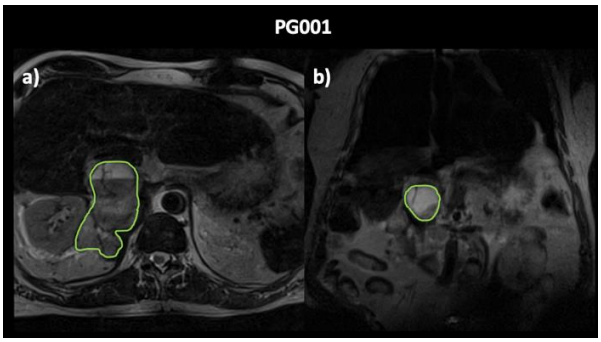

Figure 60 – T_2-weighted axial and coronal images for PG001; (a) and b) respectively) acquired minutes before the injection of hyperpolarised 1-^{13}C-pyruvate to localise the tumour. The tumours are outlined in green in each instance.

The ^{1}H-images show a large right-sided tumour near the adrenal gland. The axial plane (left) shows a cystic portion in the tumour, reflected by the brighter signal within the region of interest (ROI).

^{13}C-MRSI

Nonlocalised spectroscopy

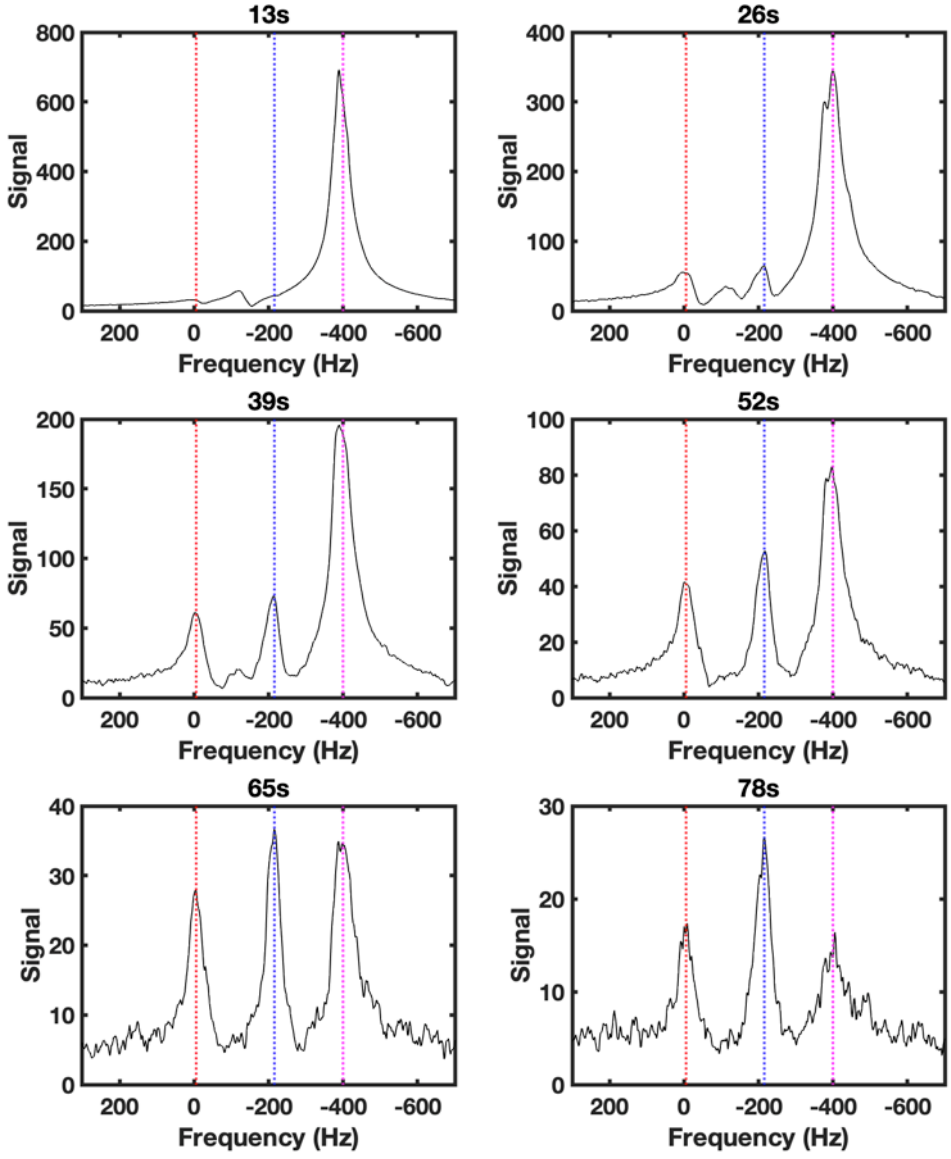

Figure 61 – Change in nonlocalised spectroscopy signals, up to 78s after the completion of injection of hyperpolarised [1-^{13}C] pyruvate. Spectra for PG001 are shown, in each the peak positions for: [1-^{13}C] lactate (0Hz – red dashed line), [1-^{13}C] alanine (~-200Hz – blue dashed line) and [1-^{13}C] pyruvate (~-400Hz – magenta dashed line) are highlighted.

Dynamic imaging

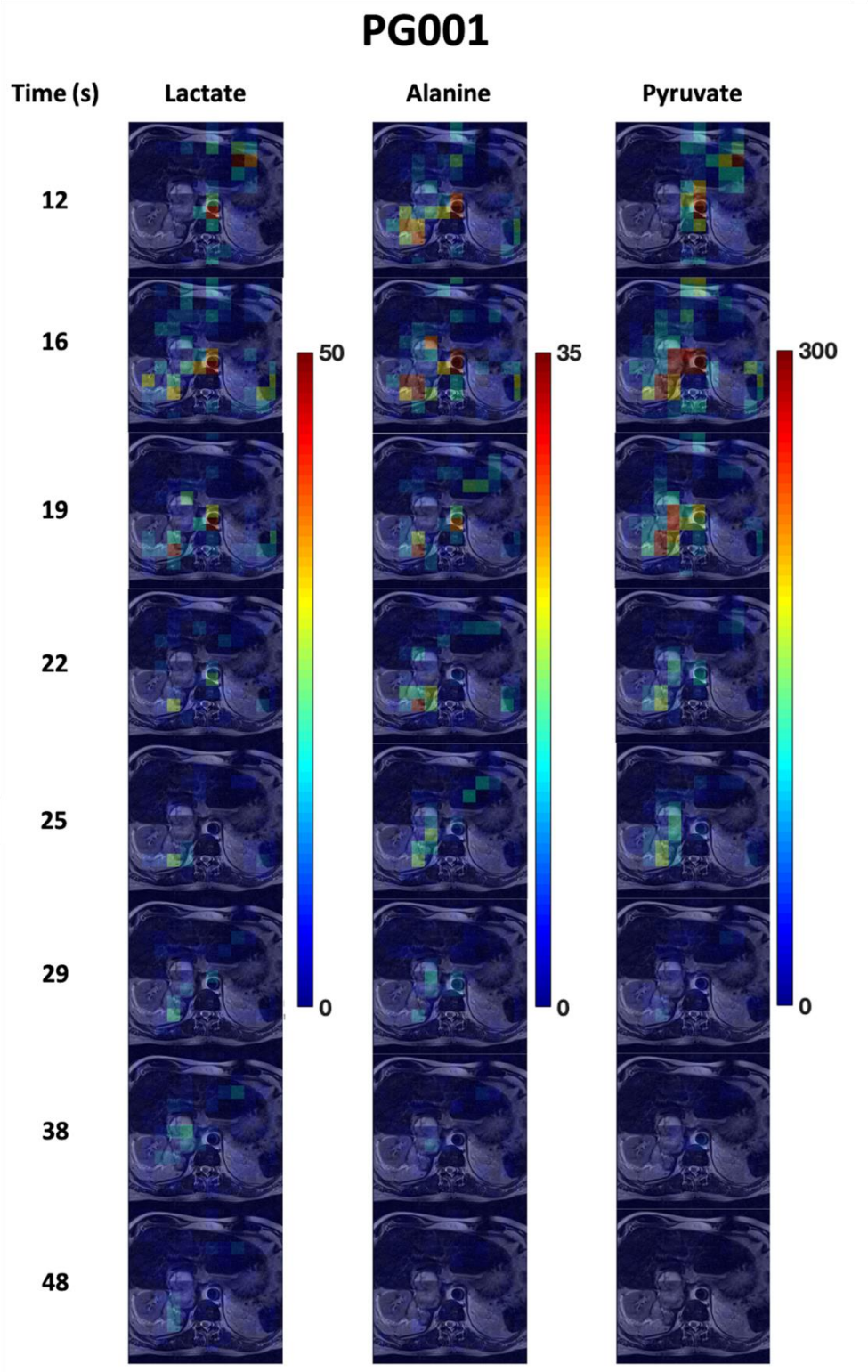

Figure 62 – Change in metabolite maps derived from the bSSFP data, overlaid on a reference T2-weighted image, for [1-13C] lactate (left), [1-13C] alanine (centre) and [1-13C] pyruvate (right) for PG001.

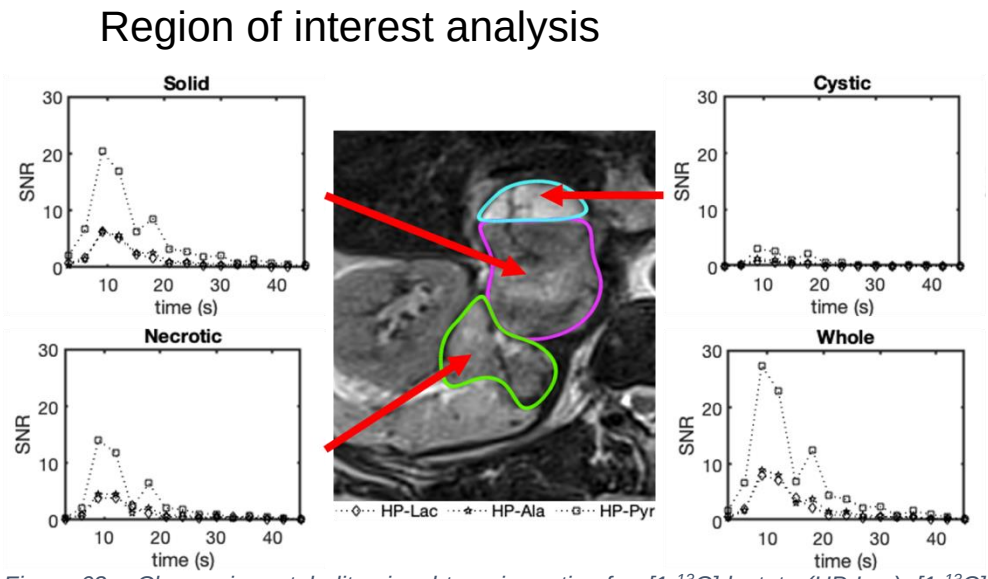

Figure 63 – Change in metabolite signal to noise ratios for: [1-^{13}C] lactate (HP-Lac), [1-^{13}C] alanine (HP-Ala) and [1-^{13}C] pyruvate (HP-Pyr) over time at the tumour site. The SNRs reflect the mean value from each ROI at each time point. The 'Whole' time point is a combination of the other three ROIs with the mean SNRs calculated at each time point.

Nonlocalised ^{13}C-MR spectra (Figure 61) were used to confirm the presence of the hyperpolarised [1-^{13}C] pyruvate (~ -400Hz) and its downstream metabolites ([1-^{13}C] lactate: ~ 0Hz and [1-^{13}C] alanine: ~ -200Hz). A large [1-^{13}C] pyruvate signal is seen, lasting up to 65s, post-injection. [1-^{13}C] lactate is also observed up to 65s, post-injection for PG001. [1-^{13}C] alanine is also seen, up to 78s, post-injection.

Metabolite maps (Figure 62) for [1-^{13}C] lactate, [1-^{13}C] alanine and [1-^{13}C] pyruvate were extracted from the bSSFP echo data using an IDEAL model and then overlaid on to axial reference images. The time course images show initial signals, of all three metabolites, within the aorta, up to 22s after the completion of injection. Metabolite signals appear very well localised to the tumour from 16s and onwards.

At 12s after the completion of injection, a strong signal is observed at the top right of the [1-^{13}C] lactate and [1-^{13}C] pyruvate maps which can be attributed to signal bleeding from the heart, which is attributed to the large slice thickness (30mm) used for the bSSFP acquisition. The bolus then travels to the aorta (12-22s) and appears at the tumour site (12s and onwards for alanine; 16s for [1-^{13}C] lactate and [1-^{13}C] alanine. Region of interest analysis demonstrates the presence of all

metabolites within the tumour from 12s onwards, although this is not apparent in the dynamic imaging figure due to image scaling. The [1-^{13}C] lactate and [1-^{13}C] alanine signals appear to be localised to the solid and necrotic portions of the tumour, with little in the cystic region (Figure 63).

ROI	Lac/Pyr AUC	Ala/Pyr AUC
Whole tumour	0.33	0.36
Cystic	0.16	0.14
Solid	0.30	0.33
Necrotic	0.37	0.40

Table 12 - Area under the curve ratios for lactate to pyruvate (Lac/Pyr AUC - middle column) and alanine to pyruvate (Ala/Pyr AUC - right hand column) signal to noise ratios (SNR)s, within the different ROIs identified (left hand column).

The similar area under the curve (AUC) ratios across all ROIs (Table 12) suggest similar levels of activity for alanine aminotransferase (ALT) and LDH (Table 1). The necrotic tissue possesses a higher lactate to pyruvate and alanine to pyruvate AUC ratio than the solid region, whilst the cystic portion had the lowest values.

Discussion

This work successfully demonstrated the application of hyperpolarised ^{13}C-MR with ME-bSSFP to record the conversion of pyruvate into both lactate and alanine.

Non-localised spectroscopy showed [1-^{13}C] pyruvate (~ -400Hz), [1-^{13}C] alanine (~ -200Hz) and [1-^{13}C] lactate (~ 0Hz). The presence of [1-^{13}C] lactate could be due to several factors: label exchange of the carbon-13 labelled carboxylic acid group via free lactate dehydrogenase (LDH), either in the tissue or within the blood; or the enzymatic conversion of [1-^{13}C] pyruvate into [1-^{13}C] lactate via LDH, which could be indicative of the Warburg effect. Similarly, the presence of [1-^{13}C] alanine could be due to either cell proliferation, muscular degradation (Cahill cycle) or liver damage; wherein pyruvate is converted into alanine through the enzyme alanine aminotransaminase (ALT). Nonlocalised spectroscopy demonstrates that metabolic processes can be tracked through ^{13}C-MR, following the injection of hyperpolarised [1-^{13}C] pyruvate. It, however, provides no spatial localisation and as such we must turn our attention to the metabolite maps acquired to better understand the processes occurring.

The metabolite maps show the presence of [1-^{13}C] pyruvate, [1-^{13}C] lactate and [1-^{13}C] alanine in the aorta for both subjects; suggesting that [1-^{13}C] pyruvate metabolism and enzyme mediated label exchange (in the case of [1-^{13}C] lactate generation) is underway prior to the bolus arriving at the tumour site.

Further observation shows the presence of [1-^{13}C] lactate at the tumour site. In line with previous cancer models using hyperpolarised ^{13}C-MR, this is likely due to the anaerobic conversion of [1-^{13}C] pyruvate to [1-^{13}C] lactate, through LDH, defined as the Warburg effect, which is enhanced in cancer cell metabolism[97]. LDH is the primary metabolic enzyme that converts pyruvate to lactate and vice

versa. LDH also plays a role in regulating nutrient exchange between tumour and stroma. Higher levels of LDH are therefore commonly found in tumours [2], and have been reported in PPGLs [98]. It is therefore not surprising that we observed [1-^{13}C] lactate signal primarily within tumour tissue, as has been observed for other tumour types [2], [79].

In the context of prostate cancer, the LP_{AUC} ratio has been suggested to correlate directly with tumour grade and consequently aggressiveness [79]. A larger cohort is required to identify the relevance of this metric, with respect to PPGLs and how these may contribute to characterisation and delineation.

Alanine is observed in the aorta and is seen clearly at the tumour site for the subject. Its presence could be due to the upregulation of alanine production, through cell proliferation, due to spreading metastatic disease. A recent study demonstrated the relationship between cell proliferation and alanine generation in breast cancer cells, and although no evidence has been found to date for PPGLs, this could be a potential mechanistic explanation behind the presence of alanine in PG001's tumour[99].

The appearance of [1-^{13}C] lactate and [1-^{13}C] alanine in the aorta can be attributed to free ALT and LDH within the blood. These enzymes are known to be present within the plasma in relatively small concentrations [100]; and LDH is abundant within red blood cells (RBCs) [101] with elevated levels indicative of haemolysis [102]. ALT is found mainly in the liver and muscle with high levels related to damage to liver cells [103]. Others have also observed [1-^{13}C] lactate signals within blood [104], this could be due to exchange of the carbon-13 label between the hyperpolarised [1-^{13}C] pyruvate and endogenous blood lactate occurring within the cytoplasm of RBCs [101]. Hyperpolarised [1-^{13}C] alanine signals have been observed in muscle and are likely related to high levels of ALT within muscle cells, however, there have been no previous reports of [1-^{13}C] alanine signal

within the blood itself. In both subjects, alanine was clearly observed both within blood and tumour.

Limitations of this study include the fact that the bSSFP sequence used involved the acquisition of only a single slice, limiting the spatial information obtained. This led to signal bleeding into the field of view from other organs, such as the heart, as seen in the [1-^{13}C] pyruvate and [1-^{13}C] lactate metabolite maps, for PG001. Furthermore, the spatial resolution of these acquisitions, in comparison to clinically used sequences, was very coarse at 21 x 21x 30mm per voxel. As the tumour in the study contained cystic, solid and necrotic portions a higher spatial resolution would allow for analysis and comparison of these tissue types.

A disadvantage of PET tracers is that uptake varies, depending on tumour type, across all radiotracers, as shown by the low ^{18}F-FDG avidity for PG001. This may require a subject being exposed to multiple ionising tracers to delineate their tumours. Hyperpolarised ^{13}C-MR, as shown here does not appear to discriminate against tumour type[1], [2]. Conversely, certain nuclear imaging modalities are specific to PPGLs e.g., Iobenguane (MIBG). Hyperpolarised ^{13}C-MR, in its current form does not afford this type of detail regarding specific tumour type or therapeutic possibilities.

Further studies will be necessary to define the role of hyperpolarised ^{13}C-MR in PPGL-associated disease with respect to diagnostics, prognostication, and longer-term disease surveillance. This will include defining the significance of the metabolite signals and the modality's ability to differentiate PPGLs according to size; anatomical position; metastatic potential and response to therapy. Hyperpolarised ^{13}C-MR may provide a prognostic tool to risk stratify for more aggressive PPGLs as well as identifying which patients require closer, longer-term follow-up.

Summary

This first- in-man pilot study has demonstrated that hyperpolarised ^{13}C-MR has the potential to provide a non-invasive, *in vivo*, metabolic assessment of human PPGLs. Whilst further study and improvement to acquisition techniques are required to delineate its role in diagnosis and surveillance, its ability to provide both radiological and functional data without radiation exposure remains the key advantage – particularly in the FPS where life-long surveillance is required.

Section D

The following section contains a single chapter which outlines potential directions for future work involving the dynamic phantom, further ME-bSSFP and clinical studies.

9. Further Work

As is often the case with research, time is a limiting factor in determining both what can be planned for and what is achieved. In short, there is always scope for improvement. The following outlines potential further work in the sections previously presented in this body of work.

Dynamic phantom

The reproducibility study used a dual channel $^{1}H/^{13}C$ endorectal coil, with a built in [^{13}C] urea reference standard. Other MR coils, such as the surface coil used in the pheochromocytoma study do not contain built in reference standards and require the use of an external phantom for both power calibration and the centring of the system's transmit frequency. An integrated reference standard, within the dynamic phantom would eliminate the need for an external reference phantom in the coil.

An inefficiency of the reproducibility experiments was that only 11ml of hyperpolarised [1-^{13}C] pyruvate was used at a time, where batches of 40ml were produced at a time. Moreover, the single chamber design of the phantom only allows for one enzyme concentration to be used per experiment. A potential improvement would involve the development of a multichambered phantom, with a mixing mechanism and the capacity for an integrated remote injection system, included for every chamber. Such a design would improve the inefficiencies described above and allow for multiple concentrations, or even different enzymes to be imaged simultaneously.

Previous work has suggested a range of metrics by which to quantify hyperpolarised ^{13}C-MR, from kinetic models to ratio-based methods comparing changes in metabolite SNR over time [50], [79]. A consensus, however, has yet to be reached, limiting the potential for cross site trials. An optimal metric would allow for the quantification of metabolism, independently of scanner hardware and acquisition techniques.

A study using the dynamic phantom developed in this body of work could involve performing a series of hyperpolarised ^{13}C-MR experiments, with varying enzyme concentration within the phantom. Variation of the amount of enzyme will allow for various metrics to be extracted, with the optimal metric correlating most closely to variations in enzyme concentration.

The experimental reproducibility of the phantom system would allow for the study to be performed on different scanners and at different sites. Pursuing such work would allow for an optimal metric to be confidently identified, as well a gain in understanding of the impact of different hardware and acquisition techniques on the data.

Processing methods

An evident limitation of using the endorectal coil is the impact its inhomogeneous reception profile has on the images of the prostate. Previous work has explored sensitivity profile corrections in spectroscopic imaging using an endorectal coil [105]. Whilst initial modelling of an endorectal coil's sensitivity profile was performed, attempts at integrating this into the data processing pipeline for clinical data would be of interest.

Sequence optimisation

The spatial resolution used for the hyperpolarised ^{13}C-MR pCa imaging, is suitable for the purposes for demonstrating metabolism in specific areas of the prostate and large tumours. Clinically, however,

pCa tumours are often smaller and the metabolic measurements currently acquired are a combination of healthy and diseased tissues, due to the large voxel size employed by the ME-bSSFP.

Finer spatial resolutions are possible; however, this can also have a detrimental impact. Firstly, a higher resolution, using ME-bSSFP would require the application of more phase encoding steps, contributing to the faster decline of the hyperpolarised state. Secondly, as a direct consequence of a greater number of phase encoding steps, the total acquisition time will proportionally increase. Thirdly, if we were to maintain our FOV the increase in spatial resolution and subsequent decrease in voxel volume would also result in a loss in SNR between measurements.

Preserving the polarised state and achieving a high spatiotemporal resolution were two of the challenges identified in the beginning of this work, in theory, increasing spatial resolution would make both more difficult to deal with. Several compromises, however, can be employed to account for an increased spatial resolution. Reducing the number of imaged slices to cover only the prostate would reduce the number of slices by half, whilst having the benefit of reducing the number of total phase encoding steps, hence a lessened influence on the decay of the hyperpolarised state, when compared to a sequence with the same resolution and current number of slices. A reduction in the TR by up to a third is possible, as suggested by the parameter simulations, doing so, coupled with the reduced number of slices will allow for a reasonable temporal resolution to be maintained. The change of further spectral parameters, such as ΔTE will allow for more echoes to be acquired during a singular TR, affording a gain in signal which may offset the loss in SNR incurred by a reduced voxel volume.

Further work, in the form of simulations and phantom work is required to quantify whether these proposed changes can offset the issues generated by having a finer spatial resolution.

Clinical application

Hyperpolarised ^{13}C-MR is an imaging modality with great potential. Metabolic imaging of other abdominal tumour types such as renal and liver cancer is already possible with the ME-bSSFP sequence, as shown when used in conjunction with a surface coil during the PPGL study (Chapter 6). For other cancers, such as brain and breast the sequence will need to undergo further optimisation as the range of spectral parameters available will vary with limitations in spatial resolution imposed by coil-specific sensitivity profiles.

Imaging of other metabolites such as fumarate for the purposes of tissue necrosis will be possible soon; preclinical work has already been demonstrated, with toxicology studies ongoing [106], [107].

Section E

References

[1] S. J. Nelson *et al.*, “Metabolic Imaging of Patients with Prostate Cancer Using Hyperpolarized [1-13C] Pyruvate,” *Sci. Transl. Med.*, vol. 5, no. 198, pp. 198, 2013.

[2] O. Abeyakoon *et al.*, “ Hyperpolarised 13C MRI: a new horizon for non-invasive diagnosis of aggressive breast cancer,” *BJR|case reports*, vol. 5, no. 3, p. 20190026, 2019.

[3] J. Kurhanewicz *et al.*, “Analysis of cancer metabolism by imaging hyperpolarized nuclei: prospects for translation to clinical research.,” *Neoplasia*, vol. 13, no. 2, pp. 81–97, 2011.

[4] M. J. Albers, “Hyperpolarized 13C lactate, pyruvate, and alanine: noninvasive biomarkers for prostate cancer detection and grading,” *Cancer Res.*, vol. 68, no. 20, pp. 8607–8615, 2008.

[5] F. Gallagher, “Magnetic resonance imaging of pH in vivo using hyperpolarized 13C-labelled bicarbonate,” *Nature*, vol. 453, no. 7197, p. 940, 2008.

[6] A. Bornet, “Boosting dissolution dynamic nuclear polarization by cross polarization,” *J. Phys. Chem. Lett.*, vol. 4, no. 1, pp. 111–114, 2012.

[7] T. Theis, “Direct and cost-efficient hyperpolarization of long-lived nuclear spin states on universal 15N2-diazirine molecular tags,” *Sci. Adv.*, vol. 2, no. 3, pp. e1501438, 2016.

[8] R. Malinowski, “Dissolution Dynamic Nuclear Polarization capability study with fluid path,” *J. Magn. Reson.*, vol. 272, pp. 141–146, 2016.

[9] M. L. Truong, A. M. Coffey, R. V. Shchepin, K. W. Waddell, and E. Y. Chekmenev, “Sub-second proton imaging of 13C hyperpolarized contrast agents in water,” *Contrast Media Mol. Imaging*, vol. 9, no. 5, pp. 333–341, 2014.

[10] F. Reineri, T. Boi, and S. Aime, “ParaHydrogen Induced

Polarization of 13C carboxylate resonance in acetate and pyruvate," *Nat. Commun.*, vol. 6, p. 5858, Jan. 2015.

[11] K. Golman, R. Zandt, and M. Thaning, "Real-time metabolic imaging," *Proc. Natl. Acad. Sci. U.S.A.*, vol. 103, no. 30, pp. 11270–11275, 2006.

[12] E. Cavallari, C. Carrera, T. Boi, S. Aime, and F. Reineri, "Effects of Magnetic Field Cycle on the Polarization Transfer from Parahydrogen to Heteronuclei through Long-Range J-Couplings," *J. Phys. Chem,* vol 119, no. 31, pp. 10035-10041, 2015.

[13] P. Bhattacharya, "Towards hyperpolarized 13C-succinate imaging of brain cancer," *J. Magn. Reson. Imaging*, vol. 186, no. 1, pp. 150–155, 2007.

[14] N. M. Zacharias, "Towards Real-time Metabolic Profiling of Cancer with Hyperpolarized Succinate," *J. Mol. Imaging Dyn.*, vol. 6, no. 1, 2016.

[15] O. G. Salnikov *et al.*, " Parahydrogen-Induced Polarization of 1-13C-Acetates and 1-13C-Pyruvates Using Side-Arm Hydrogenation of Vinyl, Allyl and Propargyl Esters ," *J. Phys. Chem. C*, vol. 123, pp. 12827–12840, 2019.

[16] R. V. Shchepin, "Efficient Synthesis of Molecular Precursors for Para-Hydrogen-Induced Polarization of Ethyl Acetate-1-13C and Beyond," *Angew. Chemie*, vol. 128, no. 20, pp. 6175–6178, 2016.

[17] K. Kovtunov, "Hyperpolarized NMR: d-DNP, PHIP, and SABRE," *Chem. - An Asian J.*, vol. 13, no. 15, pp. 1857-1871, 2018.

[18] A. B. Schmidt *et al.*, "Liquid-state carbon-13 hyperpolarization generated in an MRI system for fast imaging," *Nat. Commun.*, vol. 8, no. 1, pp. 14535, 2017.

[19] J. Agraz, "LabVIEW-based control software for para-hydrogen induced polarization instrumentation," *Rev. Sci. Instrum.*, vol. 85, no. 4, 2014.

[20] M. Goldman, "Hyperpolarization of 13C through order transfer from parahydrogen: a new contrast agent for MRI," *Magn.*

Reson. Imaging, vol. 23, no. 2, pp. 153–157, 2005.

[21] R. Adams, “A theoretical basis for spontaneous polarization transfer in non-hydrogenative para hydrogen-induced polarization,” *J. Chem. Phys.*, vol. 131, no. 19, 2009.

[22] K. Atkinson, “Para-hydrogen induced polarization without incorporation of para-hydrogen into the analyte,” *Inorganic Chem.*, vol. 48, no. 2, pp. 663–670, 2008.

[23] D. Barskiy, “The absence of quadrupolar nuclei facilitates efficient 13C hyperpolarization via reversible exchange with parahydrogen,” *Chem. Phys. Chem.*, vol. 18, no. 12, pp. 1493–1498, 2017.

[24] M. Truong, “15N hyperpolarization by reversible exchange using SABRE-SHEATH,” *J. Phys. Chem. C*, vol. 119, no. 16, pp. 8786–8797, 2015.

[25] Z. Zhou, “Long-lived 13C2 nuclear spin states hyperpolarized by parahydrogen in reversible exchange at microtesla fields,” *J. Phys. Chem. Lett.*, vol. 8, no. 13, pp. 3008–3014, 2017.

[26] D. Barskiy, “Over 20% 15N hyperpolarization in under one minute for metronidazole, an antibiotic and hypoxia probe,” *J. Am. Chem. Soc.*, vol. 138, no. 26, pp. 8080–8083, 2016.

[27] P. Rayner, “Delivering strong 1H nuclear hyperpolarization levels and long magnetic lifetimes through signal amplification by reversible exchange,” *Natl. Acad. Sci.*, vol. 114, no. 16, pp. 3188-3194, 2017.

[28] J. Hovener, “Quality assurance of PASADENA hyperpolarization for 13C biomolecules,” *Magn. Reson. Mater. Physics, Biol. Med.*, vol. 22, no. 2, pp. 123–134, 2009.

[29] G. Norquay, G. Collier, and M. Rao, “Xe-Rb Spin-Exchange Optical Pumping with High Photon Efficiency,” vol. 121, no. 15, pp. 153201, 2018.

[30] G. J. Collier, G. Norquay, R. F. Schulte, M. Rao, J. Ball, and J. M. Wild, “Imaging gas-exchange lung function and brain tissue uptake of hyperpolarized 129Xe using sampling density-weighted MRSI,” *Magn. Reson. Med.*, vol. 89, no. 6, pp. 2217-26, 2023.

[31] J. T. Grist *et al.*, “Lung Abnormalities Detected with Hyperpolarized Xe MRI in Patients with Long COVID,” *Radiology.*, vol. 35, no. 3, pp. 709-717, 2022.

[32] E. Milshteyn, C. von Morze, J. W. Gordon, Z. Zhu, P. E. Z. Larson, and D. B. Vigneron, “High spatiotemporal resolution bSSFP imaging of hyperpolarized [1-13C] pyruvate and [1-13C] lactate with spectral suppression of alanine and pyruvate-hydrate,” *Magn. Reson. Med.*, vol. 80, no. 3, pp. 1048–1060, 2018.

[33] T. B. Rodrigues, E. M. Serrao, B. W. C. Kennedy, D. Hu, M. I. Kettunen, and K. M. Brindle, “Technical Reports Magnetic resonance imaging of tumor glycolysis using hyperpolarized 13C-labelled glucose,” vol. 20, no. 1, pp. 93–98, 2014.

[34] R. Sriram *et al.*, “Molecular detection of inflammation in cell models using hyperpolarized 13C-pyruvate,” *Theranostics*, vol. 8, no. 12, pp. 3400–3407, 2018.

[35] M. Van Criekinge *et al.*, “Translation of Carbon-13 EPI for hyperpolarized MR molecular imaging of prostate and brain cancer patients,” *Magn. Reson. Med.,* vol. 81, no. 4, pp. 2702–2709, 2019.

[36] M. Tran and A. Latifoltojar, “tumoral metabolic heterogeneity in renal cell carcinoma,” *Br. J. Radiol.*, vol. 5, no. 3, pp. 20190003, 2019.

[37] S. Siddiqui *et al.*, “The use of hyperpolarized carbon-13 magnetic resonance for molecular imaging,” *Adv. Drug Deliv. Rev.*, vol. 113, pp. 3–23, 2017.

[38] M. S. Ramirez *et al.*, “Radial Spectroscopic MRI of Hyperpolarized [1-13C] Pyruvate at 7 Tesla.”, *Magn. Reson. Med.,* vol. 72, no. 4, pp. 986-995, 2014

[39] H. Y. Chen *et al.*, “Technique development of 3D dynamic CS-EPSI for hyperpolarized 13C pyruvate MR molecular imaging of human prostate cancer,” *Magn. Reson. Med.*, vol. 80, no. 5, pp. 2062–2072, 2018.

[40] W. T. Dixon, “Simple proton spectroscopic imaging,” *Radiology*, vol. 153, no. 1, pp. 189–194, 1984.

[41] J. Leupold, S. Månsson, J. Stefan Petersson, J. Hennig, and O. Wieben, “Fast multiecho balanced SSFP metabolite mapping of 1H and hyperpolarized 13C compounds,” *Magn. Reson. Mater. Physics, Biol. Med.*, vol. 22, no. 4, pp. 251–256, 2009.

[42] P. Peterson, “Fat quantification using multiecho sequences with bipolar gradients: investigation of accuracy and noise performance.,” *Magn. Reson. Med.*, vol. 71, no. 1, pp. 219–229, 2014.

[43] O. Wieben and J. Leupold, “Multi-Echo balanced SSFP Imaging for Iterative Dixon Reconstruction,” *Proc. Intl. Soc. Mag. Reson. Med. 13*, vol. 13, p. 2386, 2005.

[44] C. A. Müller *et al.*, “Dynamic 2D and 3D mapping of hyperpolarized pyruvate to lactate conversion in vivo with efficient multi-echo balanced steady-state free precession at 3 T,” *NMR in Biomedicine,* vol. 33, no. 6, pp. e4291, 2020.

[45] W. H. Perman *et al.*, “Fast volumetric spatial-spectral MR imaging of hyperpolarized C-labeled compounds using multiple echo 3D bSSFP,” *Magn. Reson. Imaging*, vol. 28, no. 4, pp. 459–465, 2010.

[46] K. Scheffler, “On the transient phase of balanced SSFP sequences,” *Magn. Reson. Med.*, vol. 49, no. 4, pp. 781–783, 2003.

[47] C. J. Daniels *et al.*, “A comparison of quantitative methods for clinical imaging with hyperpolarized 13C-pyruvate,” *NMR Biomed.*, vol. 29, no. 4, pp. 387–399, 2016.

[48] D. K. Hill *et al.*, “Model Free Approach to Kinetic Analysis of Real-Time Hyperpolarized 13C-Magnetic Resonance Spectroscopy Data,” vol. 8, no. 9, pp. 1–9, 2013.

[49] K. L. Granlund, S. Tee, H. A. Vargas, F. Robb, H. Hricak, and K. R. Keshari, “Clinical and Translational Report Hyperpolarized MRI of Human Prostate Cancer Reveals Increased Lactate with Tumor Grade Driven by Monocarboxylate Transporter 1,” *Cell Metab.*, vol. 31, no. 1, pp. 105-114, 2020.

[50] P. E. Z. Larson *et al.*, “Investigation of analysis methods for hyperpolarized 13C-pyruvate metabolic MRI in prostate cancer

patients," *NMR in Biomedicine,* vol. 31, no. 11, pp. e3997, 2018.

[51] G. Varma *et al.*, "Selective spectroscopic imaging of hyperpolarized pyruvate and its metabolites using a single-echo variable phase advance method in balanced SSFP," *Magn. Reson. Med.*, vol. 76, no. 4, pp. 1102–1115, 2016.

[52] K. E. Keenan *et al.*, "Quantitative Magnetic Resonance Imaging Phantoms : A Review and the Need for a System Phantom," vol. 79, no. 1, pp. 48–61, 2018.

[53] C. M. Walker, J. Lee, M. S. Ramirez, D. Schellingerhout, S. Millward, and J. A. Bankson, "A Catalyzing Phantom for Reproducible Dynamic Conversion of Hyperpolarized [1-13C]-Pyruvate," *PLoS One*, vol. 8, no. 8, p. e71274, Aug. 2013.

[54] C. M. Walker, M. Merritt, J.-X. Wang, and J. A. Bankson, "Use of a Multi-compartment Dynamic Single Enzyme Phantom for Studies of Hyperpolarized Magnetic Resonance Agents," *J. Vis. Exp.*, no. 110, pp. 1–7, 2016.

[55] R. Chowdhury, M.-V. Papoutsaki, C. A. Müller, and L. Smith, "A reproducible dynamic phantom for sequence testing in hyperpolarised 13 C-magnetic resonance," *The British J. of Rad.,* vol. 95, no. 1134, pp. 20210770, 2022.

[56] C. Chen, Y. Wan, Y. Wai, and H. Liu, "Quality Assurance of Clinical MRI Scanners Using ACR MRI Phantom: Preliminary Results," *J. Digit. Imaging*, vol. 17, no. 4, p. 279-284, 2004.

[57] J. X. Wang, M. E. Merritt, A. D. Sherry, and C. R. Malloy, "Accelerated chemical shift imaging of hyperpolarized 13C metabolites," *Magn. Reson. Med.*, vol. 76, no. 4, pp. 1033–1038, 2016.

[58] Y. Feng *et al.*, "Development and testing of hyperpolarized 13C MR calibrationless parallel imaging," *J. Magn. Reson.*, vol. 262, pp. 1–7, 2016.

[59] J. Y. C. Lau, B. J. Geraghty, A. P. Chen, and C. H. Cunningham, "Improved tolerance to off-resonance in spectral-spatial EPI of hyperpolarized [1-13C]pyruvate and metabolites," *Magn. Reson. Med.*, vol. 80, no. 3, pp. 925–934, 2018.

[60] J. Leupold, Mansson Sven, S. Petersson, and J. Hennig, "Fast

multiecho balanced SSFP metabolite mapping of 1H and hyperpolarized 13C compounds," *Magn. Reson. Mater. Physics, Biol. Med.*, vol. 22, no. 4, pp. 251–256, 2009.

[61] J. Wang, A. J. Wright, D. E. Hu, R. Hesketh, and K. M. Brindle, "Single shot three-dimensional pulse sequence for hyperpolarized 13C MRI," *Magn. Reson. Med.*, vol. 77, no. 2, pp. 740–752, 2017.

[62] H. Chen, "Technique development of 3D dynamic CS-EPSI for hyperpolarized 13C pyruvate MR molecular imaging of human prostate cancer," *Magn. Reson. Med.*, vol. 80, no. 5, pp. 2062–2072, 2018.

[63] N. Bøgh *et al.*, "Initial Experience on Hyperpolarized [1-13 C] Pyruvate MRI Multicenter Reproducibility — Are Multicenter Trials Feasible?," *Tomography,* vol. 8, no. 2, pp. 585–595, 2022.

[64] E. Joe *et al.*, "An indirect method for in vivo T2 mapping of [1-13C] pyruvate using hyperpolarized 13C CSI," *NMR Biomed.*, vol. 30, no. 5, pp. 1–8, 2017.

[65] R. Chowdhury *et al.*, "Quantification of Prostate Cancer Metabolism Using 3D Multiecho bSSFP and Hyperpolarized [1-13C] Pyruvate : Metabolism Differs Between Tumors of the Same Gleason Grade," *J. Magn. Res. Im.,* vol. 57, no. 6, pp. 1865-1875, 2022.

[66] B. J. Geraghty, J. Y. C. Lau, A. P. Chen, and C. H. Cunningham, "Dual-Echo EPI sequence for integrated distortion correction in 3D time-resolved hyperpolarized 13C-MRI," *Magn. Reson. Med.*, vol. 79, no. 2, pp. 643–653, 2018.

[67] C. Hundshammer, "Multimodal and Non-Invasive Imaging Techniques for a Multiparametric Characterization of Tumor Biology," 2019.

[68] C. N. Wiens, L. J. Friesen-Waldner, T. P. Wade, K. J. Sinclair, and C. A. McKenzie, "Chemical shift encoded imaging of hyperpolarized 13C pyruvate," *Magn. Reson. Med.*, vol. 74, no. 6, pp. 1682–1689, 2015.

[69] P. W. Kuchel and G. Page, "FmRa Analysis : Rapid and Direct Estimation of Relaxation and Kinetic Parameters from Dynamic

Nuclear Polarization Time Courses," vol. 2080, pp. 2075–2080, 2015.

[70] G. Farkash, S. Markovic, M. Novakovic, and L. Frydman, "Enhanced hyperpolarized chemical shift imaging based on a priori segmented information," *Magn. Reson. Med.*, vol. 81, no. 5, pp. 3080–3093, 2019.

[71] A. Bornet, X. Ji, D. Mammoli, B. Vuichoud, and J. Milani, "Long-Lived States of Magnetically Equivalent Spins Populated by Dissolution-DNP and Revealed by Enzymatic Reactions", *Chem. A Eur. J.,* vol. 20, no. 51, pp. 17113–17118, 2014.

[72] F. A. Gallagher, M. I. Kettunen, and K. M. Brindle, "Imaging pH with hyperpolarized 13C," *NMR Biomed.*, vol. 24, no. 8, pp. 1006–1015, 2011.

[73] S. Düwel *et al.*, "Imaging of pH in vivo using hyperpolarized 13C-labelled zymonic acid," *Nat. Commun.*, vol. 8, no. 1, pp. 15126, 2017.

[74] J. Steinhauser, P. Wespi, G. Kwiatkowski, and S. Kozerke, "Production of highly polarized [1-13C] acetate by rapid decarboxylation of [2-13C] pyruvate – application to hyperpolarized cardiac spectroscopy and imaging," *Magn. Reson. Med.*, vol. 82, no. 3, pp. 1140-1149, 2019.

[75] N. E. M. Association, "NEMA Standards Publication MS 3-2008, Determination of Image Uniformity in Diagnostic Magnetic Resonance Images," vol. 2008, pp. 1–17, 2008.

[76] R. Price *et al.*, "Quality assurance methods and phantoms for magnetic resonance imaging: Report of AAPM nuclear magnetic resonance Task Group No. 1," *Med. Phys.*, vol. 17, no. 2, pp. 287–295, 1990.

[77] D. J. Drost, W. R. Riddle, and G. D. Clarke, "Proton magnetic resonance spectroscopy in the brain : Report of AAPM MR Task Group # 9,", *Med. Phys.,* vol. 29, no. 9, pp. 2177–2197, 2002.

[78] C. M. Walker, "Novel Simulation to Avoid Bias in Measurement of Hyperpolarized Pyruvate : Demonstrated in Phantom and In Vivo,", 2016.

[79] K. L. Granlund *et al.*, "Hyperpolarized MRI of Human Prostate

Cancer Reveals Increased Lactate with Tumor Grade Driven by Monocarboxylate Transporter 1," *Cell Metab.*, vol. 31, no. 1, pp. 105-114.e3, 2020.

[80] O. Abeyakoon, A. Latifoltojar, F. Gong, M.-V. Papoutsaki, and R. Chowdhury, "Hyperpolarised 13 C MRI : a new horizon for non-invasive diagnosis of aggressive breast cancer," *BJR| case reports,* vol. 5,no. 3, pp. 20190026, 2019.

[81] J. W. Gordon, H. Chen, N. Dwork, S. Tang, and P. E. Z. Larson, "Fast Imaging for Hyperpolarized MR Metabolic Imaging,", *J. Magn. Res. Im.,* vol. 53, no. 3, pp. 686-702, 2020.

[82] J. W. Gordon, D. B. Vigneron, and P. E. Z. Larson, "Development of a symmetric echo planar imaging framework for clinical translation of rapid dynamic hyperpolarized 13C imaging," *Magn. Reson. Med.*, vol. 77, no. 2, pp. 826–832, 2017.

[83] H. Shang *et al.*, "Spectrally selective three-dimensional dynamic balanced steady-state free precession for hyperpolarized C-13 metabolic imaging with spectrally selective radiofrequency pulses," *Magn. Reson. Med.*, vol. 78, no. 3, pp. 963–975, 2017.

[84] O. Bieri and K. Scheffler, "Fundamentals of balanced steady state free precession MRI," *J. Magn. Reson. Imaging*, vol. 38, no. 1, pp. 2–11, 2013.

[85] J. Leupold *et al.*, "Fast chemical shift mapping with multiecho balanced SSFP," *Magn. Reson. Mater. Physics, Biol. Med.*, vol. 19, no. 5, pp. 267–273, 2006.

[86] J. R. Yamashiro and W. T. W. De Riese, "Any Correlation Between Prostate Volume and Incidence of Prostate Cancer : A Review of Reported Data for the Last Thirty Yearss,", *Res.. Rep. Urology,* pp. 749-757 2021.

[87] S. E. Moyher, D. B. Vigneron, and S. J. Nelson, "Surface Coil MR imaging of the human brain with an analytic reception profile correction" *J. Magn. Reson. Imaging*, vol. 140, pp. 139–144, 1995.

[88] K. Scheffler and J. Hennig, "Is TrueFISP a gradient-echo or a spin-echo sequence?," *Magn. Reson. Med.*, vol. 49, no. 2, pp. 395–397, 2003.

[89] S. M. Noworolski, G. D. Reed, J. Kurhanewicz, and D. B. Vigneron, “Post-Processing Correction of the Endorectal Coil Reception Effects in MR Spectroscopic Imaging of the Prostate,” *J. Magn. Res. Im.*, vol. 32, no. 3, pp. 654–662, 2010.

[90] J. C. Baez *et al.*, “Pheochromocytoma and paraganglioma: Imaging characteristics,” *Cancer Imaging*, vol. 12, no. 1, pp. 153–162, 2012.

[91] R. Alrezk, A. Suarez, I. Tena, and K. Pacak, “Update of Pheochromocytoma Syndromes: Genetics, Biochemical Evaluation, and Imaging”, *Front. Endocrinol. (Lausanne).,* vol. 9, pp. 515, 2018.

[92] Y. Yamazaki *et al.*, “Recent Advances in Histopathological and Molecular Diagnosis in Pheochromocytoma and Paraganglioma: Challenges for Predicting Metastasis in Individual Patients,” *Front. Endocrinol. (Lausanne).*, vol. 11, no. October, pp. 1–11, 2020.

[93] H. Lim, K. Thind, F. M. Martinez-Santiesteban, and T. J. Scholl, “Construction and evaluation of a switch-tuned 13C - 1H birdcage radiofrequency coil for imaging the metabolism of hyperpolarized 13C-enriched compounds,” *J. Magn. Reson. Imaging*, vol. 40, no. 5, pp. 1082–1090, 2014.

[94] H. Yu, S. B. Reeder, A. Shimakawa, J. H. Brittain, and N. J. Pelc, “Field map estimation with a region growing scheme for iterative 3-point water-fat decomposition,” *Magn. Reson. Med.*, vol. 54, no. 4, pp. 1032–1039, 2005.

[95] E. Panagiotidis *et al.*, “Comparison of the Impact of 68Ga-DOTATATE and 18F-FDG PET/CT on Clinical Management in Patients with Neuroendocrine Tumors,” *J. Nuc. Med.*, vol. 58, no. 1, pp. 91–96, 2017.

[96] V. Rufini, G. Treglia, G. Perotti, and A. Giordano, “The evolution in the use of MIBG scintigraphy in pheochromocytomas and paragangliomas”, *Hormones,* vol. 12, no. 1, pp. 58–68, 2013.

[97] O. Warburg, “Injuring of Respiration the Origin of Cancer Cells”, *Science,* vol. 123, no. 3191, pp. 309-314, 1956.

[98] K. Eijkelenkamp, T. E. Osinga, T. P. Links, and A. N. A. van der

Horst-Schrivers, “Clinical implications of the oncometabolite succinate in SDHx-mutation carriers,” *Clin. Genet.*, vol. 97, no. 1, pp. 39–53, 2020.

[99] J. L. Coloff *et al.*, “Differential Glutamate Metabolism in Proliferating and Quiescent Mammary Epithelial Cells Article,” *Cell Metab.*, vol. 23, no. 5, pp. 867–880, 2016.

[100] L. V. Bel’skaya, E. A. Sarf, and V. K. Kosenok, “Age and gender characteristics of the biochemical composition of saliva: Correlations with the composition of blood plasma,” *J. Oral Biol. Craniofacial Res.*, vol. 10, no. 2, pp. 59–65, 2020.

[101] V. Pallotta, A. D. Alessandro, S. Rinalducci, and L. Zolla, “Native Protein Complexes in the Cytoplasm of Red Blood Cells,” *J. Proteome Res.,* vol. 12, no. 7, pp. 3529-46, 2013.

[102] I. J. Sullivan and J. N. Faulds, “Lactate dehydrogenase and Haemolysis Index as quality control markers of haemolysis in intra-operative cell salvage,” *Transfus. Med.*, vol. 23, no. 5, pp. 326–329, 2013.

[103] W. M. Cassidy and T. B. Reynolds, “Serum lactic dehydrogenase in the differential diagnosis of acute hepatocellular injury,” *J. Clin. Gastroenterol.*, vol. 19, no. 2, pp. 1128–121, 1994.

[104] P. Wespi, J. Steinhauser, G. Kwiatkowski, and S. Kozerke, “Overestimation of cardiac lactate production caused by liver metabolism of hyperpolarized [1-13C] pyruvate,” *Magn. Reson. Med.*, vol. 80, no. 5, pp. 1882–1890, 2018.

[105] S. M. Noworolski, G. D. Reed, J. Kurhanewicz, and B. Vigneron, “NIH Public Access,” vol. 32, no. 3, pp. 654–662, 2010.

[106] M. Singh, S. Josan, M. Zhu, A. Jhajharia, and D. Mayer, “Dynamic metabolic imaging of copolarized [2-13C] pyruvate and [1,4-13C2] fumarate using 3D-spiral CSI with alternate spectral band excitation,” *Magn. Reson. Med.*, vol. 81, no. 5, pp. 2869–2877, 2019.

[107] A. Eldirdiri, A. Clemmensen, S. Bowen, A. Kjær, and J. H. Ardenkjær-Larsen, “Simultaneous imaging of hyperpolarized [1,4-13C2] fumarate, [1-13C] pyruvate and 18F–FDG in a rat

model of necrosis in a clinical PET/MR scanner," *NMR Biomed.*, vol. 30, no. 12, pp. 1–9, 2017.

[108] S. B. Reeder *et al.*, "Multicoil Dixon Chemical Species Separation with an Iterative Least-Squares Estimation Method," *Magn. Reson. Med.*, vol. 51, no. 1, pp. 35–45, 2004.

Appendix

Appendix A: Research Fluid Path Preparation

Dose concentration (mM)	250	Approx. 250	80
Dose volume (ml)	57	22.9	18.5
Dissolution media in syringe (g)	40	18	18
Length of outer lumen tube removed (mm)	15.0	0.5ml dose	29.5
Acid/radical in sample vial (g)	1.28	0.422	0.135
Neutralisation media in receiver (g)	14.4	6.466	2.069
Dilution media in receiver (g)	9.8	5.961	5.961
Fluid path dead volume (g)	8	10	10
Neutralisation media composition	720mM NaOH/400mM TRIS	720mM NaOH/400mM TRIS	720mM NaOH/400mM TRIS

Table A 1 – Formulations for preparing different concentrations of hyperpolarised [1-^{13}C] pyruvate using the research fluid paths described later in this Appendix.

1. Flow and moisture check

1.1. Open the filling station Helium valve opposite hyperpolariser and set regulator pressure to 15 PSI and test

gas flow at the filling station (briefly turn on and off). User should be able to hear gas flowing.

1.2. Fully push dissolution syringe onto pressure check fixture.

N.B. Part A tubing should still have protective/storage sleeve attached, B1.4/B1.5 will not be possible without this. Pushing the syringe onto the fixture at an angle may result in damage to the fixture o-rings. Check o-rings on pressure check fixture before attaching dissolution syringe. If there are any holes/scratches/dents on the o-rings, they will need replacing.

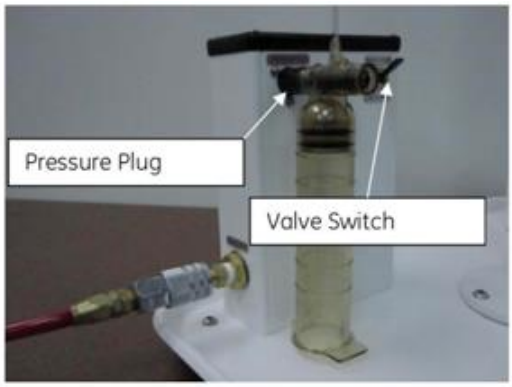

Figure 3: Dissolution Syringe Connected to Pressure Checker

1.3. Hang tubing on support apparatus.

N.B. Not securing the tubing properly may cause it to flail uncontrollably.

1.4. Flow gas through system (toggle valve switch to DOWN position).

1.5. Confirm gas flow through system by feeling/listening for gas at luer outlet of dissolution syringe.

N.B. If gas flow cannot be felt there could be three potential issues:

1. The compression seal, attaching the protective sleeve to part A is not tight enough or too tight. Refer to section 7 for how to correctly assemble the compression seal. If the sleeve is too tight the upper portion of the protective sleeve will appear deformed/squeezed; trim this with a razor blade (as shown in section 3) and replace the ferrule (as shown in section 7).

2. The filling station may be leaking. Attach the test dissolution syringe (shown right) and cap the luer lock. Fill the system for 30 seconds by opening the valve switch to the DOWN position. Proceed to close the valve switch by toggling it to the UP position. Upon closing the valve observe the pressure for 2 minutes. After this open the valve again by switching to the DOWN position; if the needle on the pressure gauge moves then there is a leak in the filling station. GE will need to be contacted to fix this.

3. If after performing step 1 there is still a leak and in step 2 the pressure remains constant then this means that the RFP is leaking somewhere and will need to be disposed of.

1.6. If moisture is observed, flow gas for at least 10 minutes to ensure the fluid path is dry.

N.B. This is essential, not drying the RFP fully will result in blockages forming when the solution is loaded into the polariser – causing dissolution to fail/the RFP components being forced apart in the polariser.

1.7. Close valve switch (toggle to UP position). A luer lock cap can be fixed to the dissolution syringe to prevent moisture from entering the outlet line.

1.8. A tag can be added to the fluid path at this time to identify the component for future use. Typically, a simple tape label can

be added to the tube existing the dissolution syringe approximately 6” above the valve.

2. Filling dissolution syringe with dissolution media

2.1. Place dissolution syringe onto holder on the assembly.

2.2. Confirm dissolution syringe piston is fully pressed up to empty position (Figure 4).

Figure 4: Syringe On Holder With Piston Up

Figure 5: Filling Syringe

2.3. Hang tubing on support apparatus.

N.B. Not securing the tubing properly may cause it to flail uncontrollably.

2.4. Ensure that the dissolution media filling syringe is connected to the filling plug (Figure 5).

N.B. If the connection between the filling plug and filling syringe appears to be loose, disconnect it from the filling syringe and replace the luer fixture. These can be found in the same packs in which the disposable outer lumens are provided.

N.B. Try to keep the filling plug and syringe as horizontally level as possible so as to avoid damage to the luer lock connecting the two

2.5. Confirm fill plug is primed with dissolution media by drawing a volume (~5mL) into the fill syringe, holding syringe upright to expel any trapped air and disposing of volume in fill syringe.

2.6. Place the filling syringe with plug on balance and zero the balance.

2.7. Fill syringe with 18±0.01g of dissolution media, remove any residual media from the outer surface of the plug and record mass. Media can be added or dispensed from the filling syringe to achieve the correct level.

2.8. Supporting the filling plug and dissolution media filling syringe as seen in Figure 5, insert the filling plug into the dissolution syringe valve bore and dispense contents. Failure to support the filling plug during insertion and removal adds strain to the filling plug luer adaptor and may result in failure of this component.

N.B. When attaching the filling syringe to the dissolution syringe hold the black plug as shown in Figure 5, not doing so will result in stress being applied to the luer connecting the filling plug to the filling syringe, potentially leading to it breaking. If the connecting between the filling plug and filling syringe appears to be loose, disconnect it from the filling syringe and replace the luer fixture. These can be found in the same packs in which the disposable outer lumens are provided.

2.9. Remove the filling syringe with plug and wipe the bore – ensure bore is completely dry. When drying the dissolution

syringe bore remove the apparatus from the holder shown in figure 4. Failure to do so may result in liquid entering the tubing.

N.B. If the bore is not completely dry solution may enter the tubing, leading to potential blockages and failure during the dissolution step. Use KimWipes and not regular tissue as the former will not leave any lint, further reducing the likelihood of blockages. Leave a KimWipe in the inner bore.

2.10. Remove the syringe containing pyruvic acid/EPA mixture from the freezer and place into a 50ml beaker filled with 40ml of warm tap water

N.B. Doing this now means that after section 3 has been completed the acid/radical sample will have thawed and the user will not have to wait around for this to occur.

3. Trimming Outer Lumen Tubing

3.1. Reducing the length of the outer tube has the effect of positioning the inner tube deeper into the sample vial. To maintain optimum dissolution efficiency the inner tube should be positioned 5 mm from the frozen sample surface.

3.2. The disposable outer lumen tube as received is the correct size for 2.0mL sample.

3.3. If 0.1mL is to be used, cut tubing to length using tube cutting block (remove 29.5mm).

N.B. For a 0.1ml sample trim the outer lumen using the guide for the 0.5ml sample (Figure 6). This will adequately position the inner tube above the sample.

3.4. Cutting location for associated sample volume shown in Figure 6.

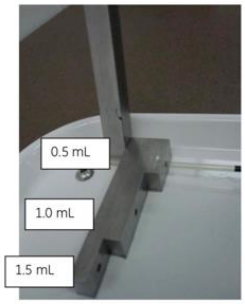

Figure 6: Tube Cutting Sample Size Reference

3.5. Insert tube into cutting block with black marking closest to cutting fixture and ensure that tube is pressed fully into fixture against hinged backstop. Cutting the opposite end of the tube will result in improper positioning of the sample within the polarize and may impact operation.

3.6. Cut tube at cutting block with straight razor (Figure 7). Practice cutting on a test piece of tubing. One procedure that has proven successful and reproducible entails the following: (1) firmly press the tube into the cutting block; (2) place the razor blade in contact with the tube, (3) rotate the tube to score the tube, (4) cut the tube by with a downward and lateral slicing motion of the razor.

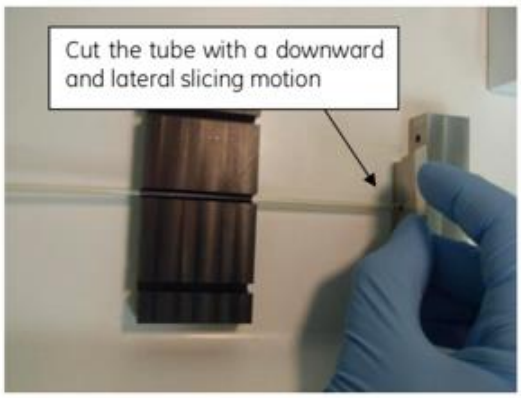

Figure 7: Tube Cutting.

3.7. Remove the cut outer lumen tube and inspect the cut for straightness and debris. Dispose of incorrectly cut tubes and retry with a new/unmodified outer lumen tube. Tubes should not be cut multiple times.

3.8. Open the back stop on cutting fixture and push cut section out for disposal.

4 Load sample into vial

4.1. Switch the benchtop UV source on

N.B. Doing this now will ensure that after the cryovial has been filled and the outer lumen glued (section 4) the user will not have to wait for the UV source (which acts to cure the glue) to warm up.

4.1. Place empty vial with weighing block on balance and zero balance (Figure 8).

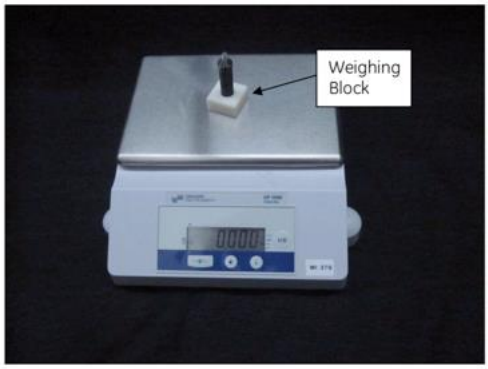

Figure 8: Weigh Vial

4.2. While holding the vial in a vertical orientation, carefully transfer the 0.135g (approx. 0.1ml) of the acid/radical sample into vial using an adjustable pipet. Ensure that the pipet tip does not fully seal the vial port during loading to minimize the likelihood of spilling sample.

4.3. After loading, if sample is present at the tubing port, use Kimwipe or other absorbent media that will not leave particulate behind to carefully and fully wipe all sample from the port.

4.4. Weigh vial for final sample volume.

N.B. It's easier to pipette the acid/radical solution straight into the cryovial whilst it is on the weighing scale. Setting the P200 syringe to 100 will inject 100µl (0.1ml) of solution into the cryovial. The acid/radical solution has a density of 1.35g/ml. Make a note of this value to get an accurate idea of the final concentration of pyruvate produced.

5 Gluing outer lumen to cryovial

5.1. Ensure that the UV source is turned on at least 5 minutes prior to use to allow time for the lamp to warm up. The lamp intensity should be adjusted to apply 2.5 W/cm2 with the waveguide positioned 1 cm from the from the joint surface. The source timer should be set for a 10s exposure.

5.2. Place vial with sample into vial holder (Figure 9).

Figure 9: Vial in Vial Holder

5.3. Apply UV cure adhesive to outside of disposable outer lumen tubing at end furthest from black mark. If too much glue is applied, wipe the glue from the tube and reapply. The glue should be cured immediately using the following steps to minimize the potential for crazing or cracking of the plastic.

N.B. Place a single drop of glue 0.5cm from the end and use the needle tip to spread this around the lumen. The glue is extremely runny and using a single drop ensures that it is easier to spread. Adding the drop at this distance allows the glue to fall around the cryovial evenly in 5.2.

5.4. Slide tubing into slot with the adhesive below the tube holder. Insert tubing with adhesive into vial cap.

5.5. Keep the lumen firmly pressed to cryovial allowing the glue to fill the joint between the two components.

N.B. If the glue appears to have flown within the lumen remove the tube. Wipe the glue away with a Kimwipe, if there is still glue within

the lumen then repeat section 4 with a new outer lumen. Residual glue within the lumen will result in blockages, potentially causing the RFP to blow apart.

5.6. CAUTION: ALWAYS USE PROPER SAFETY PROCEDURES TO PROTECT YOURSELF AND OTHERS FROM ULTRAVIOLET LIGHT, INCLUDING BUT NOT LIMITED TO: UV GOGGLES AND SHIELD TO PROTECT EXTERNAL PERSONNEL AND LOCKING THE LAB DOOR TO PREVENT ACCIDENTAL EXPOSURE

5.7. While holding the tube in position above the vial holder, position the UV source waveguide 1cm from the joint surface and activate the lamp with the pedal. Allow 5s for the initial exposure to cure one side and then slowly rotate the vial 360 degrees to ensure full exposure.

N.B. This step can be repeated up to three times if the glue appears to be visibly runny after the first exposure.

5.8. Inspect the UV glue joint to ensure that it is fully filled.

5.9. Voids in the glue are most easily seen during the UV exposure process, but are also evident with the naked eye following exposure.

5.10. If voids are detected the vial/tube assembly should be replaced by repeat sections **3-5**. The agent can be salvaged from the defective vial by cutting off the tube or vial cap with a razor blade. Salvaged agent can be reused in subsequent experiments.

6. Install Dynamic Seal

6.1. Locate the small black seal insertion tool which is used to avoid damage to seal elements.

6.2. Keep sample vial vertical at all times to avoid sample "splashing" into the attached tube.

6.3. Ensure the vial assembly is firmly positioned within the vial holder.

6.4. Place thin end of the seal insertion tool into end of disposable outer lumen.

6.5. With one finger positioned on top of the dynamic seal, slide the dynamic seal bottom (narrow end) first over the seal insertion tool and onto tubing. Position the seal below the black marking on tube. Use the IV pole to support the top end of the tube/vial assembly.

N.B. When attaching the dynamic seal ensure that the lumen and cryovial are firmly secured. Hold the lumen as close to the top as possible whilst inserting the dynamic seal. This will provide the user with more control and prevent any kinks in the lumen from occurring.

6.6. Remove the seal insertion tool.

7. Connect Disposable Vial Assembly

7.1. With threaded end of nut facing the open end of the tube, place PEEK Nut on disposable outer lumen tube (shown in step 7.3).

7.2. Place a new yellow compression ferrule on disposable outer lumen tube, with conical section of ferrule facing the PEEK Nut. Compression ferrules should not be reused due to alteration in the ferrule's structure during compression. Reuse of a ferrule may compromise the integrity of this connection.

N.B. Ensure that the ferrule is flush with the end of the inner lumen, it is likely to slip/move during the positioning phase prior to screwing. Incorrect positioning could lead to the inner lumen being compressed too much which could result in blockages; subsequently causing the RFP components to fail. Incorrect positioning can also lead to the outer lumen not being firmly secured to the inner lumen causing the

components to blow apart. Have a colleague check that these components are aligned correctly if the user is unsure.

7.3. Insert Inner lumen into disposable outer lumen tube, taking care to avoid kinking the inner lumen tube.

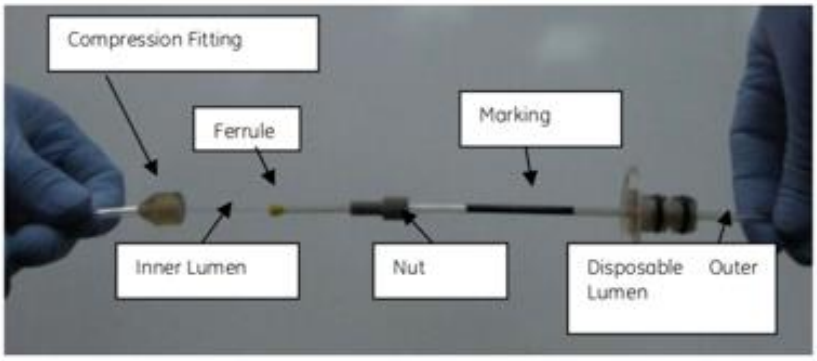

7.4. When the majority of the inner lumen tube is inserted, it may be easier to complete the remaining insertion with the lower section of the outer lumen tube as straight as possible. While supporting the inner lumen at the compression fitting and the entrance to the outer lumen with two hands, remove the tube assembly from the IV pole and reposition your hands with the supported tubes to the left side of the filling tray. This action will straighten the outer lumen tube and enable easier insertion.

7.5. Fully insert end of disposable outer lumen tube into the reusable compression fitting.

7.6. Screw PEEK nut into compression fitting until resistance is felt, signalling that the ferrule is beginning to compress onto the tubing.

N.B. Ensure that the ferrule does not slip off the outer lumen, this often happens and can cause a weakened connection. Apply a small of pressure to the outer lumen, pushing it towards the compression fitting to ensure correct positioning.

7.7. Tighten nut 1⁄4 turn to compress the ferrule. Over tightening the nut will result in continued compression of the outer lumen tube and potentially result in increased flow

resistance. An easy method to ensure a ¼ turn is applied is to line up the thumbs and pointer fingers of your left and right hands as shown in Figure 17. Tightening the fitting will result in the thumb of your right hand being centred between the thumb and pointer finger of your left hand.

7.8. Once this connection is made it should not be undone and remade as the ferrule structure has been altered.

N.B. Loosening of the compression fitting will require that steps 7.3-7.7 be repeated with a new outer lumen and cryovial.

8. Helium Purge and Seal Pressure Check

8.1. Set system pressure to 15 PSI and test gas flow (briefly turn on and off)

N.B. This step is essential to ensure that the RFP tubing becomes as dry as possible. Any moisture in the system will result in a blockage which will cause the system to fail.

8.2. Remove any wipes from the syringe valve bore and fully push dissolution syringe onto pressure check fixture (see below).

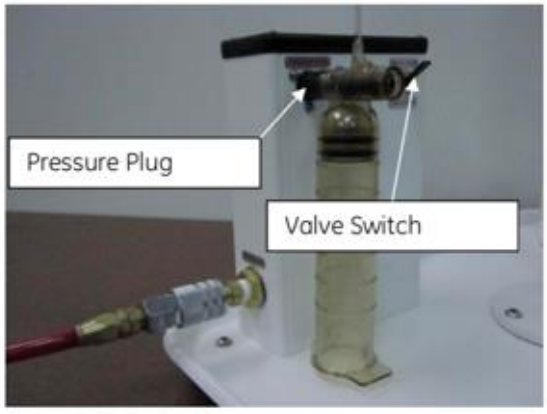

8.3. Cap the dissolution syringe outlet with luer cap. With the pressure check valve in the off position and the luer cap on the dissolution syringe outlet the tube set is effectively sealed. Failure to seal the tube set prior to the following freezing steps may result in the cryogenic pumping of air into the sample vial. The entrapment of air and ambient moisture in the tube set may

result in ice formation when placed in the polarizer, which could lead dissolution failures (limited liquid flow due to tube blockage).

8.4. Holding the sample in a vertical orientation place the vial in liquid nitrogen and freeze. Freezing the sample will prevent splashing during purging and pressure testing. Most sample volumes with be solidified in 1 minute.

N.B. Ensure dynamic seal is as far away from the liquid nitrogen as possible to avoid it being damaged. The vial does not need to be held in the liquid nitrogen, place the cryovial directly in and proceed with the next steps.

8.5. Pressurize the system to 15 PSI. There will be no flow with the syringe outlet capped – allow 2 minutes for the system to pressurise to 15 PSI

N.B. perform a repeat of section 1 if the user suspects that there are leaks. This should not be the case, but it will inform the user if the compression seal is loose.

8.6. Remove luer cap from dissolution syringe outlet and allow helium gas to flow for 5 minutes.

N.B. This will remove all air/moisture from the system

8.7. Confirm gas flow through system by feeling/listening for gas at luer outlet of dissolution syringe.

8.8. Cap the dissolution syringe outlet with luer cap to close the system (shown below).

8.9. Increase pressure at source regulator to 40 psi.

8.10. Close the pressurization valve (toggle switch to UP position).

8.11. Observe pressure gauge for 2 minutes and confirm pressure has not decayed.

N.B. These steps are essentially a repeat of section 1.

8.12. If a pressure loss is noted, there are three likely leak locations. First check that the (1) compression fitting and (2) dissolution syringe outlet ports are tightly fit. If the leak persists the check that the outlet cap is tightly fit. Be careful to avoid over tightening the compression fitting as this action may create a flow restriction.

8.13. If the pressure leak persists a likely cause is the o-rings on the pressure test fixture. Inspection of these o-rings will require the removal and repeat of steps **8.3-8.8**.

8.14. Do not remove syringe from the pressure test fixture before relieving pressure within the fluid path. While pressurized, the process of removing the syringe will align the gas source with the dissolution syringe barrel and result in

pushing the plunger to the bottom of the barrel and the likely loss of fluid.

N.B. Close the helium valve on the filling station (switch valve to UP position) and then remove the luer cap. After doing this then proceed to removed dissolution syringe steps 8.15-8.17.

8.15. Remove the vial from the liquid nitrogen and place in the vial holder. This action reduces the potential for cryogenic pumping when the tube set is opened in the following steps.

8.16. Allow the cryovial to come to room temperature (minimum of 5 minutes). Then slowly open luer cap at syringe outlet to bleed small amount of pressurized gas.

8.17. Remove dissolution syringe from pressure check fixture. Inspect that syringe valve barrel to ensure it is dry. Wipe as needed.

N.B. Ensure that this valve barrel is completely dry. Look at the valve as well, the o-rings need to be undamaged. If there are any visible cuts/scratches/holes on the o-rings, these will need to be replaced as soon as possible. Damaged o-rings will cause the dissolution media to leak from the syringe, immediately, upon the RFP being placed in the polariser.

8.18. Quickly insert valve into the bore of the dissolution syringe and use the valve insertion tool to ensure that the valve is in the closed position (horizontal). The valve can be inserted with or without the insertion tool attached. In both cases, ensure the valve is inserted straight into the valve body. Insertion of the valve at an angle may displace or damage the o-rings, resulting in failures during use with the polarizer. Increased resistance during valve insertion may signify that an o-ring has been dislodged or damaged.

8.19. Allow the sample to thaw before loading into the polariser (Further 5-10 minutes before loading)

N.B. The liquid nitrogen does not result in the acid/radical freezing in an even distribution. For polarisation to occur the acid/radical must

be distributed evenly upon freezing, forming a 'glass'. This will occur most effectively in the polariser.

8.20. When manipulating a thawed sample, ensure the vial is maintained in a vertical orientation to keep the sample from splashing.

N.B. If the acid/radical splashes into the tubing the RFP will need to be disassembled and the user will need to repeat sections 3-this point again.

8.23. At this point the fluid path is loaded and ready for use. Ensure a transfer tube is attached to the dissolution syringe outlet port prior to insertion into the polarizer.

9. Preparation of a Receiver Vessel

9.1. Position the empty receiver vessel (50ml beaker) with parafilm applied over the top on the balance and record the mass. This information is useful when combined with the mass of the dissolution product to calculate the fluid path dead volume.

9.2. Remove the receiver vessel closure and zero the balance.

9.3. Dispense the required amount of neutralization media into the receiver vessel using a disposable pipet.

N.B. The neutralisation media contains a strong base, getting this mass as accurate is essential as it will induce react with the pyruvic acid coming out of the polariser forming pyruvate. If not enough/too much neutralisation media is present then not enough pyruvate will form (the pyruvic acid in the dissolution media has a different chemical shift in ppm then pyruvate).

9.4. Record the final mass and zero the balance.

9.5. Dispense the required volume of dilution media into the receiver vessel using a disposable pipet.

9.6. Record the final mass and zero the balance.

9.7. Seal the receiver vessel with the closure.

9.8. Secure receiver vessel to a larger container, in case of spillage, filled with ice.

N.B. Only add the ice to the larger container five minutes before dissolution. Adding it too early will cause it to melt.

10. Load Fluid Path

10.1. Take RFP to spinlab, again ensuring that the sample vial remains upright, identify a channel to load and select 'Load without QC'

10.2. Open the spinlab door

10.3. Select the 'unlock syringe door' button and load the syringe

10.4. Then select the 'load vial' button and load vial

10.5. Once vial is loaded before closing the spinlab door ensure that plug is 'verified'

10.6. Syringe will be automatically heated, this needs to be switched off – go to > Service > channel_xx > heater pressure > drop down menu > Evt_Cool

10.7. After this, the sample space will be purged of any air – wait for the purging to be complete before switching on the Helium valve – KMC-> app_sm-> channelX_sm-> PurgeController -> He valve (set once).

10.8. Press 'Lower Vial' to begin lowering the sample into the hyperpolariser, this typically takes 20 minutes.

10.9. Once vial has successfully lowered, the 'Cold Ops' button will be active. Press the button to initiate the polarisation. This step is not required if a vial is already loaded and polarising.

10.10. Once polarisation is achieved and receiver beaker from step 9 in in position, press 'Prepare to Dissolute', followed by 'Dissolute' to eject the sample into the receiver vessel.

10.11. The resulting solution is now ready for experimental use.

11. Unload fluid path

11.1. The fluid path cannot be unloaded until the heater has cooled. Wait for the ‘Unload’ button on the relevant channel to become active.

11.2 Press ‘Unload’ and open the SPINLab door.

11.3 Press ‘Open syringe door’ and carefully remove the dissolution syringe from the heater. Close the syringe door.

11.4 Press ‘Unlock Insertion Latch’ and pull back the black handle on the sample channel to access the vial. Carefully pull the vial out and replace the plug.

11.5 Press ‘Verify Vial Unloaded’

12. Clean fluid path

12.1. Put 60ml of water in the filling syringe and mount the fluid path on the filling station and tape the exit line to a sink

12.2. Remove the valve from the barrel of the dissolution syringe and wipe the inside carefully removing any moisture

12.3. Fill the dissolution syringe with water via the filling syringe

12.4. Upon removing the filling syringe wipe the inside of the barrel and reinsert a dried valve

12.5. Turn the valve to the open position

12.6. Force the syringe down on the holder – we should feel a notable amount of pressure here but will also see the water rinsing the fluid path

12.7. Repeat steps 12.1 – 12.6 two more times. During the final run add 10ml of neutralisation media to the water and then proceed with the rinsing process

12.8. Remove the valve from the dissolution syringe and wipe the barrel dry.

12.9. Mount the syringe to the pressure check fixture and switch this on – allow this to run for at least 5 minutes

12.10. Remove part C from dissolution syringe and pack this away.

12.11. Leave research fluid path on the pressure check fixture with the helium running at least 10 minutes

12.12. Disconnect disposable part B from the dissolution syringe and reconnect protective sheath

12.13. Remove dynamic seal from part B and keep this – dispose of the rest of part B

12.14. Pack the sheathed dissolution syringe into one of the storage tubes

Appendix B: IDEAL Model

Metabolite maps were created from bipolar multi-echo (ME) data using iterative decomposition with echo asymmetries and least squares estimation (IDEAL). The theory and algorithm are originally described in *Reeder et al. 2004* with additional correction for bipolar echo effects as described in *Peterson 2013* and adapted for the separation of ^{13}C metabolites in our application [42], [108]. The explanation below assumes that four (x) metabolite frequencies (Δf_x) are being resolved. On a voxel-by-voxel basis, the following signal model was assumed throughout all exams:

$$\boldsymbol{S} = \boldsymbol{E} \cdot \boldsymbol{D} \cdot \boldsymbol{A} \cdot \boldsymbol{P}$$

$$\boldsymbol{S}_{7\times1} = \begin{bmatrix} S(t_1) \\ \vdots \\ S(t_7) \end{bmatrix}, \boldsymbol{A}_{7\times4} = \begin{bmatrix} e^{i2\pi\Delta f_L t_1} & e^{i2\pi\Delta f_{PH} t_1} & e^{i2\pi\Delta f_P t_1} & e^{i2\pi\Delta f_U t_1} \\ e^{i2\pi\Delta f_L t_2} & e^{i2\pi\Delta f_{PH} t_2} & e^{i2\pi\Delta f_P t_2} & e^{i2\pi\Delta f_U t_2} \\ \vdots & \vdots & \vdots & \vdots \\ e^{i2\pi\Delta f_L t_7} & 0e^{i2\pi\Delta f_{PH} t_7} & e^{i2\pi\Delta f_P t_7} & e^{i2\pi\Delta f_U t_7} \end{bmatrix},$$

$$\boldsymbol{E}_{7\times7} = \begin{bmatrix} e^{(-1)^1 i\theta} & 0 & \cdots & 0 \\ 0 & e^{(-1)^2 i\theta} & \cdots & 0 \\ \vdots & \vdots & \ddots & 0 \\ 0 & 0 & 0 & e^{(-1)^7 i\theta} \end{bmatrix}, \boldsymbol{D}_{7\times7} = \begin{bmatrix} e^{i2\pi\psi_0 t_1} & 0 & \cdots & 0 \\ 0 & e^{i2\pi\psi_0 t_2} & \cdots & 0 \\ \vdots & \vdots & \ddots & 0 \\ 0 & 0 & 0 & e^{i2\pi\psi_0 t_7} \end{bmatrix},$$

$$\boldsymbol{P}_{4\times1} = \begin{bmatrix} \rho_L \\ \rho_{PH} \\ \rho_P \\ \rho_U \end{bmatrix},$$

or written as a signal model equation for t_n:

$$S(t_n) = \sum_{m\in\{L,PH,P,U\}} (\rho_m \cdot e^{-i2\pi(\Delta f_m + \psi_0)t_n}) \cdot e^{(-1)^n i\theta}$$

with $S(t_n)$ being the signal recorded at echo time t_n, Δf_m being the relative frequency of metabolite m (L: Lactate, PH: Pyruvate-hydrate,

P: Pyruvate, U: Urea), θ being the complex error for correction of the bipolarity effects, and ψ_0 the static offset of the magnetic field B_0 in Hertz. The values for Δf_m were extracted from the interleaved spectral acquisitions using an automated peak search method (findpeaks(), MATLAB, R2022b). The initial value for θ was set to zero and for ψ_0 to the corresponding pixel-value from the acquired B_0 field map. The field map was therefore down sampled from the ^{1}H- to the ^{13}C-spatial resolution and converted into ^{13}C frequencies by multiplication with $\gamma(^{13}C)/\gamma(^{1}H)$. The whole maps for θ and ψ_0 were iteratively estimated using the algorithm described in *Reeder et al. 2004* for 15 iterations [108]. The final estimation of the metabolite intensities ρ_m was performed using the pseudo-inverse and inverse matrices for $\boldsymbol{A}$, $\boldsymbol{D}$, and $\boldsymbol{E}$.

$$\boldsymbol{P} = (\boldsymbol{A^T A})^{-1}\boldsymbol{A^T} \cdot (\boldsymbol{DE})^{-1} \cdot \boldsymbol{S}$$

The ME-bSSFP sequence used in the study utilised bipolar gradients. A bipolar gradient records the signal during an alternating trajectory through k-space. For technical implementations, the rows of ADC samples from even echoes thus are reverted or tagged with a reversion flag before being stored in a raw data matrix. In our case, the central ADC sample in odd echoes is at index five and in even echoes at index four (total number of ADC samples per echo: 8). To match the k-space centers in odd and even echoes the even echo signals were shifted by one discrete position. However, manually shifting the k-space data in a matrix and applying FFT2 results in complex image data with a linear phase roll in direction of the shift over the entire FOV. The magnitude image is unaffected (no visible artefacts). In order to correct for the phase roll in bipolar echo images the IDEAL model assumes an additional factor $e^{(-1)^n\theta}$ with theta fitting a constant phase offset at the current image position that will alternate in even or odd echoes.

Appendix C: ME-bSSFP Simulator

Below are sample code listings for the ME-bSSFP simulator used in this body of work:

Main Script

```
%% Sequence parameters
M_start = 1;          % start magnetization [a.u.]
M_eq = 1;             % thermal equilibrium magnetization [a.u.]
alpha = 30;           % flip angle [deg]
pulses = 384;           % number of pulses [int]
preps = 0;            % number of preparation pulses [int]
TR = 0.0075:0.0001:0.0225;          % repetition time [s]
no_echoes = 5;         % number of gradient echoes per repetition [int]
delta_TE = 1.02e-3;     % time distance between gradient echoes [s]
flip_back = true;         % flag for flipback pulse [logical]

%% Spin system
no_metabolites = 3;     % number of metabolites [int]
no_spins = 1024;       % number of isochromates per metabolite [int]

% urea + HP pyr , HP lact %% Freiburg phantoms

mean_resonances     =   [20*31,     13*31,   0  ];  % [Hz]
T1                  =   [1.4,     15,     13.1      ];  % [s]
T2                  =   [0.075,     2,      0.622       ];  % [s]
linewidth           =   [20,    20,     20      ];  % [Hz]

%% run the simulation for all sequence parameters
tic

% loop over alphas and TRs
for m = 1:size(alpha,2)
   for j = 1:size(TR,2)

      %% cells for function parameters
      Sequence_parameter = {...
         alpha(m),...
         pulses,...
         preps,...
         TR(j),...
         no_echoes,...
         delta_TE,...
         flip_back...
         };
      Spinsystem = {...
         M_start,...
         M_eq...
         no_metabolites,...
         no_spins,...
```

```
            mean_resonances,...
            T1,...
            T2,...
            linewidth...
            };

        %% run the simulation
        [signal, dist, t_axis] = ...
            sim_me_bssfp(Sequence_parameter, Spinsystem);

        %% store the signal matrix
        n = no_spins;
        k = pulses;

        mean_signal_per_pulse = mean(signal,3);
        std_signal_per_pulse = std(abs(signal),0,3);

        mean_mag_over_seq(:,:,j,m) = ...
            squeeze(mean(abs(mean_signal_per_pulse),2));
        std_mag_over_seq(:,:,j,m) = ...
            squeeze(1/k*sqrt(sum(std_signal_per_pulse.^2,2)));

        mag_last_pulse(:,:,j) = squeeze(mean_signal_per_pulse(:,end,:));

    end
end
toc

%% clear workspace and ...
clearvars -except Sequence_parameter Spinsystem signal dist t_axis ...
    mean_mag_over_seq std_mag_over_seq ...
    mean_signal_per_pulse std_signal_per_pulse ...
    mag_last_pulse;

% ... save
save( ...
    [datestr(now, 'yyyy-mm-dd') '_mebSSFP_results.mat']... filename
    )
```

bSSFP behaviour script (sim_me_bssfp)

```
function [signal_mat, iso_dist, t] = sim_me_bssfp(...
    seq_params, spinsys...
    )

    %% constant parameters

%% sequence parameters
flip_angle = seq_params{1};            % in degree
no_pulses = seq_params{2};              % number #
no_preps = seq_params{3};               % # of preparation pulses
no_echoes = seq_params{5};              % number #

TR = seq_params{4};                    % in s
t_spinecho = TR/2;                     % time of spin-echo

delta_TE = seq_params{6};              % in s

first_echo = t_spinecho - no_echoes/2*delta_TE;          % in s
t_gradecho = zeros(no_echoes,1);
for k = 0:no_echoes-1
    t_gradecho(k+1) = first_echo+ (2*k+1)/2 *delta_TE;
end

flip_back = seq_params{7};                       % 0 = false, 1 = true

%% spin system parameters

% magnetization parameters
M_start = spinsys{1}; % start magnetization in z-direction
M_0 = spinsys{2}; % thermal equilibrium

%% number of metabolites/isochromats
no_isos = spinsys{3};
% number of spins per metabolite
no_spins = spinsys{4};

% every metabolite has own T1, T2 in s
T1 = spinsys{6};
T2 = spinsys{7};                       % in s

% T2_star the same for each metabolite
linewidth = spinsys{8};                % in Hz
T2_star = 1./(pi.*linewidth);          % in s

% offresonance of the isos in Hz
mean_resonances = spinsys{5};

%% make cauchy probability distributions (PD) with center freq and linewidth
% and create spins with random frequency following the PD
if no_spins == 1
    iso_dist =  mean_resonances';
elseif no_isos == 0
```

```
    iso_dist = linspace(-no_spins/2, +no_spins/2, no_spins).*pi/TR/no_spins;
    no_isos = 1;
else
    iso_dist = zeros(no_isos,no_spins);
    for i = 1:no_isos
    rng('default')    % for reproducibility of the random number generation
    pd(i) = makedist('tLocationScale','mu', mean_resonances(i),...
        'sigma', linewidth(i)/2 , 'nu', 1);
    iso_dist(i,:) = random(pd(i), 1,no_spins);
    end
    h_dist = figure(123);
    histogram(iso_dist,4000,'FaceColor','b')
    xlim([-1000, 1000]);
    reverseAxes('xDir');
end


%% preallocations for the sequence

M_mat = zeros(no_spins, 2);
M_mat(:,1) = M_start; % start magnetization

    % Signal matrix contains
    % MATRIX [ Metabolitenumber / Pulsenumber / Echonumber / Z- and XY-Signal
]
signal_mat = zeros(no_isos, no_pulses, no_spins, 2);
phase = 0;  % pulse phase


%% Sequence start
% tic

%% seperated iteration for every metabolite with its spin distribution
for no_iso = 1:no_isos
    M_mat = zeros(no_spins, 2);
    M_mat(:,1) = M_start;

    %% alpha/2-preparation pulse

    M_mat = pulse_function(M_mat,flip_angle/2, phase);
%     signal_mat(no_iso,1,:,:,:) = M_mat(:,:);
    M_mat = relaxation_function(M_mat, M_0, TR/2, T1(no_iso), T2(no_iso));
    M_mat = dephasing_function(M_mat, iso_dist(no_iso,:), TR/2);


    %% preparation pulses ?

    if no_preps ~= 0
        for j=1:no_preps
            phase = phase+180;
            M_mat = pulse_function(M_mat, flip_angle, phase);
            M_mat = relaxation_function(M_mat, M_0, TR, T1(no_iso), T2(no_iso));
            M_mat = dephasing_function(M_mat, iso_dist(no_iso,:), TR);
        end
```

```
    end

    %% refocusing pulses
    for i=1:no_pulses

        phase = phase+180;
        M_mat = pulse_function(M_mat, flip_angle, phase);
        M_mat = relaxation_function(M_mat, M_0, TR/2, T1(no_iso), T2(no_iso));
        M_mat = dephasing_function(M_mat, iso_dist(no_iso,:), TR/2);


        signal_mat(no_iso,i,:,:) = M_mat(:,:);


        M_mat = relaxation_function(M_mat, M_0, TR/2, T1(no_iso), T2(no_iso));
        M_mat = dephasing_function(M_mat, iso_dist(no_iso,:), TR/2);
    end


    %% flip back pulse

    if flip_back
        phase = phase+180;
        M_mat = pulse_function(M_mat, flip_angle, phase);
        M_mat = relaxation_function(M_mat, M_0, TR/2, T1(no_iso), T2(no_iso));
        M_mat = dephasing_function(M_mat, iso_dist(no_iso,:), TR/2);

        phase = phase+180;
        M_mat = pulse_function(M_mat, flip_angle/2, phase);

            signal_mat(no_iso, no_pulses+1,:,:) = M_mat(:,:);
    end

end

% toc

% signal_mat = signal_mat./M_start;

%% Plot the result
if flip_back
    t = [no_preps*TR + (1:no_pulses)*TR, no_preps*TR + no_pulses*TR + TR/2 ];
else
    t = [no_preps*TR + (1:no_pulses)*TR];
end

return
%##########################################################################
##########

%% plot the xy-magnetization of each metabolite per time (per echo in fig)
for j=1:no_echoes
    figure(j)
```

```
    subplot(3,2,1)
    plot(t, real(squeeze(signal_mat(1,:,j,:,2))),'-.');
    title(['Echo No. ' num2str(j) ', real, met 1'])
    xlabel('Time [s]')
    ylabel('absolut signal')
    axis([(no_preps-10)*TR, (no_preps+no_pulses+10)*TR, -M_start, M_start])


    subplot(3,2,2)
    plot(t, imag(squeeze(signal_mat(1,:,j,:,2))),'-.');
    title(['Echo No. ' num2str(j) ', imag, met 1'])
    xlabel('Time [s]')
    ylabel('absolut signal')
    axis([(no_preps-10)*TR, (no_preps+no_pulses+10)*TR, -M_start, M_start])


    subplot(3,2,3)
    plot(t,real(squeeze(signal_mat(2,:,j,:,2))),'-.');
    title(['Echo No. ' num2str(j) ', real, met 2'])
    xlabel('Time [s]')
    ylabel('absolut signal')
    axis([(no_preps-10)*TR, (no_preps+no_pulses+10)*TR, -M_start, M_start])

    subplot(3,2,4)
    plot(t,imag(squeeze(signal_mat(2,:,j,:,2))),'-.');
    title(['Echo No. ' num2str(j) ', imag, met 2'])
    xlabel('Time [s]')
    ylabel('absolut signal')
    axis([(no_preps-10)*TR, (no_preps+no_pulses+10)*TR, -M_start, M_start])

    subplot(3,2,5)
    plot(t,real(squeeze(signal_mat(3,:,j,:,2))),'-.');
    title(['Echo No. ' num2str(j) ', real, met 3'])
    xlabel('Time [s]')
    ylabel('absolut signal')
    axis([(no_preps-10)*TR, (no_preps+no_pulses+10)*TR, -M_start, M_start])

    subplot(3,2,6)
    plot(t,imag(squeeze(signal_mat(3,:,j,:,2))),'-.');
    title(['Echo No. ' num2str(j) ', imag, met 3'])
    xlabel('Time [s]')
    ylabel('absolut signal')
    axis([(no_preps-10)*TR, (no_preps+no_pulses+10)*TR, -M_start, M_start])

    %
end

%% average over all spins of each metabolite
% signal_mat_avg_mag = mean(abs(signal_mat),4);
signal_mat_avg_mag = mean(signal_mat,4);
% signal_mat_std_mag = std(abs(signal_mat),0,4);
signal_mat_std_mag = std(abs(signal_mat),0,4);
signal_mat_var_mag = var(abs(signal_mat),0,4);
```

```
for j = 1:no_echoes
   figure(j+no_echoes)

   subplot(3,1,1)
   errorbar(t,
abs(squeeze(signal_mat_avg_mag(1,:,j,1,2))),squeeze(signal_mat_std_mag(1,:,j,1,
2)),'-.')
   title(['Echo ' num2str(j) ',met 1 magn'])
   xlabel('time')
   ylabel('absolute signal')
   axis([(no_preps-10)*TR, (no_preps+no_pulses+10)*TR, -M_start, M_start])
   leg_strings = [];
   for i = 1:no_isos
      leg_strings = [leg_strings; ['metabolite ' num2str(i)]];
   end
   legend(leg_strings)


   subplot(3,1,2)
   errorbar(t,
abs(squeeze(signal_mat_avg_mag(2,:,j,1,2))),squeeze(signal_mat_std_mag(2,:,j,1,
2)),'-.')
%     plot(t, real(squeeze(signal_mat_avg_mag(:,:,j,1,2))),'.')
   title(['Echo ' num2str(j) ',met 2, magn'])
   xlabel('time')
   ylabel('absolute signal')
   axis([(no_preps-10)*TR, (no_preps+no_pulses+10)*TR, -M_start, M_start])


   subplot(3,1,3)
   errorbar(t,
abs(squeeze(signal_mat_avg_mag(3,:,j,1,2))),squeeze(signal_mat_std_mag(3,:,j,1,
2)),'-.')
%     plot(t, imag(squeeze(signal_mat_avg_mag(:,:,j,1,2))),'.')
   title(['Echo ' num2str(j) ', met 3, magn'])
   xlabel('time')
   ylabel('absolute signal')
   axis([(no_preps-10)*TR, (no_preps+no_pulses+10)*TR, -M_start, M_start])
end


%% FUNCTIONS

function M_back = dephasing_function(M,dephasing_distribution, t)

deph_mat = [ones(size(M,1),1), exp(1i*dephasing_distribution'*t*2*pi)];
M_back = M.*deph_mat;

function signal_back = T2_star_weighting_function(signal, t,t_spinecho, T2_star)
relax_mat = zeros([2,2, size(t,1)]);
signal_temp = zeros(size(signal));

re_or_dephase = -sign(t-t_spinecho);
for n = 1:size(size(signal(1)))
```

```
for k = 1:size(t,1)
   relax_mat(:,:,k) = [...
      1,          0;...
      0,          exp(re_or_dephase(k)*(t(k)-t_spinecho)/T2_star)...
      ];
   for l = 1:size(signal,2)
      signal_temp(n,l,k,:,:) = squeeze(signal(n,l,k,:,:))*relax_mat(:,:,k);
   end
end
end

signal_back = signal_temp;


function M_back = relaxation_function(M, M_0, t, T1,T2)

% relax_mat = zeros([2,2]);
z_mat = zeros(size(M));
M_temp = zeros(size(M));

% for i=1:size(T1,2)
   relax_mat = [...
      exp(-t/T1),     0;...
      0,              exp(-t/T2)...
      ];
   z_mat(:,1) = M_0*(1-exp(-t/T1));

   M_temp(:,:) = M(:,:)*relax_mat(:,:) + z_mat;
% end

M_back = M_temp;


function M_back = pulse_function(M, angle, phase)
M_temp = [real(M(:,2)), imag(M(:,2)), M(:,1)];

phase = phase*pi/180;
angle = angle*pi/180;

rot_mat = [...              %  Ry(phase)Rx(angle)Ry(-phase)
   cos(angle)*sin(phase)^2+cos(phase)^2,   cos(phase)*sin(phase)*(cos(angle)-1),
sin(angle)*sin(phase);...
   cos(phase)*sin(phase)*(cos(angle)-1),   cos(angle)*cos(phase)^2+sin(phase)^2,
sin(angle)*cos(phase);...
   -sin(angle)*sin(phase),                 -sin(angle)*cos(phase),
cos(angle)...
   ];                   % see Liang/Lauterbur p.82

M_temp = M_temp*rot_mat';
M_back = [M_temp(:,3), M_temp(:,1)+1i*M_temp(:,2)];
```